Durham University

Durham E-Theses

Microwave Induced Optical Nonlinearities in Cuprous Oxide

JONATHAN DENYS PRITCHETT

How to cite:

PRITCHETT, JONATHAN DENYS (2023) Microwave Induced Optical Nonlinearities in Cuprous Oxide. Doctoral thesis, Durham University.

Use policy

The full-text may be used and/or reproduced, and given to third parties in any format or medium, without prior permission or charge, for personal research or study, educational, or not-for-profit purposes provided that:

- a full bibliographic reference is made to the original source
- a https://etheses.durham.ac.uk/id/eprint/15291/ is made to the metadata record in Durham E-Theses
- the full-text is not changed in any way

The full-text must not be sold in any format or medium without the formal permission of the copyright holders.

Please consult the full Durham E-Theses policy for further details.

Academic Support Office, The Palatine Centre, Durham University, Stockton Road, Durham, DH1 3LE
e-mail: e-theses.admin@durham.ac.uk Tel: +44 0191 334 6107
https://etheses.durham.ac.uk

Microwave Induced Optical Nonlinearities in Cuprous Oxide

Jonathan D. Pritchett

A thesis presented for the degree of
Doctor of Philosophy

Quantum Light and Matter
The University of Durham
United Kingdom
14th December 2023

Microwave Induced Optical nonlinearities in Cuprous Oxide

Jonathan D. Pritchett

Abstract

This thesis presents an experimental study of the transmission spectrum of cuprous oxide in the presence of a microwave field. Using one photon spectroscopy an excitonic population is created which can then be modified by the application of a microwave field.

This was achieved using a combination of microwave antennae and high-resolution spectroscopy. The main results presented in this thesis are: (1) Using photoluminescence and transmission spectroscopy the quality of natural and synthetic samples was measured, finding natural samples to be far superior. This was attributed to the presence of copper vacancies in the synthetic material. These vacancies were removed through thermal annealing, but this did not improve the quality of synthetic samples. (2) Determination of temperature as the limiting factor to observe higher nP states. This was carried out through spectroscopy of cuprous oxide over a range of temperatures. (3) Observation of large optical nonlinearities in the presence of a microwave field. These manifest as changes in absorption which is stronger for higher n states, where for sufficiently strong fields it is no longer possible to resolve them. An additional impact of the microwave field is an increase in the absorption between states. These observations were modelled by treating excitons as spinless hydrogen enabling an extraction of the nonlinear susceptibility using an atomic physics approach. The change in absorption is well described by this model. Alongside this, a large cross-Kerr nonlinearity is estimated which is several orders of magnitude larger than that seen in conventional media. These results cement cuprous oxide as a viable platform for Rydberg physics wherein strong coupling to external fields can be detected. This also highlights the need to develop high-quality synthetic material to remove the reliance on naturally occurring samples.

Supervisors: Matthew P. A. Jones and Stuart Adams **Durham University**
Quantum Light and Matter
Department of Physics
South Road
Durham
DH1 3LE

Acknowledgements

One of the most important aspects of science is its collaborative nature. This part however, doesn't always come through in how we talk about science. So, I would like to take this change to thank the people who have helped and supported me throughout this PhD. Without them this thesis would never have been completed and the last four years of research would have been a totally different experience.

First of all, I would like to thank my supervisor Matt Jones. Your constant support and guidance kept me on the right track the entire way. I have learned a lot about science with you, and not just about cuprite. I would also like to thank my secondary supervisor Stuart. Your insights and thoughts were always helpful regardless of when we came to you. Alongside this, I want to offer my thanks to the cuprite team team: Liam, Josh, Dani and Horatio. It has been a joy to work alongside all of you, and I will sorely miss it going forwards. A special thanks to Liam, for training me to work in the lab and battling through a wall of theory together. As well as I would like to thank Dani for introducing me to science while I was still working by myself in the basement that first year.

I would also like to thank my fellow members of QLM. You have all made Durham such a welcoming and inclusive environment to be in. The talent and expertise here made so much more of a difference than I ever thought it could. Between tea times and the occasional run it has been a great place to be.

Beyond Durham I would like to thank our collaborators in Cardiff: Stephen, Wolfgang and Sam. You have all provided key insights into this material and much of this thesis would have been impossible without you. I am excited to see what developments lie in the future! I would also like to thank my friends and

family for your support and belief. Physics is as it turns out quite hard, and having people backing you up makes a huge difference.

Contents

Declaration

The work in this thesis is based on research carried out in Department of Physics, University of Durham, United Kingdom. The work in this thesis was supported by a studentship from EPSRC. The data presented in this thesis is available on request form the author. No part of this thesis has been submitted elsewhere for any other degree or qualification, and it is the sole work of the author unless referenced to the contrary in the text.

Copyright © 2023 by Jonathan D. Pritchett.

"*The copyright of this thesis rests with the author. No quotation from it should be published without the author's prior written consent and information derived from it should be acknowledged*".

List of Figures

List of Tables

Nomenclature

AOM acousto-optic modulator

BPD balanced photodiode

CB conduction band

ECDL external cavity diode laser

FPE Fabry-Pérot etalon

FWHM full width half maximum

IR infra-red

LED light emitting diode

NA numerical aperture

PBS polarising beam splitter

PL photoluminescence

ppLN periodically-poled lithium niobate

RFA Raman fibre amplifier

SHG second harmonic generation

VB valence band

Chapter 1

Introduction

At the turn of the 20$^{\text{th}}$ century work was underway in understanding the emission spectra of atoms [1]. These spectra were characterized by a series of discrete lines, corresponding to the discrete energy level structure within atoms [2]. From this notion the basic elements of quantum mechanics were formed, wherein energy levels are described by different quantum numbers [3], of particular note is the principal quantum number n. The invention of the laser in the late 1950s [4] offered physicists access to strong narrowband electromagnetic fields. This enabled highly excited atomic states, known as Rydberg states [5; 6], to be readily accessed and utilised [6]. Owing to the scaling of many physical properties of atoms with n, Rydberg states have exaggerated properties. Notable among these is the spatial extent, scaling with n^2 [5]. This leads to atomic radii of the order of µm across [7; 8].

The large separation between the valance electron and ionic core of Rydberg atoms allows for such states to be treated as hydrogenic [9]. Another consequence of their large spatial extent is that they are highly sensitive to electromagnetic fields [10; 11; 12; 13], such as those produced by neighbouring Rydberg states [14; 15]. The result of this is that long-range Van der Vaal interactions create a "blockaded" region around a Rydberg atom [16]. Within this region, the presence of a Rydberg state shifts the energy of neighboring Rydberg states preventing their excitation [17; 18]. This can be utilised to create single photon sources [19; 17; 20; 21] and absorbers [22; 23; 24; 25] paving the way for all-optical signal processing [26; 27; 28; 29; 30; 31]. Furthermore, the long-range interactions lead to large nonlinearities, in turn giving rise to perfect reflectors [32; 33; 34] and offering control over light at the single photon level [35; 36]. This has led to

interest in utilizing Rydberg states as a potential platform for developing quantum computers [37; 38; 39].

The strong coupling to external fields can be utilized to create very sensitive and efficient devices [40; 41]. This arises as electric fields can couple opposite parity Rydberg states through electric dipole transitions [3], the strength of which scaling with n^2 [5]. As a result, Rydberg states can be strongly coupled to one another. Transitions can be found between Rydberg states ranging from radio to THz frequencies [42; 43; 44; 45] offering a wide range of potential applications. One such application is as an optical readout for superconducting solid-state qubits [35; 46]. These systems have attracted significant interest in recent years owing to the control offered over qubit coupling [47; 48]. However, a major disadvantage of the microwave frequencies is that it is not possible to extract information over long distances, owing to thermal noise [49; 50]. One possible way this challenge can be overcome is by coupling the microwave frequencies to optical frequencies. In the optical regime, communication can be achieved over global length scales [51; 52]. Thus, combining these two systems would allow for the best parts of both to be simultaneously utilized. While such coupling has been demonstrated for Rydberg atoms [53; 35], these atomic systems are not inherently compatible with the cryogenic environment of the dilution fridge solid-state qubits reside in.

In recent years an alternative platform for Rydberg physics has emerged in the form of cuprous oxide [54; 55; 56; 57], a cut gemstone which is shown in Fig. 1.1. In 2014, a discrete series of absorption lines was observed corresponding to excitonic states up to principal quantum number $n = 25$ [58]. More recent experiments have been able to resolve up to $n = 30$ [59], placing these states firmly into the Rydberg regime, with spatial extents µm across in size. Excitons are the solid-state analogue to hydrogen [60; 61] consisting of a bound electron-hole pair [62], and show the characteristic Rydberg series of energy levels [63]. However, owing to a screening of the electric field between them by the crystal lattice, they have a much lower binding energy. This in turn leads to larger Bohr radii [58].

Cuprous oxide distinguishes itself from archetypal semiconductors by its relatively large binding energy of ∼90 meV [59; 58; 64]. This is particularly notable when compared to the archetypal direct band gap semiconductors GaAs with 4.2 meV [65] or 2.7 meV for Ga [66]. While this enables higher principle quantum number states to be resolved, it is not the sole criteria for observing up to $n = 30$. For

example, copper chloride (CuCl) has an excitonic binding energy of ∼130 meV but only up to $n = 4$ have been resolved [67; 68]. Furthermore, exceptionally high binding energies in the range of 100s of meV can be found in 2D semiconductors [69]. But again, high principle quantum numbers have not been resolved here. As such it is not only the large binding energy that enables the observation of Rydberg excitons. A further criterion is that the line widths of the corresponding states are suitably narrow. This is achieved by a combination of crystallographic structure, specifically cubic structure, and suitably forbidden re-combinations [58]. These criteria ensure that the excitons behave as hydrogenic objects with long lifetimes and correspondingly narrow absorption peaks. It is the combination of these features that enabled the first observation of excitons in 1956 in cuprous oxide [70].

Like atomic states, excitons can couple very strongly to external electronic fields [71; 72; 73]. In particular, the narrow spacing and broad nature of the high-lying states results in broadband coupling to microwave fields [74]. A major advantage of the solid-state nature of cuprous oxide is that it is well suited to the dilution fridge environment of superconducting qubits. This makes it an excellent candidate for optical reading out the microwave frequencies.

Unlike archetypal semiconductors, such as GaAs or Si, there has been limited technological development originating from cuprous oxide. There was interest in using the low principal quantum number states of the yellow series in the search for the excitonic Bose-Einstein condensates (BEC) [75; 76; 77]. The low mass of the exciton leads to the BEC being predicted to form at much higher temperatures compared to atomic systems [78]. Moreover, the long lifetimes of the lowest excitonic state made it seem like an ideal candidate [79]. However, collisional processes resulted in the system not being as ideal as initially thought [76]. Alongside this cuprous oxide has presented itself more recently as a high-efficiency thin-film solar cell [80; 81; 82]. Regardless of this, there has been only a small amount of interest in developing high-quality synthetic samples. The result of this is the highest nP states have only been observed in naturally occurring samples [59]. Relying solely on natural samples is not a sustainable model.

The purpose of this thesis is to investigate microwave-induced nonlinearities in cuprous oxide due to Rydberg excitons, in particular the cross-Kerr effect. This not only serves to explore the similarities between atomic and excitonic systems but also to further establish the viability of cuprous oxide as a Rydberg platform.

Figure 1.1: Photo copyright Joel E Arem, used with permission. Cut and polished gemstone of cuprous oxide, of particular note is its metallic red lustre. Despite its attractive appearance, cuprite is too soft for use in jewellery.

This thesis utilizes the setup built in [55], which in turn was built up to develop the quantum optical applications of cuprous oxide. The modifications made to this setup will be described in the relevant chapters. Using this setup, this thesis will focus on single photon transmission spectroscopy in the presence of a microwave field. Doing so will enable the characterization of the nonlinear optical properties of cuprous oxide. In the future microwave resonators will be used in place of broad band antennae and the photon statistics of light will be studied in search of quantum light. Such processes will be described using an atomic physics-based model of the nonlinear susceptibility

1.1 Structure of the Thesis

The layout of this thesis is as follows. The second chapter will lay out the theoretical description of excitons in cuprous oxide. This will be based on a modified hydrogenic model, and utilize a nonlinear electronic susceptibility model to de-

scribe how microwave fields modify the transmission. The third chapter will seek to compare and contrast high-quality natural samples with synthetically grown samples via transmission and photoluminescence (PL) spectroscopy. Synthetic samples were then thermally annealed in an attempt to improve their quality. The fourth chapter will present the experimental setup for transmission spectroscopy of cuprous oxide. It will then seek to determine the factors limiting the observation of high n states in this system.

The fifth chapter will describe the modifications to the transmission spectroscopy setup to enable the application of a microwave field across the sample. The modification of the transmission will be described using the nonlinear electronic susceptibility built up in the second chapter. This model provides quantitative agreement in the low microwave field strength regime. Furthermore, the modulation of the phase of the transmitted light, corresponding to a cross-Kerr effect, will be characterized by looking at the spectrally resolved transmission. The estimated Kerr effect extracted by doing this is of the order of 10^{-2} mV^{-2}, over 10 orders of magnitude larger than the archetypal Kerr medium nitrobenzene at 10^{-12} mV^{-2}.

Finally, the sixth will briefly explore the changes to the transmission spectrum in very intense fields. This will include a comparison to a Floquet theorem-based atomic model developed by Alistair Brewin here in Durham. This serves as a more complete description of the atomic states than the nonlinear susceptibility model.

Publications

A list of publications arising from work presented in this thesis are given below:

1. L. A. P. Gallagher, J. P. Rogers, J. D. Pritchett, R. A. Mistry, D. Pizzey, C. S. Adams, M. P. A. Jones, P. Grünwald, V. Walther, C. Hodges, W. Langbein, and S. A. Lynch, “Microwave-optical coupling via Rydberg excitons in cuprous oxide,", Phys. Rev. Research **4**, 013031 (2022). [74].

2. S. A. Lynch, C. Hodges, S. Mandal, W. Langbein, R. P. Singh, L. A. P. Gallagher, J. D. Pritchett, D. Pizzey, J. P. Rogers, C. S. Adams, and M. P.

A. Jones, "Rydberg excitons in synthetic cuprous oxide Cu_2O," Phys. Rev. Materials **5**, 084602 (2021) [83].

3. J. P. Rogers, L. A. P. Gallagher, D. Pizzey, J. D. Pritchett, C. S. Adams, M. P. A. Jones, C. Hodges, W. Langbein, and S. A. Lynch, "High resolution nanosecond spectroscopy of even-parity Rydberg excitons in Cu_2O," (2021), arXiv:2111.13062 [cond-mat.mes-hall]. Submitted to Physical Review B [84]

Chapter 2

Optical Properties of Cuprous Oxide

To explore the similarities and differences between excitons and atoms it is crucial first to consider the crystallographic environment excitons find themselves in. The defining feature of crystal structures is their periodicity. A major consequence of this is that electrons are forced to exist in a series of energetic bands. These bands describe the electron energy as a function of its (quasi) momentum [85]. The corresponding wavefunctions are delocalised over the volume of the material, these are described by Bloch functions [86]. Semiconductors are characterized by the existence of an energy gap between adjacent bands, known as a band gap. In particular, they require the Fermi level of the system to be located between these bands. The band below this is known as the valence band (VB) while the band above is known as the conduction band (CB) [87]. The placement of the Fermi level results in an empty conduction band when the semiconductor is in its ground state.

To excite an electron from the valance band to the conduction band a change in momentum and energy is required. For direct band gap semiconductors the required change in momentum is 0, enabling the optical excitation of electrons. Doing so leaves behind a positively charged hole, which is schematically illustrated in Fig. 2.1 (a). As a result, both the size and nature of the band gap is critical to the optical properties of a semiconductor [86]. Cuprous oxide is no exception to this, with the most relevant band gap being direct and corresponding to optical frequencies for absorbed light. Towards the band edge these properties are further influenced by the presence of excitons: bound electron-hole states [86; 61; 88]. Owing to the Coulombic interaction between the oppositely charged particles excitons can be described by a simple hydrogenic model. This is illustrated in

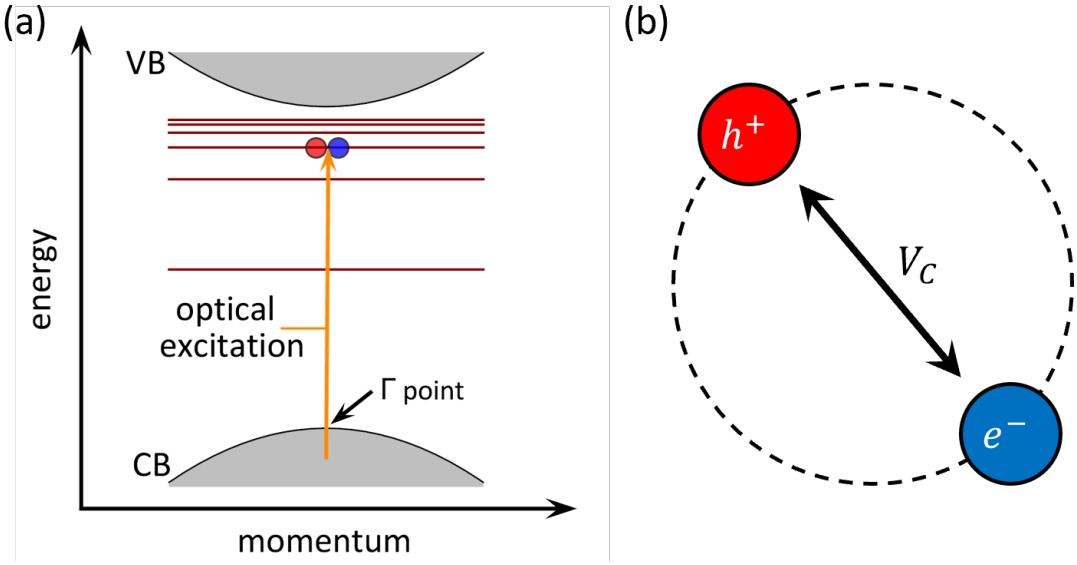

Figure 2.1: Illustration of the formation of excitons in semiconductors. (a) schematic diagram of electronic band structure around the Γ point, the centre of the Brillouin zone. Under optical excitation, excitons can be formed, these form at discrete energy levels, as shown by the horizontal red lines. (b) bound electron-hole pair due to the Coulomb interaction between them. This results in a hydrogen-like structure.

Fig. 2.1(b). This model is further modified by the crystallographic environment. Both of these concepts will be explored throughout this chapter.

The large binding energy of cuprous oxide, alongside the parity of the relevant bands, enables the observation of high principal quantum number states [59]. These highly excited states have physical extents up to µm across [58]. Such large radii lead to correspondingly large dipole moments, resulting in strong coupling to the external field [5]. A major consequence of this is the absorption spectrum of cuprous oxide can be dramatically modified by external fields [74]. In particular, the large line widths and narrow spacing between high n states enable strong coupling to microwave frequency fields.

This chapter will lay out a hydrogenic description of excitons in cuprous oxide starting from the material's crystal structure. Doing so will enable a full description of the absorption spectrum of cuprous oxide around the band edge. This model will then be further developed through a nonlinear susceptibility model. The nonlinear susceptibility will allow for changes to the spectrum due to an external microwave field to be described.

2.1 Structure of Cuprous Oxide

2.1.1 Physical Structure

Cuprous oxide is physically characterized by its distinctive red appearance, described as an adamantine lustre [89]. The colour originates from the direct band gap of ∼2.17 eV, which results in only red light being transmitted. Structurally, cuprous oxide is a cubic structure with a lattice constant of 4.27 Å [90], made up of copper face centre cubic (fcc) and oxygen body-centred cubic (bcc) sublattices. These lattices are shifted from one another by a quarter of the body diagonal, as shown in Fig. 2.2(a). Cuprous oxide belongs to the O_h symmetry group.

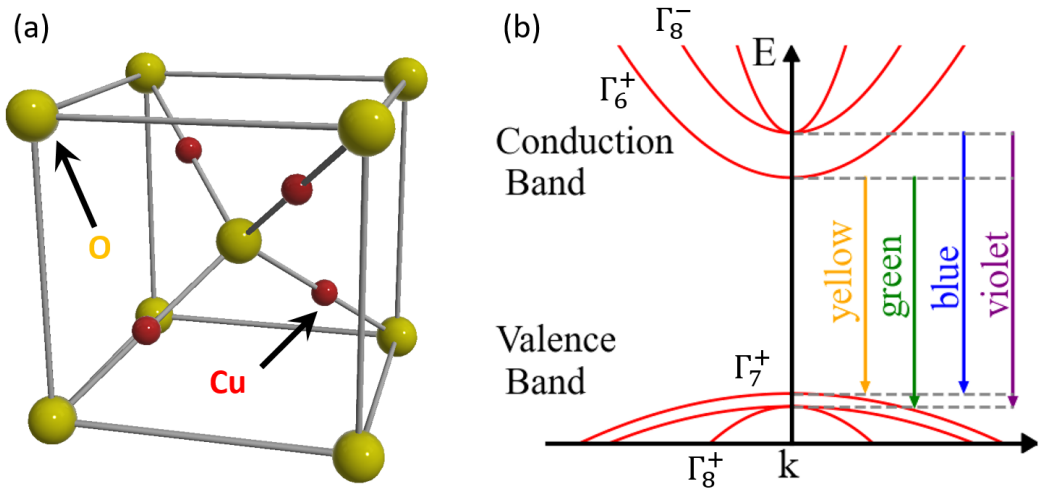

Figure 2.2: Overview of the physical and electronic structure of cuprous oxide. (a) the unit cell of cuprous oxide: showing the fcc copper lattice interleaved with the bcc oxygen lattice. (b) schematic of the band structure of cuprous oxide at the Γ point. Four excitonic series exist between the two lowest-lying conduction bands and two highest-lying valence bands.

2.1.2 Energetic Structure

The electronic band arising from the physical structure laid out in the previous section has been calculated extensively [91; 92; 93; 94]. Cuprous oxide is a direct band gap semiconductor with a band gap of approximately 2.172 eV. Because the valence and conduction bands share the same parity direct optical excitation is dipole forbidden. This band structure is schematically illustrated in Fig. 2.2(b).

This thesis will focus on the electronic structure around the Γ point, where the effective mass approximation is valid. Bands are described by their irreducible symmetries $\Gamma_x^{\pm}$ where ± refers to the parity [95]. An unusual property of cuprous oxide is that both the lowest-lying conduction band and the highest-lying valence band originate from the orbitals of the same element, in this case copper. The 4s copper orbital is responsible for the conduction band and the 3d copper orbital leads to the valence band [96].

There are four excitonic series in cuprous oxide existing between the two highest-lying valance bands and two lowest-lying conduction bands. These series are labelled according to the energy of the band gap that exists between the yellow, green, blue, and violet series. The yellow series forms the focus of this thesis where the highest excitonic states have been observed, up to $n = 30$ [59]. However, studies have been carried out on the other series through PL spectroscopy [97]. So far excitons have not been resolved as far into those series. This is likely due to research interest being primarily focused on the yellow series as an already proven platform for Rydberg excitons.

2.2 Hydrogenic Model of Excitons

In general, quantum mechanical systems cannot be solved analytically. The origin of this lies in the interaction of multiple bodies with one another, leading to the problems rapidly becoming intractable [3]. Hydrogen, however, is one of the few systems for which a solution can be found. This system is so well understood that it can be used as a means of searching for new physics beyond the standard model [98; 99]. Here, the electron of mass m_{e}, located at $\mathbf{r}_{\mathrm{e}}$, and a proton of mass m_{p}, located at $\mathbf{r}_{\mathrm{p}}$, interact with each other according to the following Hamiltonian [100]:

$$H_{\mathrm{H}} = -\frac{\hbar^2}{2M}\nabla_{\mathrm{R}}^2 - \frac{\hbar^2}{2\mu}\nabla_{\mathrm{r}}^2 - \frac{e^2}{(4\pi\epsilon_0)r}, \tag{2.1}$$

where μ is the reduced mass of the system, defined by $\mu^{-1} = m_{\mathrm{e}}^{-1} + m_{\mathrm{p}}^{-1}$, $M = m_{\mathrm{e}} + m_{\mathrm{p}}$ is the total mass and e is the electron charge. The two coordinates used in this equation are the centre of mass coordinate $\mathbf{R} = (m_{\mathrm{e}}\mathbf{r}_{\mathrm{e}} + m_{\mathrm{p}}\mathbf{r}_{\mathrm{p}})/(m_{\mathrm{e}} + m_{\mathrm{p}})$ and relative coordinate $\mathbf{r} = |\mathbf{r}_{\mathrm{e}} - \mathbf{r}_{\mathrm{p}}|$. The first term in the Hamiltonian describes the kinetic energy of the centre of mass, the second describes the relative motion of the electron and proton. The final term is the Coulomb interaction between the proton and the electron. A major result of this form of the Hamiltonian is the existence of bound energy levels, E_{n}, described by:

$$E_{\mathrm{n}} = -\frac{Ry}{n^2}, \tag{2.2}$$

where Ry is the Rydberg constant, which is -13.6 eV for hydrogen, and n is the familiar principal quantum number. The wavefunctions can be determined by solving the corresponding Schrodinger equation. The ability to describe objects in the same way as hydrogen is highly appealing. Not only does it enable the discussion of excitonic states in terms of atomic physics (e.g. S, P, D... like symmetries) but it also enables the modelling of related phenomena. Chief among these are transitions between states and optical nonlinearities. The following section will lay out excitons within a hydrogenic picture and introduce corrections to this model resulting from the crystal environment.

2.2.1 Electrons and Holes

A distinguishing characteristic of the hydrogenic model is that the electron and proton move through space as free particles. The only interaction between them

arises from the Coulomb interaction. Electrons (and holes) within a crystal lattice however do not move as free particles owing to the structure of this lattice [86]. Instead, they move with effective masses, m_{e}^{*} (m_{h}^{*}) given by the curvature of the conduction (valance) band. However, the parabolic nature of the bands around the Γ allows for electrons and holes to be treated as free particles with masses given by their effective mass. Such an approximation is valid when the excitonic radius is much larger than the crystal unit cell [101; 102]. This is a reasonable approximation to make in cuprous oxide where the excitonic Bohr radius is 1.11 nm [58], over twice the lattice spacing of 4.27 Å. This approximation only becomes more appropriate for higher-lying exciton states with larger radii.

Within the effective mass approximation, the Coulomb interaction between the electron and hole is given by the familiar potential:

$$V(r) = \frac{-e^2}{4\pi\epsilon_0\epsilon_{\mathrm{r}} r}, \tag{2.3}$$

where ϵ_r is the relative permittivity, which is approximately 7.5, and $r = |\mathbf{r}_{\mathrm{e}} - \mathbf{r}_{\mathrm{h}}|$, where r_{e} and r_{h} are the electron and hole coordinates. The role of the relative susceptibility is to include the screening of the Coulomb interaction due to the dielectric nature of the material. In much the same way as for hydrogen the Hamiltonian, H_0 can be written down by using a reduced mass, $\mu^{-1} = m_{\mathrm{e}}^{-1} + m_{\mathrm{h}}^{-1}$, total mass, $M = m_{\mathrm{e}} + m_{\mathrm{h}}$ and centre of mass coordinate $\mathbf{R} = (m_{\mathrm{e}}\mathbf{r}_{\mathrm{e}} + m_{\mathrm{h}}\mathbf{r}_{\mathrm{h}})/(m_{\mathrm{e}} + m_{\mathrm{h}})$. This results in the following form for H_0 of the exciton:

$$H_0 = E_{\mathrm{g}} - \frac{\hbar^2}{2M}\nabla_{\mathrm{R}}^2 - \frac{\hbar^2}{2\mu}\nabla_{\mathrm{r}}^2 + V(r), \tag{2.4}$$

where E_{g} is the bandgap energy. As before, the second term describes the kinetic energy of the centre of mass of the exciton. Similarly, the third term describes the kinetic energy from the relative motion of the electron and hole. Once again, this leads to atomic energy levels described by:

$$E_{\mathrm{X}} = E_{\mathrm{g}} - \frac{R_{\mathrm{X}}}{n^2}, \tag{2.5}$$

where n is the principal quantum number of the exciton and R_{X} is the excitonic Rydberg energy. Unlike hydrogen, this constant is much smaller, ~90 meV. The wavefunctions are once again obtained by solving the time-independent Schrodinger equation. Like hydrogen the excitonic radius scales, r_n, with n^2 according to :

$$\langle r_{\mathrm{n}} \rangle = a_{\mathrm{B}}\frac{1}{2}(3n^2 - l(l+1)), \tag{2.6}$$

where l is the angular momentum principle quantum number and a_{B} is the Bohr radius. The key difference between the two objects is that the screening of the Coulomb interaction within the crystal lattice leads to this being 1.11 nm in cuprous oxide, as opposed to 0.5 Å for Hydrogen. A consequence of this much larger Bohr radii is a much larger dipole moment [5].

While the hydrogenic picture does provide a reasonable approximation to describe the excitonic series experimental observations show deviations. These will be explored in the following section.

2.2.2 Deviations from the Hydrogenic Model

The deviations from the hydrogenic model are largely due to the physical structure of the crystal lattice. The effective mass approximation treats electrons and holes as free particles moving with effective masses. This can be thought of as ignoring the structure of the crystal lattice. The impact of this will be explored here by adding additional terms to the excitonic Hamiltonian. The treatment laid out here follows that laid out in [103; 104] and is similar to that used in [55].

The deviations from the hydrogenic model can be understood as a series of corrections to the Hamiltonian in eqn. 2.4. Specifically, they modify that Hamiltonian to:

$$H = H_0 + H_{\mathrm{CC}} + H_{\mathrm{SO}} + H_{\mathrm{d}} + H_{\mathrm{X}}, \tag{2.7}$$

where H_0 is given in eqn. 2.4, each term will be discussed in turn. The form of these terms will not be discussed in this thesis, only their impact on the energetic structure. To illustrate this the splitting of the $n = 4$ excitonic states is shown in Fig. 2.3. This is similar to the figure shown in [105].

The first correction term to the Hamiltonian, H_{CC}, is the central cell correction [103; 106]. This takes into account the deviations of the Coulomb potential at short range, including the exciton-phonon interactions. The exciton-phonon interactions are challenging to take into account owing to two optical-phonon branches [107], but the simple term employed here is still reasonably effective. This accounts for the non-parabolicity of the valence bands, which primarily impacts the lowest-lying excitonic states. Physically this can be understood by the smaller radii of these lower-lying states.

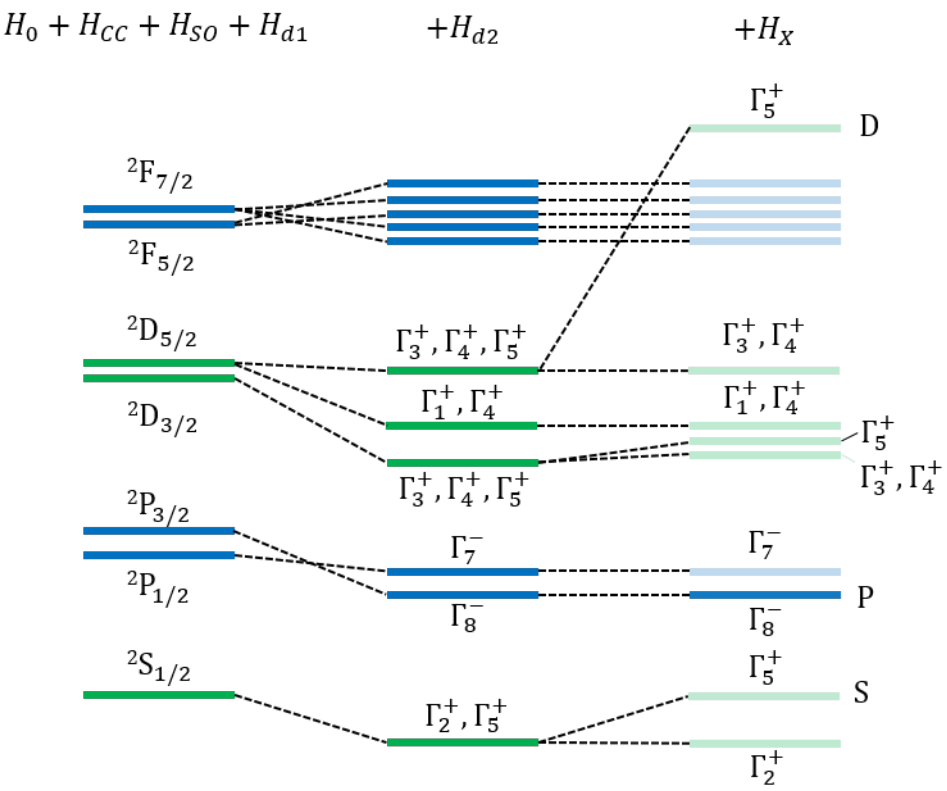

Figure 2.3: Schematic of the fine structure splitting for the n=4 exciton energy levels. Splittings are not to scale. Odd parity states are shown in blue with even parity states in green. This is based on Figure 2 of [105]. The first column shows the fine structure including the spherically symmetric terms of the Hamiltonian. The second term shows the splitting due to H_{d2}, accounting for the cubic symmetry of the crystal lattice. The final column shows the impact of exchange interactions. Only the highlighted state P is optically active under single-photon excitation. The states labelled S and D are highly relevant in chapter 5 and 6 where transitions between states is discussed.

The second term, H_{SO}, is an effective spin-orbit coupling term [103; 108; 105]. This results in the splitting of the valance bands Fig. 2.2(b). This splitting gives rise to two non-interacting series of excitons, the yellow and green series. These can be described by their quasi-spin quantum number, s, and associated angular momentum of the envelope function, l. Alongside energy, the series are distinguished by their different spin angular momentum quantum numbers of 1/2 and 3/2 for the yellow and green bands respectively. Alongside this, the spin-orbit coupling results in a non-parabolic dispersion for the uppermost valence band.

The third term, H_{d}, is a correction to the effective mass approximation and mixes the yellow and green excitonic series [103]. The term can be further split into

two separate terms $H_{\mathrm{d}} = H_{\mathrm{d1}} + H_{\mathrm{d2}}$. The first is spherically symmetric while the second has a cubic symmetry. H_{d1} does not commute with either s or l and results in the two becoming coupled. This gives rise to a fine structure splitting for $l > 0$. This requires that excitonic states be labelled by their total angular momentum $J = |s - l|, ..., |s + l|$. States are then characterized using atomic spectroscopy notation of $n\,{}^{\nu}L_J$, with multiplicity $\nu = 2s + 1$. The second part of this correction, H_{d2}, leads to an additional splitting of states and stops J from being a good quantum number. This forces eigenstates to be labelled by irreducible representations $\Gamma_{\mathrm{x}}^{\pm}$ of the O_{h} group. This amounts to taking the cubic nature of the crystal structure into account and is more significant for the green series than for the yellow series [103] owing to the larger spin of the hole.

The final term, H_{X}, corresponds to the exchange interaction between the electron and hole [103]. This only impacts even parity states as both the electron and hole must have a finite probability of being in the same unit cell. This only impacts states with an S-type symmetry and results in splitting to singlet ortho-exciton and triplet para-exciton states. For the yellow 1S exciton, these are separated by 12 meV. Direct recombination is forbidden for all orders for the para-exciton, owing to the requirement for a spin flip. This results in lifetimes of up to 12 µs [79]. This forbidden nature can be overcome through the application of stress [109] or external magnetic fields [110; 79]. Using SHG spectroscopy in the presence of magnetic fields up to $n = 6$ has been observed in the para exciton series [106].

Another impact of the exchange interaction is the change in D state energy levels [103]. As before the degeneracy is lifted, and the states with Γ_5^+ symmetry are shifted to higher energy. A consequence of this is the ${}^2D_{5/2}$ state is shifted to higher energy than the F states. Only the odd parity P states can be accessed via single photon spectroscopy. The even parity S and D states require an additional photon to access and are otherwise very weak [111; 112; 64; 113]. This thesis is primarily concerned with the yellow P series, but the S and D series are relevant for microwave-induced nonlinearities. This will be further discussed in the following section.

Only the states labelled as S, P, and D in Fig. 2.3 are relevant to this thesis. Borrowing notation from atomic physics they will be referred to throughout this thesis by S, P, and D with their irreducible symmetries being implied. Unlike hydrogen, experimental investigations have shown the different angular momentum exciton states at the same n are not degenerate [107; 114]. To account for the non-

degeneracy of the angular moment states a quantum defect model is employed [115]. This modifies the previous form for Rydberg energy levels by:

$$E_{\mathrm{nl}} = -\frac{R_{\mathrm{X}}}{(n-\delta_{\mathrm{l}})^2}, \tag{2.8}$$

where δ_{l} is the quantum defect. Alkali atoms have shown a weak dependence on energy for the quantum defect [116]. For alkali atoms, this originates in electronic shielding from inner electrons, whereas for excitons it originates from the non-parabolicity of the relevant energy bands. A similar dependence has been applied to excitonic states [115; 117; 118; 119; 120], but here we will ignore the n dependence of the quantum defect and treat it as a constant for each series.

So far, the discussion of correcting terms has focused on idealized crystal lattices that do not contain defects. These defects modify the unique structure of cuprous oxide [121; 122] and can modify the optical selection rules. These will be explored more fully in the following chapter.

2.3 The Excitonic Spectrum

Owing to the similarities in energetic structure between cuprous oxide and the archetypal atomic system it is perhaps unsurprising that the optical selection rules are similar. As a result, the spectra obtained from cuprous oxide are highly analogous to those extracted from archetypal atomic systems. The major differences between the spectra can be explained owing to the presence of phonons from the crystal lattice. Phonons broaden states and add additional absorption features and additional decay pathways. These will be explored throughout this section.

An archetypal transmission spectrum of cuprous oxide is shown in Fig. 2.4. The experimental setup used to obtain this will be detailed in the following chapter. The even parity of the valance band results in the odd parity P-type symmetry forming the most striking feature. These appear as a series of asymmetric peaks appearing closer and closer together towards the band edge. One might expect the F-type symmetry states to appear in this spectrum owing to their shared odd parity. However, these states have a much lower oscillator strength, resulting in a minimal contribution [114].

The excitonic states sit on top of a nonresonant background. This accounts for the majority of the absorption in the spectrum in Fig. 2.4. This originates in the

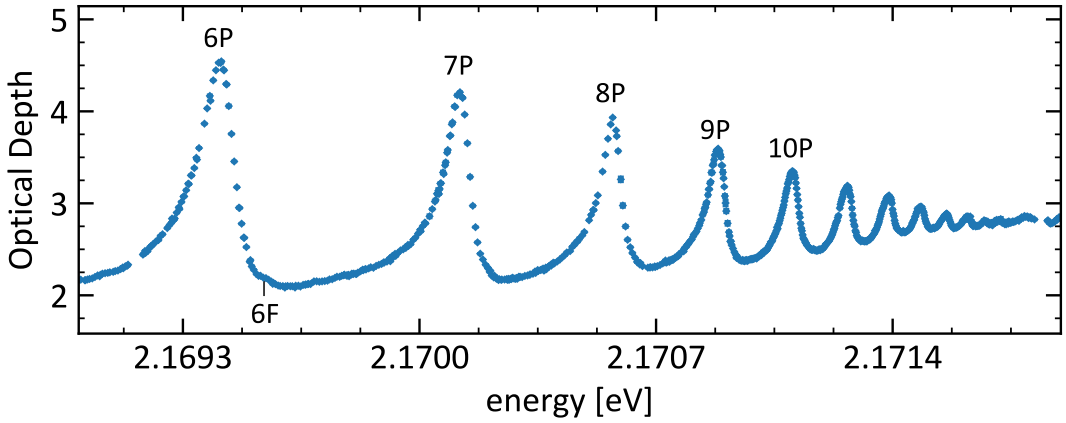

Figure 2.4: One photon absorption spectrum of excitons in sample AM at 4 °K was obtained using a tuneable narrowband laser. Details of the experimental procedure are given in chapter 4. The dominant features are the P states sitting on top of the square root-shaped phonon-assisted background.

creation of a 1S ortho-exciton alongside an odd-parity optical phonon. The square root dependence on energy of this background term originates in the density of phonon states [123; 124]. There is a contribution from both the green and yellow 1S ortho-excitons present here. The contribution for the yellow 1S begins around 2.05 eV while the contribution for the green kicks in at approximately 2.155 eV (between 2P and 3P). This contribution appears as a largely linear background for higher-lying excitonic states, such as those shown in Fig. 2.4.

The broad linewidths originate in exciton-phonon scattering [125; 126; 56]. The dominant contribution originates in the scattering of Rydberg states to 1S states via optical phonons. Scattering can occur by absorption or emission of optical phonons. However, the low-temperature environment experiments are carried out in limits the phonon population [56]. As a result only emission of phonons significantly contributes to the broadening.

The P series excitons are asymmetric, with steeper slopes on the high-energy side. This asymmetry arises due to the phonon-assisted generation of excitons [126; 125], whereby an exciton can be generated from an optical photon with lower energy more easily. This leads to a more gentle low-energy slope [127]. Other proposals have argued that this asymmetry is instead due to Fano resonances [108]. These arise due to the interference with the phonon-assisted background. The relative weighting of these two contributions remains unclear [56].

Towards the band edge, the absorption gains an exponential component known

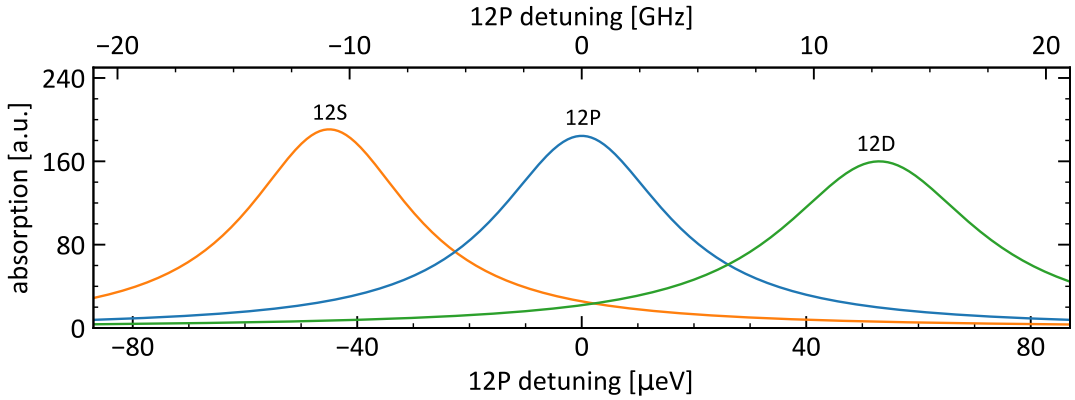

Figure 2.5: Schematic of the location and width of the $n = 12$ excitonic states. The 12P state overlaps with the 12S and 12D states resulting in a broad range of microwave frequencies being able to couple the opposite parity states to one another. The asymmetry of these states has been neglected in this diagram.

as the Urbach tail [128]. This smoothly transforms the spectrum from discrete exciton resonances to a continuum [129; 130]. The origin of this lies in charges within the material [131].

2.3.1 Microwave Transitions

Much like in atomic systems, it is possible to induce a transition between neighbouring angular momentum states by the application of an external field [5]. Rydberg systems offer the advantages of strong coupling to external fields via a large dipole moment. The exaggerated Bohr radius of cuprous oxide offers the same coupling at far lower n. Moreover, the broad nature of the excitonic states enables a much more broadband coupling between microwave and optical fields. This is illustrated in Fig. 2.5 for the $n = 12$ state. Here, the excitonic states overlap meaning that a microwave response can be detected at all detunings. The impact of this will be more fully explored in the 5^{th} and 6^{th} chapters of this thesis.

A consequence of the crystallographic structure of cuprous oxide is that we can only detect processes involving an odd number of photons. This will be expanded on in the following section. The energy levels involved in cuprous oxide further require that such processes involve a single laser photon and two microwave photons. This leads to three distinct excitation schemes, as illustrated in Fig. 2.6. These three processes are characterized by three different frequency responses. Two are

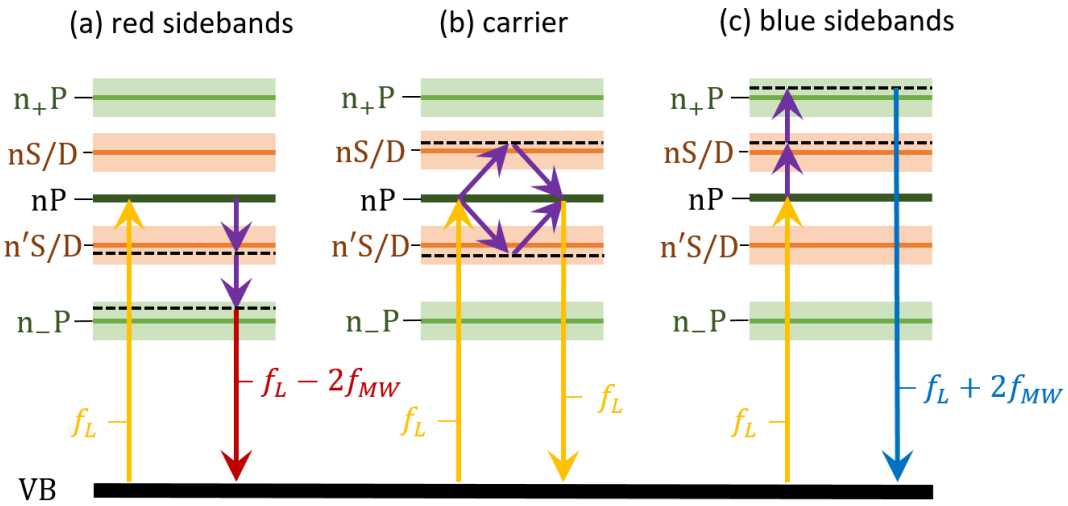

Figure 2.6: Energy level diagram of the three optical processes due to the application of microwave fields. Purple arrows correspond to microwave photons. Shaded regions illustrate the linewidth of the relevant state to show that the processes need not be resonant. Black dashed indicates the energies of the processes. (a) Creation of red sidebands by transitioning to a lower P-state via an intermediate S/D state. (b) Carrier light is modified by the creation of new components at the same frequency created through transitioning to and from neighbouring S/D states. The final P-state is the same as the initial state. (c) Creation of blue sidebands by transitioning to a higher P-state via an intermediate S/D state.

detuned from the laser frequency by two microwave frequencies. These correspond to transitions to a neighbouring P-state via an intermediate S/D state. The final process is where the final P state is either the same as the initial state or overlapping with the initial state. In either case, this results in the frequency being the same as the laser frequency.

The result of the broad linewidths and narrow spacing results in significant changes to the excitonic spectrum of cuprous oxide [74]. This is shown in Fig. 2.7. Not only does this modify the one-photon transmission, as indicated in Fig. 2.7(a), but it also leads to additional frequency components, as shown in Fig. 2.7(b). These additional components can be described using a nonlinear susceptibility model. This will incorporate the line widths and couplings between states to make predictions on the change in optical properties of cuprous oxide in the presence of a microwave field.

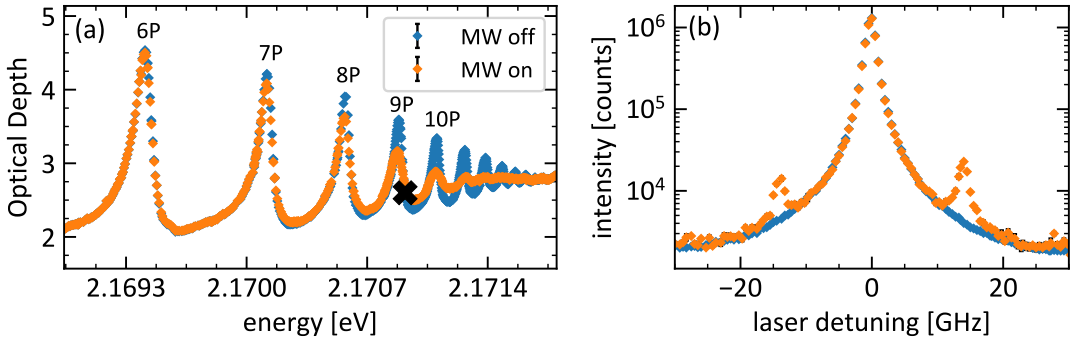

Figure 2.7: Variation in single photon transmission in the presence of a 75 mW microwave field with frequency 7 GHz. (a) the transmission of the spectrum is increased at P states and decreased between them. The effect of the microwave field becomes more pronounced for higher n. The black X shows correspond to the laser detuning (b) that was taken. (b) frequency resolving the transmission at 2.17091 eV. Of key note here is the addition of additional frequency terms at plus or minus twice the frequency of the microwave field.

2.4 Electronic Susceptibility

The optical response of a material can be described in terms of the complex-valued susceptibility χ [61]. The susceptibility describes the polarisation, $\tilde{\mathbf{P}}$, induced within a material by an external field, $\tilde{\mathbf{E}}$, by:

$$\tilde{\mathbf{P}} = \epsilon_0(\chi^{(1)}\tilde{\mathbf{E}} + \chi^{(2)}\tilde{\mathbf{E}}\tilde{\mathbf{E}} + \chi^{(3)}\tilde{\mathbf{E}}\tilde{\mathbf{E}}\tilde{\mathbf{E}} + ...), \tag{2.9}$$

where $\chi^{(1)}$ is the linear susceptibility and $\chi^{(m)}$ is the m^{th} order nonlinear susceptibility. The tilde notation on field terms is used to explicitly show the time dependence of those fields. The vector nature of light requires that $\chi^{(m)}$ is a tensor of rank $m+1$. Each term in the above expansion corresponds to a field generated within the material, referred to as the m^{th} order nonlinear polarization. The centrosymmetric nature of cuprous oxide results in all even-order nonlinearities going to zero. As a result, the lowest order nonlinearity results from the $\chi^{(3)}$ term.

This thesis is concerned with the modifications to the optical properties of cuprous oxide in the presence of a microwave field. To that end, the field applied across the sample takes on the following form:

$$\tilde{\mathbf{E}} = \tilde{\mathbf{E}}_{\mathrm{L}}(\omega) + \tilde{\mathbf{E}}_{\mathrm{MW}}(\Omega), \tag{2.10}$$

where $\tilde{\mathbf{E}}_{\mathrm{L}}(\omega)$ is the laser field with frequency ω and similarly $\tilde{\mathbf{E}}_{\mathrm{MW}}(\Omega)$ is the microwave field with frequency Ω. The fields are modelled as plane waves of the form:

$$\tilde{\mathbf{E}} = \mathbf{E}_0 \exp(i\omega t + i\mathbf{k}\cdot\mathbf{r}) + c.c., \tag{2.11}$$

where ω is the frequency, $\mathbf{k}$ is the wavevector, $\mathbf{E}_0$ is the electric field strength, and *c.c.* denotes the associated complex conjugate. Taking the product of electronic fields in eqn. 2.9 results in additional frequency components being introduced to the polarisation. In fully nonresonant media these different frequency components have the same strength. This is because there is no resonance condition that will enhance any one of the processes. To capture resonant structure we use a frequency dependent χ which is a function of the frequencies of the involved fields. For example, a third-order nonlinearity involving one laser photon and two microwave photons would be written as:

$$\tilde{\mathbf{P}}^{(3)}(\omega + 2\Omega) = \chi^{(3)}(\omega + 2\Omega, \omega, \Omega, \Omega)\tilde{\mathbf{E}}_{\mathrm{L}}\tilde{\mathbf{E}}_{\mathrm{MW}}\tilde{\mathbf{E}}_{\mathrm{MW}}, \tag{2.12}$$

where the first argument in $\chi^{(3)}$ is the frequency of the polarisation and the remaining arguments are the frequencies of the involved fields.

Many physical properties of the system can be described in terms of the susceptibility. Thus knowing the functional form of χ enables predictions to be made of the optical response of the material. In atomic physics, it is possible to derive this form using quantum mechanics. These expressions are built on the energy levels, line widths, and dipole matrix elements for transitions between energy levels. This is comprehensively derived in [61]. These forms have been used to describe the nonlinear optical processes of excitons [132]. The following sections will lay out the functional form of the susceptibility used to describe the processes in cuprous oxide. We will start by exploring the role of different frequency components arising from $\chi^{(3)}$.

2.4.1 Frequency Components of $\chi^{(3)}$

The $\chi^{(3)}$ term describing the mixing of a microwave and laser field contains a large number of different frequency components. These correspond to all the possible permutations of adding or subtracting the microwave and laser frequencies. In this thesis, we are only concerned with components at the laser frequency or detuned from it by twice the microwave frequency. This amounts to only considering

third-order polarisations described by:

$$\tilde{\mathbf{P}}^{(3)} = \epsilon_0 \chi^{(3)} \tilde{\mathbf{E}}_{\mathrm{L}} \tilde{\mathbf{E}}_{\mathrm{M}} \tilde{\mathbf{E}}_{\mathrm{M}}, \tag{2.13}$$

owing to the resonance conditions enforced by the yellow excitons. Any processes containing two laser fields will be very far detuned from any excitonic states and so will not contribute significantly. Furthermore, the detection system is only able to frequency resolve signals within a few GHz of the laser frequency. The three frequencies involved in this process correspond to three distinct processes. The first is at $\omega+2\Omega$ corresponding to frequency sum generation. Similarly, there is another term at $\omega - 2\Omega$ which relates to frequency difference generation. The final frequency is at ω which corresponds to a cross-Kerr effect. The Kerr effect term modulates the amplitude and phase of the transmitted light. It is the Kerr effect that will form the primary focus of the following section, and a major focus of this thesis is to measure the AC cross Kerr effect in cuprous oxide.

2.4.2 The form of $\tilde{\mathbf{P}}^{(3)}$

The form of the nonlinear polarisation can be identified by placing the form of the electronic fields into eqn. 2.13. To simplify this expression both the tensor nature and frequency dependence of $\chi^{(3)}$ will be neglected. These are taken into account when the explicit form of $\chi^{(3)}$ is evaluated. Furthermore, the spatial dependence of the fields will not be explicitly written in the following algebra. Doing so results in $\tilde{\mathbf{P}}^{(3)}$ taking the following form:

$$\tilde{P}^{(3)} = \epsilon_0 \chi^{(3)} \mathrm{E}_{\mathrm{L}}^0 e^{-i\omega t}(e^{-i2\Omega t} + e^{i2\Omega t} + 2)|\mathrm{E}_{\mathrm{MW}}^0|^2 + c.c., \tag{2.14}$$

where E_L^0 is the laser field strength and $\mathrm{E}_{\mathrm{MW}}^0$ is the microwave field strength. By noting the complex form of cosine and making use of the identity $\cos(2x) = 2\cos^2(x) - 1$ the above expression becomes:

$$\tilde{P}^{(3)} = 4\epsilon_0 \chi^{(3)} E_{\mathrm{L}}^0 e^{-i\omega t} \cos^2(\Omega t)|E_{\mathrm{MW}}^0|^2 + c.c., \tag{2.15}$$

which in turn can be re-written in terms of the intensity of the microwave field, defined as $I_{\mathrm{MW}} = 2\epsilon_0 n_0 c|E_{\mathrm{MW}}^0|^2$, with refractive index n_0, leading to:

$$\tilde{P}^{(3)} = \frac{2\chi^{(3)}}{n_0 c} E_{\mathrm{L}}^0 e^{-i\omega t} I_{\mathrm{MW}} \cos^2(\Omega t) + c.c. \tag{2.16}$$

By then inserting this result into our form for the polarization inside the medium we arrive at:

$$\tilde{P}^{(3)} = (\epsilon_0\chi^{(1)} + \frac{2\chi^{(3)}}{n_0 c} I_{\mathrm{MW}} \cos^2(\Omega t))E_L = \chi_{\mathrm{eff}} E_{\mathrm{L}}^0 e^{-i\omega t}, \tag{2.17}$$

which describes the nonlinear contribution as a modification to the linear susceptibility of the material. By noting that the susceptibility is related to the refractive index through:

$$n^2 = \chi + 1. \tag{2.18}$$

Thus, it is clear that the modulation to the polarization which originates from $\chi^{(3)}$ is a modulation to the refractive index. In the next section, we will explore how to relate the real and imaginary parts of $\chi^{(3)}$ to the real and imaginary parts of the nonlinear refractive index.

2.4.3 Relating χ to optical Properties

The optical properties of a material can be described by the complex refractive index, $\bar{\mathrm{n}}$. This captures both the absorption and refraction of light within media. This can be understood by recalling how the wave vector relates to the refractive index:

$$k = \bar{n}\frac{\omega}{c} = \bar{n}k_0, \quad \bar{n} = n + i\kappa, \tag{2.19}$$

where k_0 is the wave vector in a vacuum and κ describes the absorption, α, within a material. When this is placed into the expression for a propagating field it is clear that the imaginary part describes an absorptive term

$$\tilde{\mathbf{E}} = \mathbf{E}_0 \exp\{(i\omega t - ikr)\} = \mathbf{E}_0 \exp\{(i\omega t + ink_0 r)\exp(-k_0\kappa r)\}, \tag{2.20}$$

where the final exponential term is the absorptive term. The modification to the refractive index is taken into account through the introduction of nonlinear refractive indices:

$$\begin{aligned} n &= n_0 + n_2 I_{\mathrm{MW}} = n_0 + \Delta n, \\ \kappa &= \kappa_0 + \kappa_2 I_{\mathrm{MW}} = \kappa_0 + \Delta\kappa, \end{aligned} \tag{2.21}$$

where n_2 and κ_2 described the strength of the nonlinearity, n_0 and κ_0 are the linear refractive indices and I_{MW} is the intensity of the associated microwave field. In

weakly absorbing material, such as cuprous oxide, the real and imaginary parts of $\chi^{(3)}$ relate directly to the nonlinear refractive indices [61] by:

$$\chi_R^{(3)} = (4/3)n_0^2\epsilon_0 c n_2, \tag{2.22}$$

$$\chi_I^{(3)} = (4/3)n_0^2\epsilon_0 c \kappa_2, \tag{2.23}$$

allowing for predictions of the amplitude of the Kerr effect, and corresponding phase shift, to be made.

2.4.4 The Kerr Coefficient

Placing the nonlinear refractive indices into the form of the propagating electric field results in:

$$E^{out} = \epsilon_0 E_{\mathrm{L}}^0 \exp[i(n_0 kz - i\omega_{\mathrm{L}} t)] \exp\Big(i n_2 I_{\mathrm{MW}} \cos^2(\Omega t)\frac{\omega}{c} z\Big) \exp\Big(-\frac{z}{\delta}\Big), \tag{2.24}$$

where δ has been defined according to $\frac{1}{\delta} = n_0 \frac{\omega_L}{c} z(\kappa_0 + \kappa_2 I_{\mathrm{MW}} \cos^2(\Omega t))$. This accounts for the amplitude modulation. The first exponential term in the above expression is the un-modified wave. The second term is the modulation to the phase and the third is the modulation to the transmission. The role of phase modulation is to change the refractive index of the material. Physically, this can be thought of as a speeding up or slowing down of the transmitted wave. This introduces additional frequency components indicated in Fig. 2.8.

The form of the additional frequency components can be shown by rewriting the phase modulation term from eqn. 2.24. Using $\beta = n_2 kz\epsilon_0 n_0 c|E_{\mathrm{MW}}|^2$ phase term becomes:

$$\exp\Big[i2\beta\cos^2(\Omega t)\Big] = \exp[i\beta(1+\cos(2\Omega t)], \tag{2.25}$$

which can in turn be expanded using the Jacobi-Anger expansion to obtain the following expression for the transmitted light:

$$E^{\mathrm{out}} = \tilde{E}^L e^{i\beta}(J_0(\beta) + iJ_1(\beta)e^{i2\Omega t} - iJ_1(\beta)e^{-i2\Omega t})e^{-z/\delta}, \tag{2.26}$$

which contains three field terms arising from the phase modulation. Here only the first two additional frequency terms have been used, which corresponds to a weak external field. These frequency terms correspond to a field at the laser frequency and two fields detuned by 2Ω from the laser frequency. This effect is illustrated in Fig. 2.8(b).

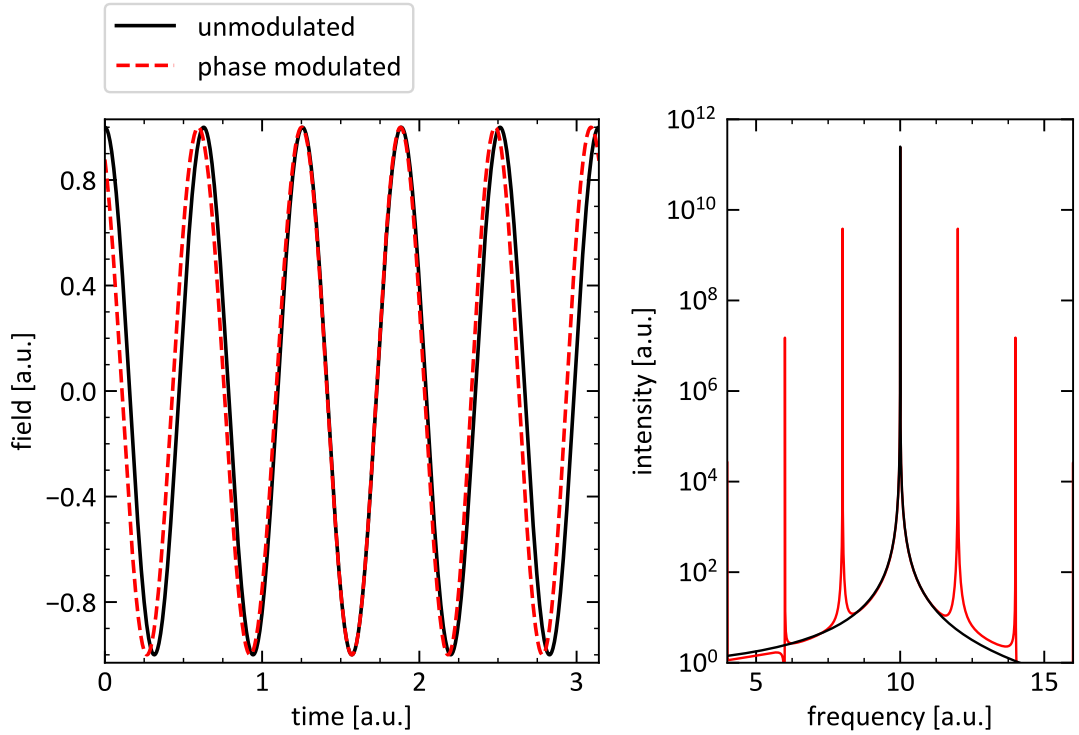

Figure 2.8: The effects of phase modulation on a wave. Left: the modulation results in lagging and speeding up the modified wave. Right: additional frequency components are introduced to the spectrum.

These detuned frequency terms appear as sidebands on the main carrier frequency and can be detected using a Fabry-Perot etalon, as described in Chapter 5. The phase change is determined by taking the ratio of the sideband signal to the carrier signal when no microwaves are applied:

$$\frac{I_{\mathrm{SB}}}{I_{\mathrm{Car}}} = \left|\frac{J_1(\phi)}{J_0(0)}\right|^2, \tag{2.27}$$

where ϕ is the corresponding phase shift. As the Bessel function is normalized the right-hand side of the above equation simplifies to $|J_1(\phi)|^2$. Thus the phase shift is extracted by finding the inverse of this function computationally. A flaw with this approach is that it is not able to distinguish between sidebands generated by phase modulation from sidebands generated by amplitude modulation. Here, both processes can produce sidebands detuned from the laser frequency by twice the microwave frequency. To account for this data is collected at points in the spectrum where the change in amplitude is zero, such that sidebands come purely from phase modulation as shown in Fig. 2.7(b), where there is no change to the carrier component due to the external microwave field.

A further complication is that we have assumed that $\chi^{(3)}$ does not depend on the frequency of the involved fields to derive the Bessel function form given in eqn. 2.26. This can be done using the functional form of χ laid out in the following section.

2.4.5 Functional form of χ

To make quantitative predictions of the optical properties of cuprous oxide we required the form of the susceptibility χ. This work will use an atomic model based on matrix transition elements, line widths, and energy levels to achieve this. Under single-photon excitation, the susceptibility near to an isolated nP state is given by:

$$\chi_{\mathrm{nP}} = \frac{N}{\epsilon_0 \hbar} \frac{|D^{\mathrm{VB}\rightarrow\mathrm{nP}}|^2}{\delta_{\mathrm{nP}} - i\Gamma_{\mathrm{nP}}}, \tag{2.28}$$

where $|D^{\mathrm{VB}\rightarrow\mathrm{nP}}|^2$ is the dipole moment per unit volume for the transition from the valence band to the nP state, N is the number density of the excitons, δ_{nP} is the detuning from the state energy level given by $\hbar\omega - E_{\mathrm{nP}} - \hbar\Omega$, for state energy E_{nP} [3]. Γ_{nP} is the linewidth, defined here as the half width half maximum (HWHM). A full derivation of this can be found in chapter 3 of [61]. Here, we have taken the rotating wave approximation, which amounts to considering only frequencies near to δ_{nP} making significant contributions to χ_{nP}. The result of the imaginary prefactor in front of Γ_{nP} is that taking the imaginary part of χ_{nP} results in a Lorentzian lineshape.

The real and imaginary parts of the refractive index, n and κ respectively, are related to the the electronic susceptibility according to eqn. 2.19. An interesting impact of this is that near resonance there is a decrease in the refractive index of light n with increasing frequency, the opposite of how n normally behaves. This is known as anomalous dispersion and occurs around any highly absorptive feature. Of course, around resonance, we see a significant increase in κ corresponding to the increase in absorption [61].

This model does not take into account the asymmetry of the nP states. For high principal quantum numbers it is no longer appropriate to treat the exciton resonances as isolated. This results from the states beginning to overlap. Here the susceptibility is instead a sum over all principal quantum numbers:

$$\chi = \sum_n \frac{N}{\epsilon_0 \hbar} \frac{|D^{VB\rightarrow nP}|^2}{\delta_{\mathrm{nP}} - i\Gamma_{\mathrm{nP}}}, \tag{2.29}$$

which is now able to reproduce the odd parity yellow excitonic series. The energy levels, line widths, and dipole matrix elements are determined by fitting measured transmission spectra.

To expand this to the nonlinear optical regime knowledge of the nS and nD states is required. The corresponding line widths and energies can be obtained by fitting the SHG spectrum. This has been carried out in previous work by this group [74; 84]. The form of the nonlinear susceptibility is similarly given by:

$$\chi^{(3)}(\omega_L \pm \Omega \mp \Omega) = \sum_{n,n',l,\pm} \frac{N}{\epsilon_0 \hbar} \frac{|\mathrm{D}^{\mathrm{VB}\Rightarrow \mathrm{nP}}|^2 D^{\mathrm{nP}\Rightarrow \mathrm{n'l}} D^{\mathrm{n'l}\Rightarrow \mathrm{n''P'}}}{(\delta_{\mathrm{nP}} - i\Gamma_{\mathrm{nP}})(\delta_{\mathrm{n'l}} - i\Gamma_{\mathrm{n'l}} \pm i\Omega)(\delta_{\mathrm{n''P'}} - i\Gamma_{\mathrm{n''P'}})}, \tag{2.30}$$

where the sum describes the coupling of an initial nP state to a final $n''P'$ state through an intermediate $n'l$ state, this sum is performed over all intermediate states owing to the broad linewidths involved. The detuning to the first $n'l$ state is modified by the addition or subtraction of a microwave field. This describes the nonlinear susceptibility at the frequency of the laser. The other two processes are described by a similar expression where the detuning of the final nP state is modified by 2Ω. These processes are schematically indicated in Fig. 2.6. Further details on this model are provided in Appendix B.

This corresponds to evaluation in three different regimes. The first is where the final nP state is the same as the initial state, or where a neighboring nP state overlaps with the initial state. This corresponds to the polarisations which are at the frequency of the carrier. The other two regimes are at plus or minus two microwave frequencies from the carrier. The transition matrix elements are calculated based on an exciton-polariton model neglecting the asymmetry of the excitonic states. These calculations were performed by Valantin Walter and more details on these calculations can be found in [74; 49], as well as in Appendix A.

Using this functional form it is possible to make quantitative predictions for the optical properties of cuprous oxide. This will be fully explored during the 5^{th} chapter. The limitations of this model and the requirement to extend to 5^{th}-order nonlinear polarisations will be explored in the 6^{th} chapter. We now turn our attention to addressing the tensor nature of the crystal structure.

Having the functional form of $\chi^{(3)}$ allows us to investigate the validity of the assumption that $\chi^{(3)}$ is the same in the three frequency regimes we are concerned with. These are the laser frequency, ω, and the red detuned frequency. $\omega - 2\Omega$,

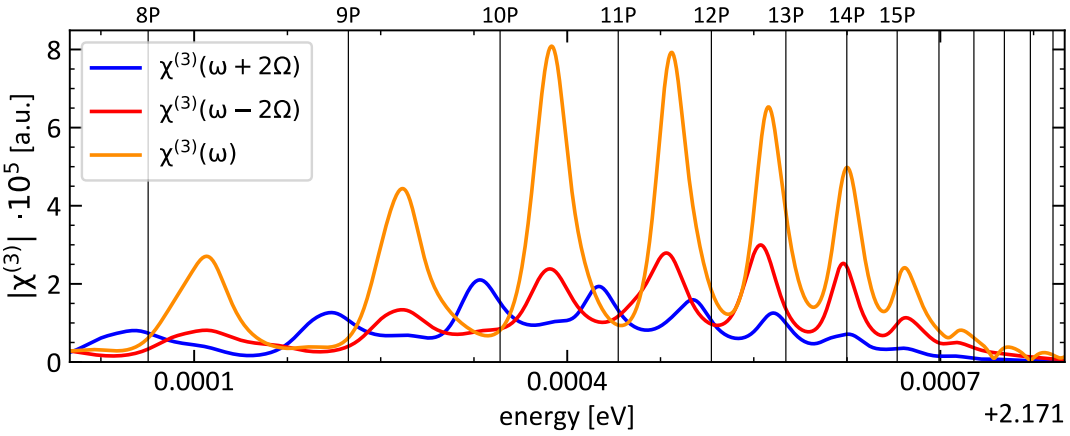

Figure 2.9: Comparison between calculated values of $\chi^{(3)}$ evaluated in the three relevant frequency regimes. Here, ω is the frequency of the laser while Ω is the frequency of the microwave field. Vertical black lines indicate the location of excitonic resonances. All of the curves show a similar structure of peaks but with some different locations. Notably, the orange curve, corresponding the $\chi^{(3)}$ at the frequency if the laser, is larger than the other two.

and then the blue detuned frequency, $\omega + 2\Omega$. The calculated values for these different frequency regimes are shown in Fig. 2.9. The values themselves are found by computing the sum in eqn. 2.30. While the structure of the three regimes in which $\chi^{(3)}$ were evaluated are different, the order of magnitude of the three regimes is similar. This is particularly true for the red and blue detuned evaluations. However, the clear deviations lead to the method of extracting a phase from the intensity of the sidebands as only being an estimation.

2.4.6 Crystal Structure and Susceptibility

Unlike atomic systems, cuprous oxide is not isotropic. As a result, the orientation of the crystal can play a role in the nonlinear susceptibility, and the tensor nature must be taken into account. Doing so will enable further insight into the matrix elements of $\chi^{(3)}$ to be experimentally determined by resolving the polarisation state of transmitted light. Furthermore, it allows for comparisons to be made between different experiments based on this material wherein the orientation of samples may not be the same.

$\chi^{(3)}$ is a rank 4 tensor, which contains up to 81 independent elements. This results in evaluating eqn. 2.13 becoming a highly involved task. However, the

symmetries of cuprous oxide result in only 21 of these elements taking non-zero values. Of which only four are independent and are related by the following set of equations:

$$\begin{aligned}
&\chi^{(3)}_{\mathrm{xxxx}} = \chi^{(3)}_{\mathrm{yyyy}} = \chi^{(3)}_{\mathrm{zzzz}},\\
&\chi^{(3)}_{\mathrm{yyzz}} = \chi^{(3)}_{\mathrm{zzyy}} = \chi^{(3)}_{\mathrm{zzxx}} = \chi^{(3)}_{\mathrm{xxzz}} = \chi^{(3)}_{\mathrm{xxyy}} = \chi^{(3)}_{\mathrm{yyxx}},\\
&\chi^{(3)}_{\mathrm{yzyz}} = \chi^{(3)}_{\mathrm{zyzy}} = \chi^{(3)}_{\mathrm{zxzx}} = \chi^{(3)}_{\mathrm{xzxz}} = \chi^{(3)}_{\mathrm{xyxy}} = \chi^{(3)}_{\mathrm{yxyx}},\\
&\chi^{(3)}_{\mathrm{yzzy}} = \chi^{(3)}_{\mathrm{zyyz}} = \chi^{(3)}_{\mathrm{zxxz}} = \chi^{(3)}_{\mathrm{xzzx}} = \chi^{(3)}_{\mathrm{xyyx}} = \chi^{(3)}_{\mathrm{yxxy}},
\end{aligned} \tag{2.31}$$

reducing the complexity significantly. In the above expression, the indices correspond to the physical dimensions of the electronic field. The above symmetries are very similar to the isotropic case. This reflects the similarities to the isotropic case further supporting the use of a hydrogenic model in the previous section. A further simplification to the form of nonlinear polarisation arises due to the indistinguishability of the two microwave photons involved. This results in $\chi^{(3)}$ being unchanged if its final two indices are exchanged:

$$\chi^{(3)}_{\mathrm{xyyx}} = \chi^{(3)}_{\mathrm{xyxy}}, \tag{2.32}$$

which further reduces independent elements of $\chi^{(3)}$ down to three:

$$\chi^{(3)}_{\mathrm{xxxx}}, \quad \chi^{(3)}_{\mathrm{xxyy}}, \quad \chi^{(3)}_{\mathrm{xyyx}}. \tag{2.33}$$

A further complication when considering the tensor nature of $\chi^{(3)}$ arises from the choice of reference frame. In the above expressions, the coordinates are with respect to the crystal frame, not the lab frame. To transform between the two frames we make use of a transform matrix T defined such that:

$$E' = \mathrm{T}E, \tag{2.34}$$

where E is the electric field in the lab frame and E' is the electric field in the crystal frame. The crystals used in this thesis are orientated to the [111] crystal plane. Further details on this experimental setup can be found in Chapter 5. In the lab frame, the polarisation of the laser field $\mathrm{E_L}$ and microwave field $\mathrm{E_M}$ are defined by:

$$\mathrm{E_L} = \begin{pmatrix} \cos(\theta) \\ \sin(\theta) \\ 0 \end{pmatrix}, \quad \mathrm{E_{MW}} = \begin{pmatrix} 1 \\ 0 \\ 0 \end{pmatrix}, \tag{2.35}$$

where θ is the angle between the plane of polarisation of the linearly polarised light and the vertical axis. The microwave fields are applied across the sample

utilizing a stripline antenna, again further details can be found in Chapter 5. Here, the microwave field is assumed to be well-polarised along the x-direction. The desired transformation matrix will transform the orthonormal basis vectors according to:

$$\begin{pmatrix}1\\0\\0\end{pmatrix} \Rightarrow \frac{1}{\sqrt{2}}\begin{pmatrix}1\\-1\\0\end{pmatrix}, \quad \begin{pmatrix}0\\1\\0\end{pmatrix} \Rightarrow \frac{1}{\sqrt{6}}\begin{pmatrix}1\\1\\-2\end{pmatrix}, \quad \begin{pmatrix}0\\0\\1\end{pmatrix} \Rightarrow \frac{1}{\sqrt{3}}\begin{pmatrix}1\\1\\1\end{pmatrix}, \tag{2.36}$$

the key here is the transformation of the z-axis to the [111] axis. This results in the form of the transformation matrix being:

$$\mathrm{T} = \begin{pmatrix} \frac{1}{\sqrt{2}} & \frac{1}{\sqrt{6}} & \frac{1}{\sqrt{3}} \\ \frac{-1}{\sqrt{2}} & \frac{1}{\sqrt{6}} & \frac{1}{\sqrt{3}} \\ 0 & \frac{-2}{\sqrt{6}} & \frac{1}{\sqrt{3}} \end{pmatrix}, \tag{2.37}$$

with each column corresponding to the target vector. The transformation can be clearly understood by applying this to a single basis vector from the lab frame. However, we have not taken into account that the crystal can be at an angle α with respect to the polarisation of the laser field. To take this into account we utilize the rotation matrix $\mathrm{R_z}(\alpha)$ which is defined by:

$$\mathrm{R_z}(\alpha) = \begin{pmatrix} \cos(\alpha) & -\sin(\alpha) & 0 \\ \sin(\alpha) & \cos(\alpha) & 0 \\ 0 & 0 & 1 \end{pmatrix}, \tag{2.38}$$

to further transform the basis vectors. Thus to transform from the lab frame to the crystal frame the full transformation is given by $\mathrm{T}' = \mathrm{R_z}(\alpha)\mathrm{T}$. Following this transformation $\tilde{\mathbf{P}}^{(3)}$ is evaluated in the crystal frame and then transformed back to the lab frame via. Thus the nonlinear polarisation is given by:

$$\tilde{\mathbf{P}}^{(3)} = T^{-1}\chi^{(3)}\tilde{\mathbf{E}}'^{\mathrm{L}}\tilde{\mathbf{E}}'^{\mathrm{MW}}\tilde{\mathbf{E}}'^{\mathrm{MW}}, \tag{2.39}$$

The transformation back removes any dependence on α, and results in the following form for the polarization:

$$\mathbf{P}^{(3)} = \begin{pmatrix} \frac{1}{2}(\chi_{\mathrm{xxxx}} + \chi_{\mathrm{xxyy}} + 2\chi_{\mathrm{xyyx}})\cos(\theta) \\ \frac{1}{6}(\chi_{\mathrm{xxxx}} + 5\chi_{\mathrm{xxyy}} - 2\chi_{\mathrm{xyyx}})\ \sin(\theta) \\ 0 \end{pmatrix}. \tag{2.40}$$

The transformation back to the lab frame is required because that is the frame in which the polarisation is detected. The electronic field $\tilde{\mathbf{E}}$, which has a frequency

ω, generated by the nonlinear polarisation is obtained by solving Maxwell's equations for a nonmagnetic material with no free charge or current [61]:

$$-\nabla^2\tilde{\mathbf{E}} + \frac{\epsilon^{(1)}(\omega)}{c^2}\frac{\partial^2\tilde{\mathbf{E}}}{\partial t^2} = -\frac{1}{\epsilon_0 c^2}\frac{\partial^2\tilde{\mathbf{P}}^{\mathrm{NL}}}{\partial t^2}, \tag{2.41}$$

where $\epsilon^{(1)}(\omega_{\mathrm{n}})$ is the complex-valued frequency-dependent dielectric tensor which relates the linear displacement field $\tilde{\mathbf{D}}^{(1)}$, to the electronic field $\tilde{\mathbf{E}}$ by:

$$\tilde{\mathbf{D}}^{(1)} = \epsilon_0\epsilon^{(1)}(\omega)\tilde{\mathbf{E}}, \tag{2.42}$$

where the full displacement field $\tilde{\mathbf{D}}$ is related to the nonlinear polarisation $\tilde{\mathbf{P}}^{\mathrm{NL}}$ according to:

$$\tilde{\mathbf{D}} = \tilde{\mathbf{D}}^{(1)} + \tilde{\mathbf{P}}^{\mathrm{NL}}, \tag{2.43}$$

which describes the change in charge distribution due to the induced polarisation. Solving eqn. 2.41 yields fields with the same polarisation state as the polarisation induced within the material. As such, determining the polarisation state of the outgoing light can shed light on the value of the elements of $\chi^{(3)}$. This will be studied further in chapter 5.

2.5 Conclusions

This chapter has explored the optical properties of cuprous oxide around the edge of the band gap. Making use of the effective mass approximation allowed for electrons and holes to be treated as free particles. This in turn results in the system being described by a hydrogenic Hamiltonian giving rise to the familiar atomic energy levels. By then taking a series of corrections into account, which amount to a quantum defect model, the excitonic spectrum of cuprous oxide is obtained. This in turn is further modified by the presence of phonons in the crystal. Phonons contribute to the asymmetry, linewidth, and broad background seen in transmission spectra. Such a spectrum has broad excitonic resonances which overlap with one another. A major consequence of this spacing is that it is an ideal platform for exploring microwave-to-optical conversion.

Following an analogous approach to atomic physics, an electronic susceptibility model was built to describe the linear and nonlinear processes in cuprous oxide. By taking the geometry of the crystal into account the change in the polarisation

state of transmitted light was determined. Alongside this, a model describing the change in absorption and phase of the transmitted light due to microwaves was developed. Together this allows for a thorough description of the optical process in cuprous oxide.

The phase change is of particular note as it corresponds to an enormous Kerr coefficient. This can be experimentally determined using a Fabry-Perot etalon (FPE) by comparing the size of the sidebands to the carrier signal at a range of microwave powers.

Chapter 3

Sample Characterisation

To take advantage of the attractive properties offered by cuprous oxide there is a need to develop high-quality synthetic samples. Presently, much of the novel physics has only been demonstrated using naturally sourced cuprous oxide [58; 59; 133]. The fact that virtually all of the high-quality natural samples come from the same mine, specifically the Oganja mine in Tsumeb [134], highlights the finite nature of the resource. Taken together these factors limit the scalability of the physics observed in cuprous oxide for technological applications. As such, we seek to identify a suitable method for characterizing, and improving, the quality of synthetic samples.

The quality of a material is a measure of deviation from the ideal makeup for an intended purpose. For example, within the world of jewellery, a higher quality diamond would have fewer flaws than a lower quality one [135]. In this case, the quality is directly measured by inspecting the sample. For this thesis, the measure of quality of cuprous oxide is the highest principal quantum number exciton which can be observed. However, such a measurement does not provide information as to what is limiting the quality of the sample. A potential limitation to sample quality comes in the form of vacancies in the crystal lattice. These provide charge traps enabling additional channels for excitons to recombine, preventing the observation of high principal quantum numbers [121]. In particular, the density of copper vacancies has been observed to be notably higher in synthetic material, providing a possible candidate for a limiting factor [136; 137]. However, it remains unclear how exactly the presence of vacancies affects the excitonic states. That being said, recent work has shown that the creation of free charges can neutralise the charged defects within a crystal. Doing so improves the absorption spectrum but

does not enable observation of higher nP excitons [138].

Synthetically grown samples are of a far lower quality than their natural counterparts. The highest principal quantum number exciton observed in synthetic material is 10P [83] as opposed to 30P in natural samples [59]. Intuitively, this difference in quality can be understood by considering how the different samples are formed. Natural samples form by hydrothermal oxidation over long periods of time [139]. Whereas synthetic samples are formed in hours or days. It is perhaps not surprising that such a rapid formation process does not lead to the ideal crystal structure.

Synthetic cuprous oxide can be grown by several different methods. Crystal structures be grown through a variety of different mechanisms such as electrodeposition [140; 141; 142], thermal oxidation [137; 143], molecular beam epitaxy (MBE) [144] and the floating zone method (FZM) [145; 146]. The synthetic samples used in this thesis were grown via the FZM in India by Ravi Signh [83]. This technique was selected owing to its capability to rapidly generate large amounts of phase pure material in a short span of time. The key parts of this process are the oxidation of a copper rod followed by a purification step using a floating zone furnace. The result of this is a 10 mm wide rod of cuprous oxide that is 10s of cm long. Further details can be found in [83].

One avenue for the removal of vacancies from synthetic cuprous oxide is through thermal annealing [121; 147]. Heating the sample enables the crystal structure to relax into a lower energy state, with fewer vacancies. Thus thermal annealing of synthetic samples may improve their quality. Here I will present a characterization of both natural and synthetic stones before illustrating the effect of thermal annealing on synthetic stones to determine if it can be used to improve their quality. Samples will be characterized using room-temperature photoluminescence (PL) spectroscopy to probe defect densities. This method is not only simple to utilize but offers a high throughput. As such, multiple samples can be characterized without the long cooling times associated with cryogenic experiments.

3.1 Experimental Setup

To determine the impact of copper vacancies on the quality of a sample we require two separate experiments. The first will probe the density of copper vacancies while the second will measure the sample quality by examining the excitonic spectrum. Copper vacancy density will be measured using a room temperature PL setup, while cryogenic transmission spectroscopy is used to probe the excitonic states. Both of these setups are described in this section alongside the relevant physics.

3.1.1 Sample Preparation

Different samples from the same original gemstone were separately prepared for PL and transmission spectroscopy. The reason for this is the absorptive nature of cuprous oxide requires thin samples to be used for transmission spectroscopy. In this work samples were generally 100 µm thick. Additionally, the samples must be highly polished on both sides to reduce random scattering of transmitted light. Together, these lead to fragile samples prone to breaking during the mounting and un-mounting process. Whereas, for PL spectroscopy spectra are obtained from the surface of a sample. This removes the requirement for thin samples allowing much larger ones to be used instead. Furthermore, samples do not require the same high level of polish, again owing to the spectra being collected from the surface of the sample. Thus, to avoid damaging the fragile samples required for transmission spectroscopy it is practical to prepare samples separately.

For transmission spectroscopy samples were sliced and mechanically polished by the thin section laboratory in the Earth Sciences department at Durham University. This involves the mechanical polishing of samples down to a finishing with 0.25 µm DiaPro solution. Further details on the crystallographic orientation and polishing of samples can be found in [55].

For PL spectroscopy the surface of the samples was polished by hand on a glass plate. A rough polish was achieved using a 50 µm SiC pad followed by a 10 µm SiC pad. Following this a fine polish was achieved using a DP-NAP cloth together with decreasing size AlO_3, starting with a 5 µm powder solution followed by a 0.5 µm powder solution.

Broadly speaking samples are mounted in the same way for both techniques. For PL spectroscopy samples were stuck to the surface of a glass microscope slide using nail varnish. This was used instead of a more firm adhesive, such as super glue, to reduce the strain on the sample as the glue dries. Similarly, for transmission spectroscopy samples were stuck to CaF_2 windows using nail varnish. However, owing to the thinner nature of the samples only a single corner was stuck down using the varnish. This was again in an effort to reduce the strain across the sample, which is more important in the low temperature environment. The procedures described above were applied to both natural and synthetic samples in the same way.

3.1.2 Photoluminescence Spectroscopy

Energetically speaking, above-band gap optical excitation creates an electron-hole plasma. This leads to the formation and subsequent decay of 1S excitons. Owing to the symmetry of the band structure, 1S excitons cannot directly recombine. As such they undergo phonon-assisted recombination by absorbing or emitting a thermal phonon [124]. Owing to the thermal distribution of phonon energies the 1S recombination lineshape is characterised by a Maxwell-Boltzmann (MB) distribution:

$$I = \sqrt{(E - E_0)} e^{\frac{-(E-E_0)}{K_b T}}, \tag{3.1}$$

where E_0 is the activation energy of the process. In this case, the activation energy is the energy of the 1S exciton plus or minus the phonon energy [137]. The 1S excitons can also decay at charged traps as a result of vacancies. This results in additional frequency components as indicated in Fig. 3.1. These processes are characterized by spectrally broad features. The phonon-assisted recombination line is made up of two separate MB distributions, one for the absorption of a phonon and one for the emission. However, because the two features are so close, and the spectrum is thermally broadened, 1S recombination appears instead as a single MB distribution.

Due to the small trap depth of the single and doubly charged oxygen vacancy, only fluorescence from the copper vacancy can be detected at room temperature [148]. This results in the typical PL spectrum as shown in Fig. 3.2. Fitting using an MB distribution accurately describes the high-energy slope, but does not capture the shape of the low-energy slope. This is in part due to the broadening of the

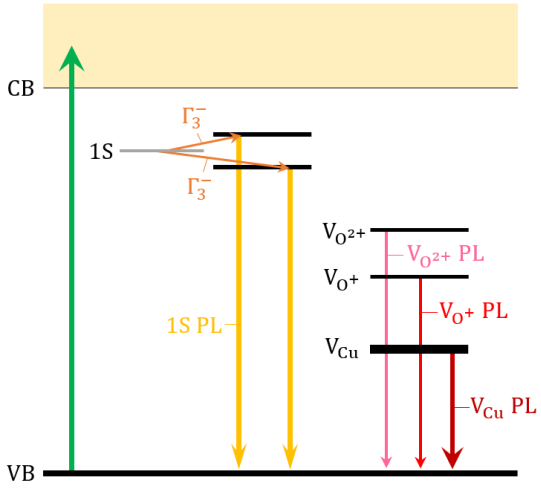

Figure 3.1: Overview of energy levels and resulting PL under above bandgap optical excitation. Only PL from the 1S recombination and copper vacancy can be detected at room temperature.

spectrum due to the spectral resolution of the spectrometer, which was 2 meV. The other factor is the low energy feature of the 1S feature which appears as a shoulder, as indicated by the green arrow in Fig. 3.2. This has been reported before [149; 150] and has been attributed to additional phonon-assisted processes. Their integrated intensity measured the size of the copper vacancy feature and 1S recombination feature.

To collect PL from the surface of the mounted polished samples were held vertically using Thorlabs KM100C mount. This was placed onto an XYZ translation stage built from three 1D translation stages. Excitation light provided by a 543 nm HeNe laser is then focused onto a point on the sample using a 0.70 NA lens (Edmund Optics LightPath 354330), with an effective focal length of 3.1 mm. Luminescence is collected using the same lens and separated from the excitation light using a dichroic mirror (Thorlabs DMSP567). Finally, this light is spectrally resolved using a spectrometer (is-instruments MSP1000). Spectra are collected using the accompanying Python package minispec to communicate with the spectrometer. Exposure times of 1000 ms were used throughout this section to collect spectra. This setup is illustrated in Fig. 3.3. This enables the characterization of the PL response of cuprous oxide across the surface of an entire sample. To reduce the impact of hot pixels on the detector it is important to take a "dark" spectrum where the laser is turned off alongside measurements of the spectrum. The dark spectrum is then subtracted from the data.

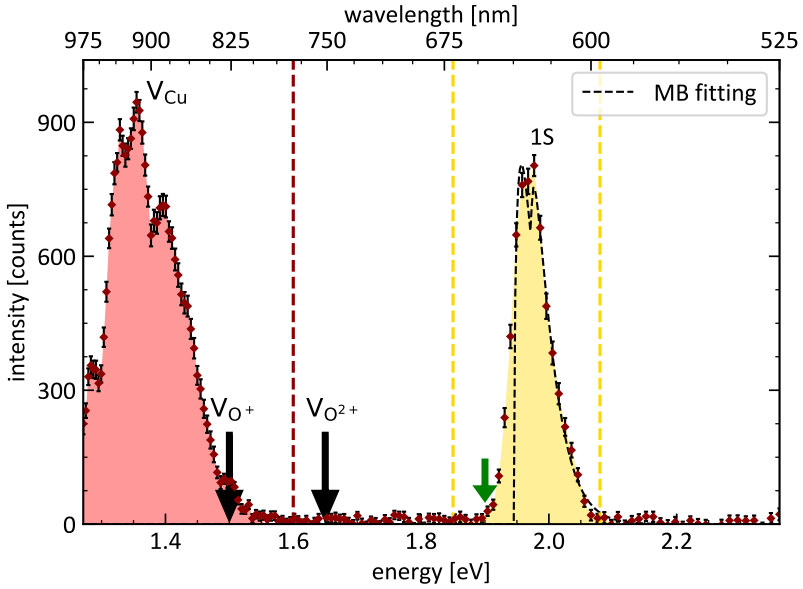

Figure 3.2: Typical PL spectrum of cuprous oxide under above bandgap excitation. Fitting the 1S lineshape with a Maxwell-Boltzmann distribution gives a temperature of 280 °K, in line with the expected 300 °K. Additional features on the copper vacancy feature arise from the dichroic mirror used to separate excitation and fluorescence. Copper vacancy intensity is integrated from the lowest resolvable energy to the dashed red line. 1S intensity is integrated between the two dashed yellow lines. The green arrow indicates the low energy shoulder on the 1S recombination feature.

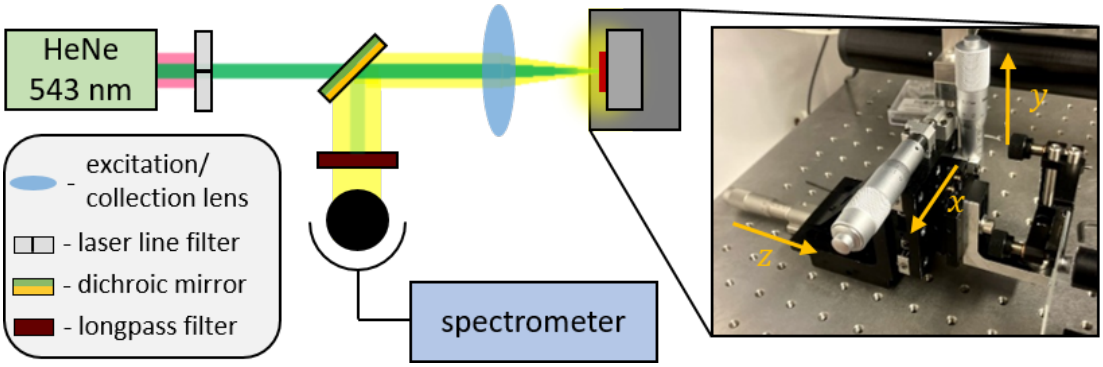

Figure 3.3: Overview of PL spectroscopy setup. Left: schematic of the experiment used to characterize samples. Light from the HeNe laser is initially filtered using a Thorlabs FL543.5-10 before being focused onto the surface of the sample. Luminescence is collected using the same lens as focusing, making the lens a critical component. Excitation light is separated from fluorescence using the dichroic mirror and stray excitation light is filtered off using a long pass filter (Thorlabs FEL0650). Right: the series of translation stages and kinematic mount used to achieve 5-axis control over the position of the sample, arrows indicate the orientation of x, y, and z directions.

To ensure that the results of subsequent experiments could be compared to one another the spot size on the sample must be the same throughout. This was achieved though by maximising the 1S recombination response on the spectrometer in each case. Such maximization was carried out by translating along the z-axis. Following this, the sample could be translated in the XY plane to collect data over the sample surface. Ideally, subsequent locations in the XY plane would be randomly selected to reduce systematic errors from accumulating throughout scanning the surface. However, as the sample is manually translated this was not the case. Instead, the sample was first translated along the x-axis from one edge to another. Following this the sample was translated an increment along the y-axis and the process was repeated back the other direction. This snake-like pattern results in a single pixel rastering across the sample surface.

3.1.2.1 Chromatic aberration

A drawback of using the aspheric lens in the system laid out above is the presence of chromatic aberration. As the sample is translated in the XY plane the distance between the lens and the sample can change. This can arise due to the sample not being perfectly flat with respect to the XY plane. This results in a different spot size at different locations on the sample. When combined with the chromatic aberration of the lens this leads to a substantial change in the PL spectrum. Not only does the amount of PL change due to the spot size but how efficiently it is collected changes as well. This effect is illustrated in fig 3.4.

This effect can be mitigated by adjusting the angle of the sample such that it lies within the XY plane. This is achieved by measuring the lens sample separation at different locations on the surface of the sample. This value cannot be easily measured directly. Instead, the chromatic aberration itself is used to provide a measure of this distance. By measuring the integrated intensity of the 1S and copper vacancy features as the translation stage is moved along the Z-axis one can observe surprisingly sharp features, as shown in Fig. 3.5. These features always occur at the same lens sample separation $\bar{z}$. Measuring this value at different points across the surface of the sample allows for a plane to be fitted to them, thus determining the angle the sample is at. By then adjusting the screws of the KM mount carefully the angle can be corrected. It is challenging to correct the angle in a single iteration. Often two or three iterations were required to provide

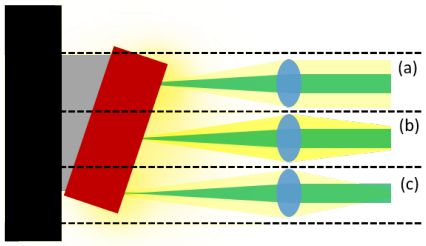

Figure 3.4: Impact of chromatic aberration as lens sample distance is varied. The sample in red is mounted at an angle due to the uneven distribution of nail varnish in grey. (a) green laser does not focus to a spot on the surface of the sample. But yellow fluorescence is collimated by the lens. (b) green spot forms on the sample, collection of yellow light is ineffective despite more PL generated than in (a) or (c). (c) both collection and excitation are ineffective.

an adequately small angle.

Another impact of chromatic aberration is that the collection efficiency of the 1S and copper vacancy light cannot be simultaneously maximized. To reduce this effect we can make use of the data collected in producing Fig. 3.5. For a particular lens sample separation, this contains information as to what fraction of the maximum signal at each wavelength is detected, providing a response curve. Thus, the chromatic aberration can be further corrected by dividing the spectrum by this response curve.

In cases where it is not possible to eliminate any angle from the sample this method of correcting for the chromatic aberration can also be used to reduce the impact of the remaining angle. Here, the response function is modified according to the variation in lens sample position described by the angle. It should be noted that this issue can also be resolved through the use of a microscope objective.

3.1.3 Transmission Spectroscopy

The highest observable nP state is determined through the use of broad cryogenic band transmission spectroscopy (conducted at a stage temperature of 4 °K. Further details on the experimental setup can be found in Chapter 4. Here, the

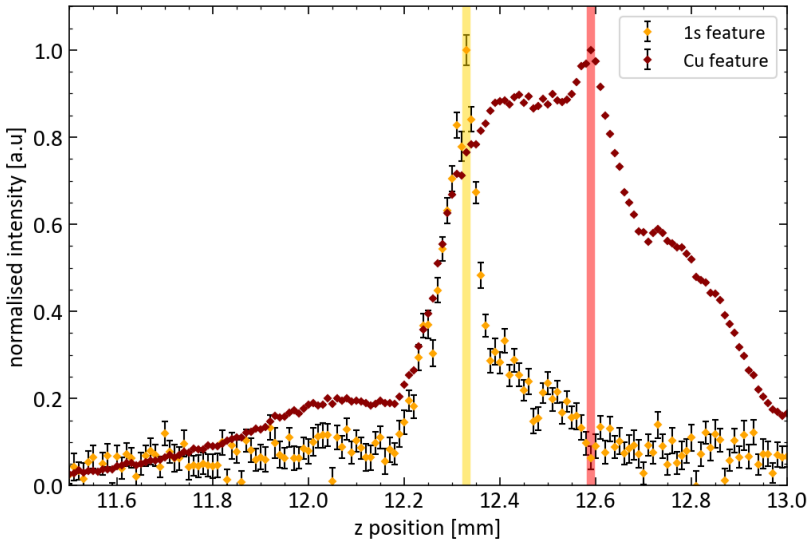

Figure 3.5: The yellow and red vertical lines indicate the maximum response of the 1s and Cu features as a function of z. Multiple features present for both the 1S and Cu features arising from the competing effects of collection and excitation efficiency. The sharp feature in the Copper vacancy was used to determine the lens-sample separation.

excitonic states are probed by spectrally resolving the transmitted light through a sample of cuprous oxide. The transmitted light is resolved using a monochromator (Horiba iHR550) equipped with 1800 g/mm and 2400 g/mm diffraction gratings giving resolutions of 110 µeV and 80 µeV respectively. The slit was imaged using a camera (Basler ac2040-120um) to resolve the spectrum. Further details on the setup can be found in [55]. The imaged spectrum would appear as a series of vertical bright and dark regions corresponding to the transmission of excitonic states. The intensity incident on each pixel would return a 12-bit integer at each location. By vertically summing over each set of pixels a spectrum vs pixel number can be obtained. This is repeated as the position of the monochromator is changed to produce a full spectrum. The different sections of the scan are stitched together by comparing the wavelength extracted.

Additionally, a similar setup was used to obtain some of the data in this thesis which was instead based at Cardiff University. This system utilized operated at a higher level of spectral resolution 35 µeV. Again, further details on this setup can be found in [55]. As before, a similar procedure was carried out to obtain spectra.

sample name	description
AE	natural sample
AM	natural sample
AF	synthetic sample
AF2	annealed synthetic sample

Table 3.1: Samples are characterized throughout this section.

3.2 Characterising Samples

Here we will explore the characterization of both natural and synthetic samples through the use of PL and transmission spectroscopy, these are listed in table 3.1. We will then examine the effects of thermal annealing on the quality of synthetic samples.

3.2.1 Natural Sample AE

To establish a baseline for high-quality samples we start by investigating naturally occurring materials. In particular, we study two natural gemstones: AE and AM. The sample AM is used throughout this thesis as the highest quality natural sample we have access to. We start with the natural sample of AE.

PL spectroscopy was carried out over the surface of the sample, with spectra being obtained along a square grid of locations separated by 0.1 mm. The results of this are shown in Fig. 3.6(a), with the typical PL spectrum shown in Fig. 3.6(b). The variation of the 1S response is well described by a Gaussian distribution centered on 220 ± 5 a.u., with a width of 190 ± 10 a.u. The width is of the order of the mean value. This leads to some regions having nearly no response, while others are nearly twice as bright as the average response. Physically this variation can come from many sources. The quality of the surface can impact the amount of area probed by the laser and the corresponding collection efficiency. Variation in local strain can lead to excitons becoming preferentially trapped in some regions of the sample, resulting in an increase in PL from these regions. Finally, defects can also impact the PL collected from a specific region [121].

Of key importance is that there is no substantial PL from the copper vacancy region. This is indicated by the distribution centered on 2 ± 1 a.u. with a width of 23 ± 2 a.u. This variation originates from the dark subtraction used to remove

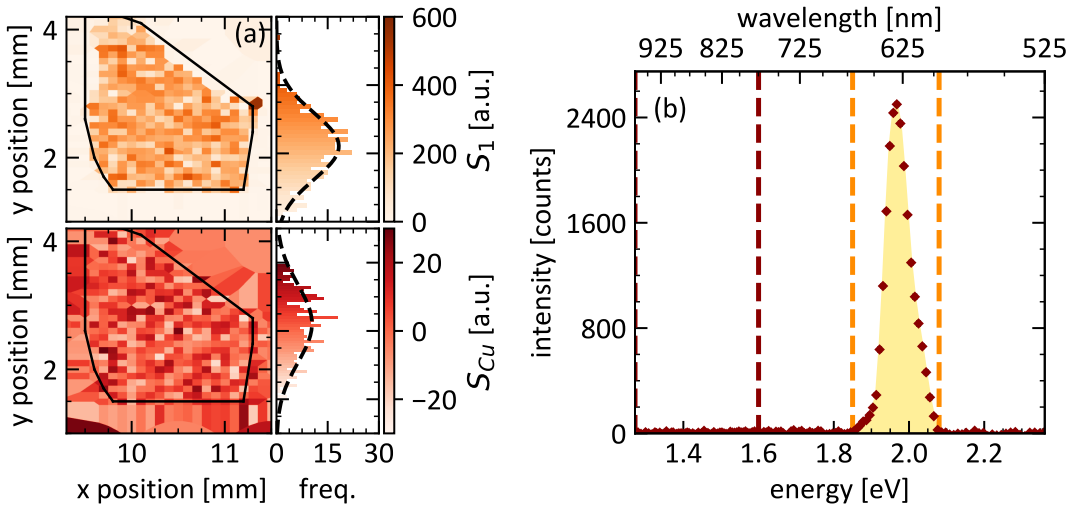

Figure 3.6: Characterisation of the natural sample AE. (a) integrated intensity of the 1S and copper vacancy recombination across the XY plane. The black line indicates the outline of the sample. Dashed lines on the histogram correspond to Gaussian fits. (b) typical PL spectrum obtained from the sample. Dashed lines show regions over which integrated intensities are acquired.

hot pixels. This is supported by the variation in the copper vacancy signal being similar both off and on the sample.

To then directly measure the quality of the sample, transmission spectroscopy was also carried out. The results of which are shown in fig 3.7. This enabled clear observation of up to 12P, with a small feature potentially corresponding to 13P. This indicates that this natural sample is of a higher quality than any synthetic sample.

3.2.2 Natural Sample AM

As with AE, PL was collected from across the surface of the sample. The same step size of 0.1 mm was used, but the sample is notably smaller. The results for this are shown in Fig. 3.8.

The response from the 1S PL is nearly twice as strong for AM as for AE, with the distribution now centred on 344 ± 14 a.u. with a width of 180 ± 30 a.u. Meanwhile, the response from the copper region is much the same, centred on 0 ± 1 a.u. with a width of 14 ± 2 a.u. This combined with the ability to resolve up to 14P, as shown in Fig. 3.9, suggests that AM is a higher quality sample than

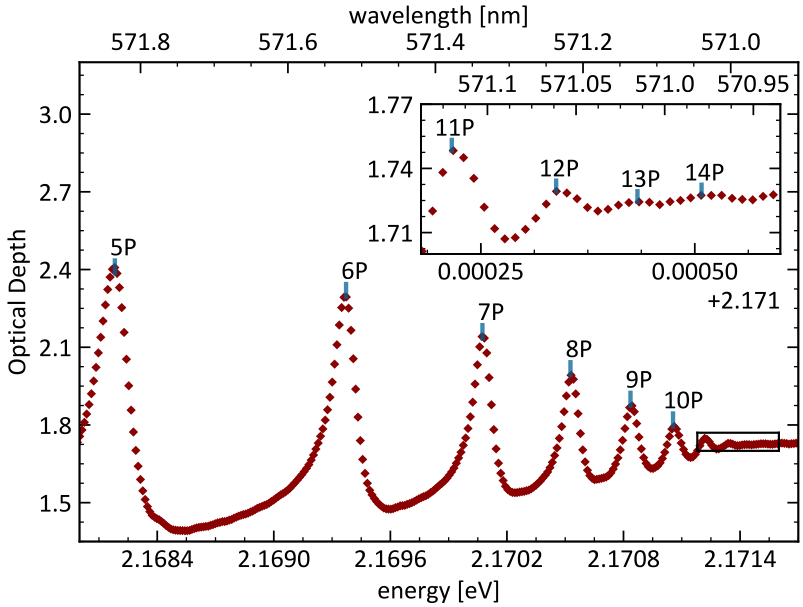

Figure 3.7: Transmission spectroscopy of the natural sample AE, collected by Liam Gallagher in 2018, reproduced with permission. The spectrum was obtained using the spectrometer at Durham. Excitonic peaks up to 12P are clearly resolvable with no significant additional features.

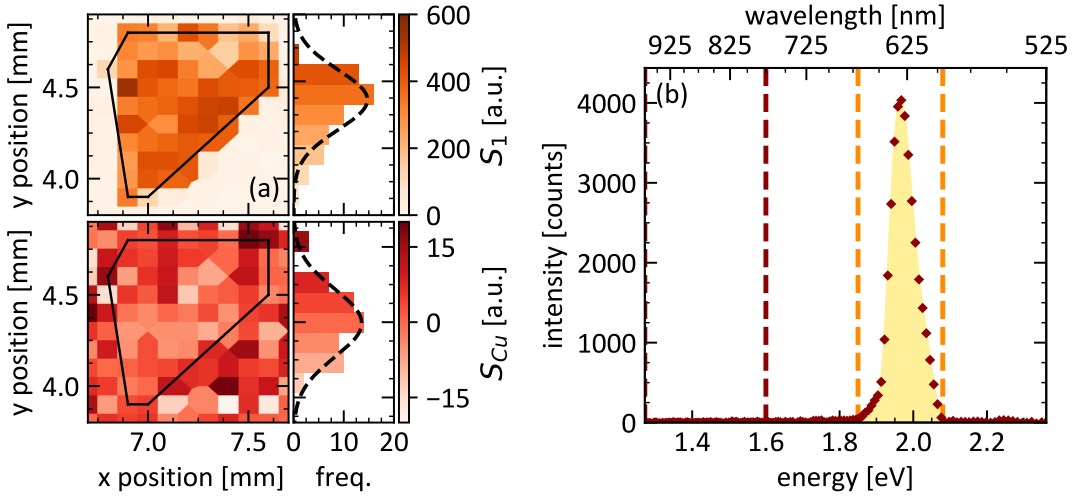

Figure 3.8: Characterization of the natural sample AM. (a) the integrated intensity of the 1S and copper vacancy recombination across the XY plane. The black line indicates the outline of the sample. Dashed lines on the histogram correspond to Gaussian fits. (b) a typical PL spectrum obtained from the sample.

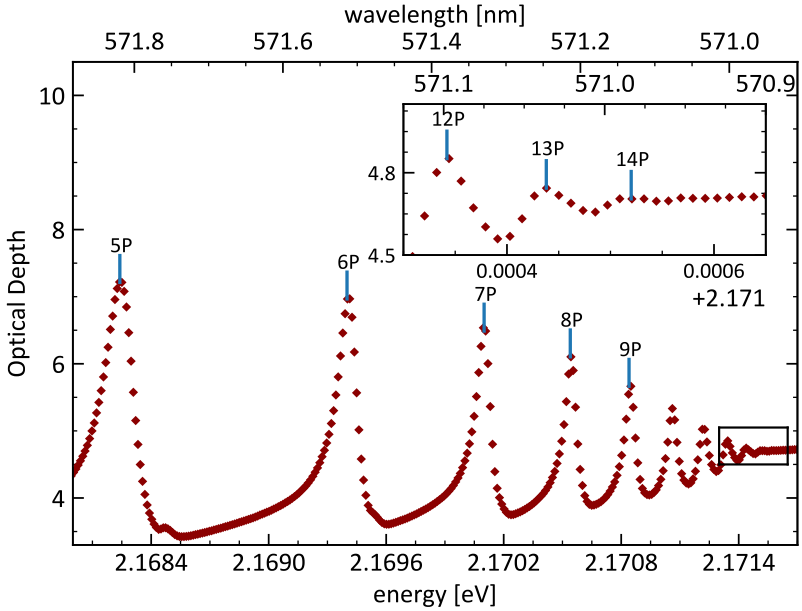

Figure 3.9: Transmission spectrum of the natural sample AM, collected by Liam Gallagher in 2018, reproduced with permission. The spectrum was obtained using the spectrometer at Cardiff. Up to 14P can be resolved. Higher P states may be supported by this system, but it is now limited by the resolution of the monochromator.

AE. Additionally, it suggests that the 1S PL signal can be used as an indicator of quality. Physically this can be understood by recalling the role of defects in PL. They provide traps enabling alternative pathways for decay. So, a lower defect density will enable a higher proportion of excitons to decay via phonon-assisted recombination, leading to a higher 1S PL signal. It should also be noted that AM also approximately 3 times thicker than AE leading to a larger optical depth in transmission.

3.2.3 Synthetic Sample AF

Applying the same procedure to investigate the PL response of a synthetic sample yields the results shown in Fig. 3.10. As with natural samples, a clear 1S recombination feature can be seen, with the distribution in sizes being described by a Gaussian centred on 56 ± 2 a.u. with a width of 57 ± 4 a.u. Again, as these values are comparable to one another there are regions with virtually no PL in these regions and some which are twice as bright as the average value. This signal is approximately 3 times smaller than that seen in AE.

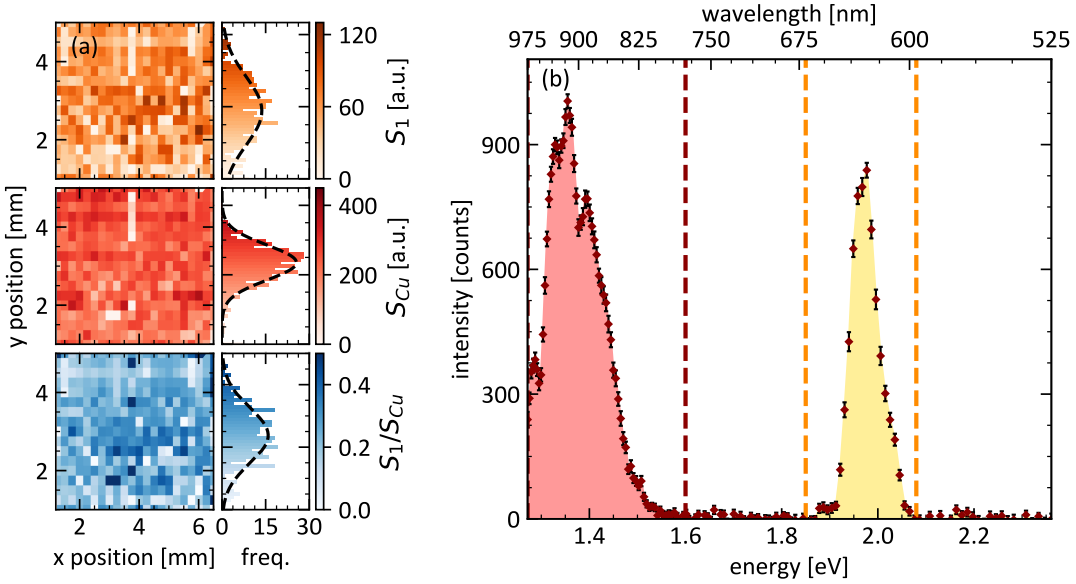

Figure 3.10: Characterization of synthetic samples AF. (a) all data points taken on the surface of the sample. Dashed lines on histograms correspond to Gaussian fits. The ratio of 1S to copper vacancy PL is also well described by a Gaussian, suggesting that the two features scale in a similar way across the surface of the sample. (b) typical PL spectrum from AF. There is a significant response from both 1S and copper vacancy PL.

Unlike the natural samples, a substantial response from the copper vacancy can also be detected. The copper vacancy signal is centred on 235 ± 3 a.u. with a width of 100 ± 5 a.u., meaning the width is a smaller fraction of its mean value. Thus, the copper vacancy varies by up to a third across the surface of the sample. The ratio of these two features also varies across the sample, with the relative size of the 1S signal being the largest towards the centre of the sample. This ratio too is described by a Gaussian distribution centered on 0.24 ± 0.01 a.u. with a width of 0.18 ± 0.01 a.u. Here, the width is slightly smaller than the mean value, which reflects the relative distribution of the 1S and copper vacancy signals.

The variation in the 1S signal is again likely due to local strain, variations in sample quality, and variations in surface quality. This also accounts for the variation in the copper vacancy. The reduced spread in response of the copper vacancy signal implies a more constant density of copper vacancies across the sample. The reason for this is to do with the mechanism for generating PL. At each point being probed by the 543 nm laser, a similar amount of electron-hole plasma will be generated. The detected PL will then depend on the number

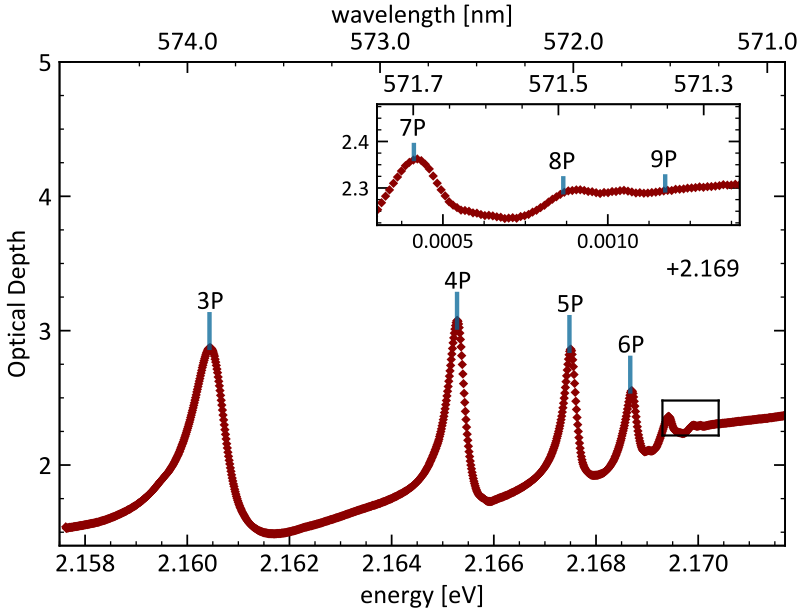

Figure 3.11: Transmission spectrum of AF. The spectrum was obtained using the spectrometer at Cardiff. Only up to 8P is resolvable in this stone. A small additional feature appears on the high energy side of 8P, this may be an even parity state.

of recombinations that occur within the collection cone of the lens. Unlike 1S recombination, which can occur at a different location than where the plasma is generated, the copper vacancy signal will be detected where there are copper vacancies. Physically this is because the copper vacancies trap excitons. Thus, a uniform distribution of copper vacancies will lead to a uniform distribution of copper vacancy PL.

To then measure the quality of the stone we once again probe the excitonic structure using transmission spectroscopy, as indicated in Fig. 3.11. This indicates a lower-quality sample with 8P being the highest resolvable principal quantum number.

The key difference between the PL of the natural and synthetic stones is the presence of copper vacancies and a smaller 1S signal. This supports the hypothesis that the copper vacancies are leading to a reduced sample quality. To address this the synthetic samples can be annealed to remove copper vacancies.

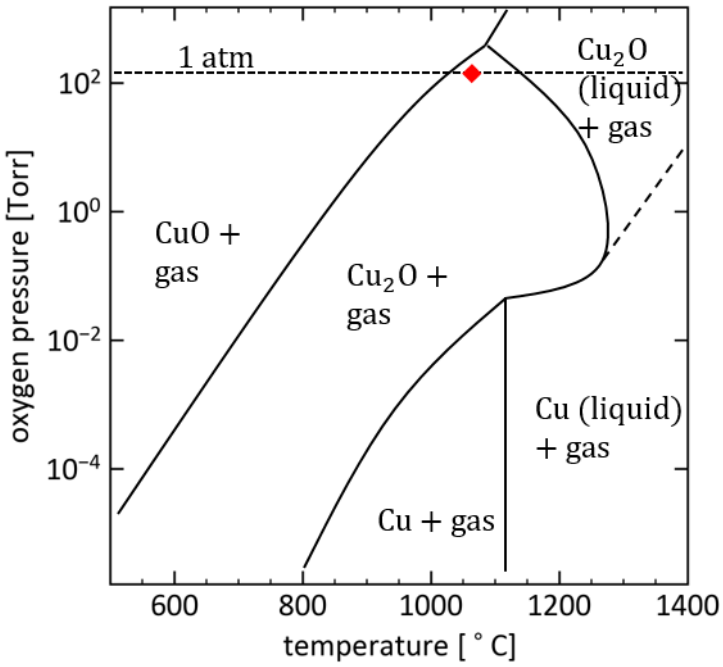

Figure 3.12: Phase diagram for a copper-oxygen system for oxygen pressure vs temperature (modified from Schmidt-Whiteley *et. al.* [151]). The red mark is the temperature/pressure combination used in this annealing process.

3.3 Annealing Synthetic Samples

For the annealing process to be effective the temperature and pressure must be carefully controlled. Here, the method laid out in [136] was used. At atmospheric pressure, there is only a small range of temperature which will result in the cuprous oxide phase of a copper oxygen system, instead of cupric oxide, as indicated in Fig. 3.12. Furthermore, great care must be taken to select an appropriate crucible to support the sample to be annealed. At high temperatures, cuprous oxide will react with many common crucible materials [151]. For the annealing process described here, a CaF_2 crucible was used. Before annealing the sample was placed in acetone and then methanol for 1 hour each to remove any contaminants. Following this it was placed on top of a CaF_2 window and heated to 1025 °C at a rate of 300 °C/hr. It was held at this temperature for 50 hrs before cooling at a rate of 100 °C/hr to room temperature.

Following on from this the samples were coated in a layer of black material thought to be cupric oxide. When polished away this revealed the characteristic red luster of cuprous oxide. As before this new sample was characterized using PL

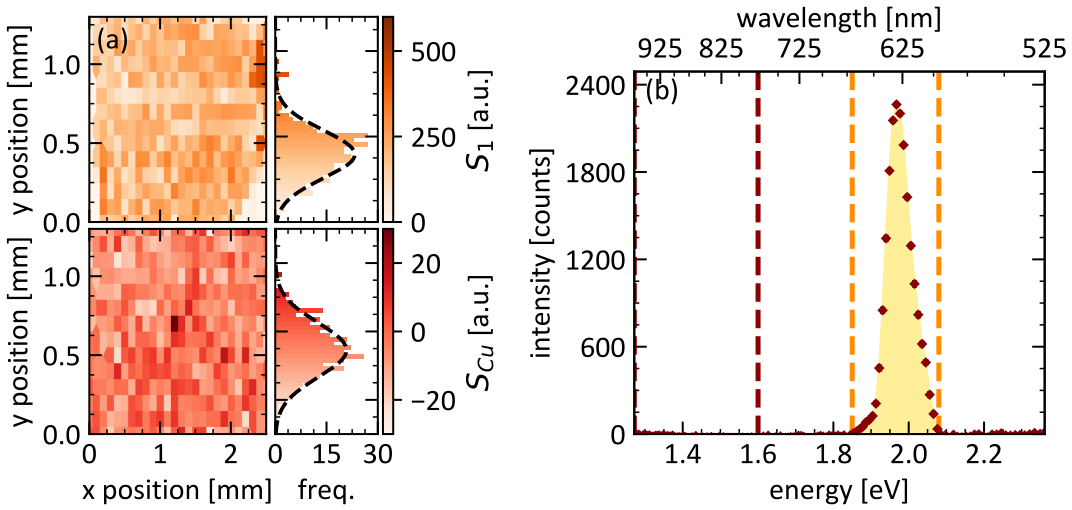

Figure 3.13: Characterization of a section of the synthetic sample AF after annealing. (a) suppression of the copper vacancy signal across the entire sample alongside enhancement of the 1S PL signal. (b) a typical PL spectrum from this sample. There is no longer a substantial copper vacancy signal.

spectroscopy. The results of this are shown in Fig. 3.13.

The annealing process shows a marked improvement in the PL spectrum across the entire sample. The copper vacancy feature has been suppressed to the extent that it appears just as it did in the natural samples. If any significant PL remains at this wavelength it is below the detection limit of this system. Similarly, the 1s recombination feature has been enhanced to the point that it is comparable to that of a natural sample. This improvement would suggest that the copper vacancies have been significantly suppressed as a result of the annealing process. The noise floor of the system implies that the largest integrated intensity of any remaining copper vacancy would be of the order of 0.1 a.u. or less. As a result, the copper vacancy density is at least 1000 times lower.

However, when we measure the sample quality using transmission spectroscopy only 6P can be resolved, as indicated in Fig. 3.14. This stands in opposition to the hypothesis that the highest observable principal quantum number is limited by the copper vacancies. Thus far, there has been no PL spectroscopy conducted at cryogenic temperatures where other vacancies could be seen. So, to shed light on what is now limiting this new spectrum we also collect that on this annealed crystal.

The experimental setup for collecting PL at low temperatures is much the same

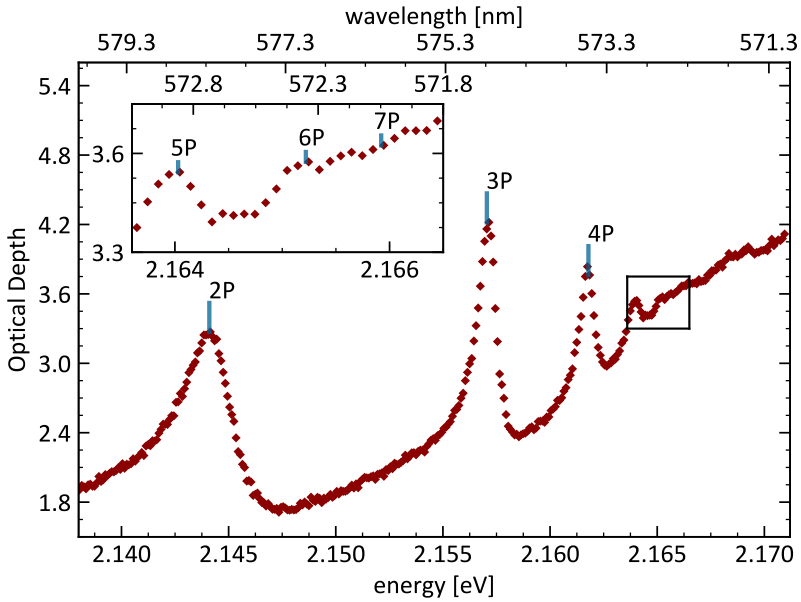

Figure 3.14: Cryogenic transmission spectrum of annealed synthetic AF. The spectrum was obtained using the spectrometer at Durham. Only up to 5P is resolvable with a small feature in the region of 6P.

as that described in Fig. 3.3. A notable change is that PL is generated using the 1142 nm laser described in the following chapter. This still creates the necessary electron-hole plasma. This results in the spectrum shown in Fig. 3.15. Unlike previous spectra, the 1S recombination signal is now much narrower, as expected since the thermal distribution of phonons is far narrower. Now, we can see an additional feature in the spectra centred around 1.65 eV, corresponding to doubly charged oxygen vacancies. It is the addition of this vacancy that we attributed to the reduced quality of the annealed samples. This was likely introduced into the sample during the annealing process.

It remains unclear if it is possible to anneal samples in such a way that both oxygen and copper vacancies can be removed. It may be that the cooling process is where vacancies are introduced. The phase diagram shown in Fig. 3.12 requires that the phase passes through the CuO region as the sample is cooled to room temperature under atmospheric conditions. However, if a lower oxygen partial pressure were used it may be possible to avoid this phase entirely.

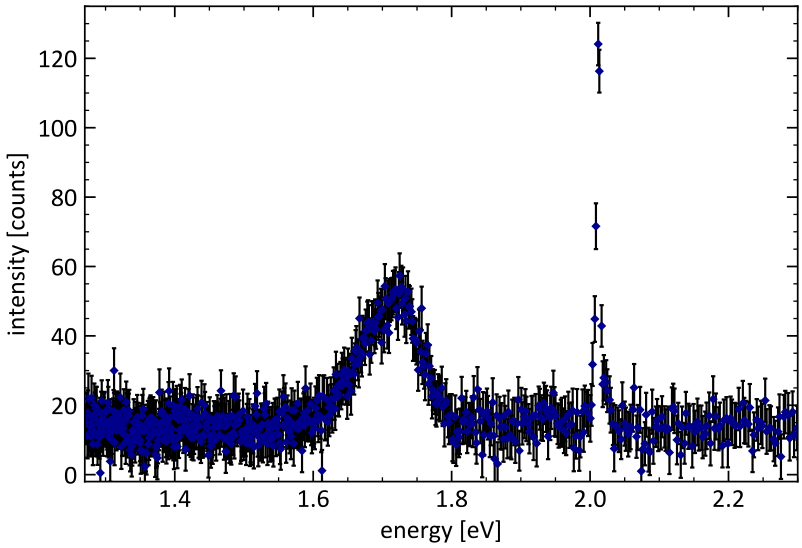

Figure 3.15: Cryogenic PL spectrum of annealed AF. The sharp feature at 2 eV is the recombination of the 1S exciton and the broad feature at 1.7 eV corresponds to the doubly charged oxygen vacancy.

3.4 Conclusions

Natural and synthetic samples of cuprous oxide have been compared through both photoluminescence and transmission spectroscopy. This indicated that the presence of copper vacancies in synthetic samples was limiting the highest principal quantum number that synthetic samples can support. Thus, the lack of a copper vacancy was used as a measure of sample quality. Furthermore, photoluminescence spectroscopy revealed a much stronger 1S recombination signal in natural samples compared to synthetic samples. This suggests a larger proportion of the electron-hole plasma recombines via phonon-assisted recombination instead of at a defect site. In turn, it provides an additional measure of the sample quality.

The synthetic sample was also annealed under atmospheric conditions to remove copper vacancies from the crystal lattice. While this was successful, resulting in a complete suppression of the copper vacancy, it did not improve the quality of the sample. Instead, the annealing process reduced the highest observable principal quantum number. This was attributed to the introduction of a doubly charged oxygen vacancy during the annealing process. It may be possible that annealing under a reduced pressure or an alternative annealing procedure will lead to the production of higher-quality synthetic samples. However, exploring

the vast sample space associated with annealing remains a significant logistical challenge.

Chapter 4

Transmission Spectroscopy

Cuprous oxide positions itself as a potential gateway to utilizing atomic physics in the solid state. In doing so, it offers access to the exaggerated properties of Rydberg states in the cryogenic environment, without the inhibiting laser systems required for cold Rydberg atoms [152; 153]. Thus paving the way for novel quantum information technologies; such as single photon sources [54], quantum simulation, optics and computation [154; 155]. Of particular note is the potential use of cuprous oxide as a microwave-to-optical conversion tool, which this group has previously studied in [74]. This concept will be explored more in the following chapter. Owing to the scaling laws of Rydberg excitons [111] it is crucial that high principal quantum number states can be accessed to make use of this wealth of physics. As the previous chapter explored, there is still a large amount of work required to develop high-quality synthetic samples. Limiting research into the excitonic properties of cuprous oxide to high-quality natural samples.

Throughout the remainder of this thesis spectroscopy will be carried out on high-quality natural samples of cuprous oxide. Doing so enables access to the high-lying excitonic states. The highest principal quantum number observed in this thesis so far is 14P, a far cry from the observation of 30P made by Versteegh et al. in 2021 [59]. This suggests that either the quality of the sample is limiting our observations or there is a limitation to this experimental setup. Additionally, previous work carried out in Durham using second harmonic generation (SHG) spectroscopy on the same sample was only able to resolve up to 12S [84]. This value is again significantly below the current state-of-the-art limit to the principal quantum number.

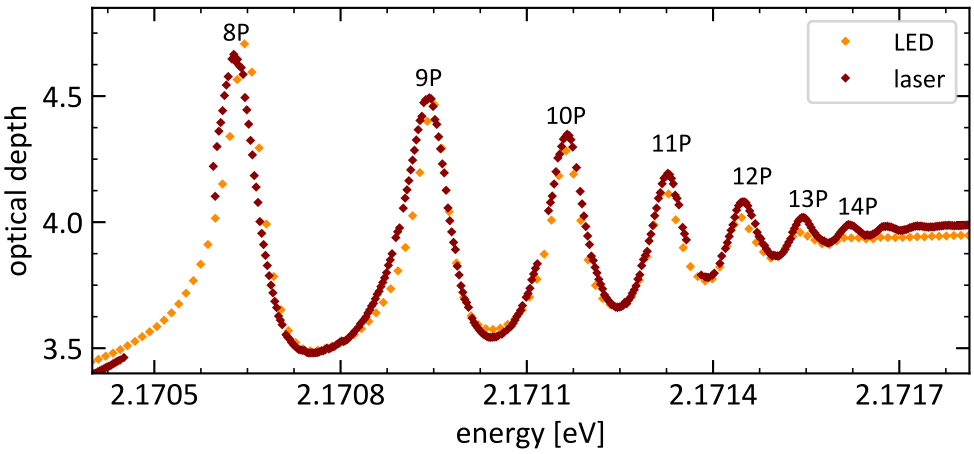

Figure 4.1: Comparison between transmission spectroscopy carried out with a broadband LED and a narrowband tunable laser. The key difference is the capability of laser spectroscopy to resolve higher n excitons than LED spectroscopy.

Taken together this motivates a study of the factors limiting the resolution of high principal quantum number states by our system. Broadly speaking these factors can be divided into two categories: experimental limitations and physical limitations. Experimental limitations describe the noise floor, spectral resolution, and stability of the system. These would prevent an excitonic state from being detected, even if it were present in the material. Physical limitations on the other hand, such as sample quality or temperature, reduce the population of a particular state to prevent observation.

The broadband transmission spectroscopy experiments carried out so far have not been limited by the experimental stability or noise floor. Instead, the limiting factor has been the spectral resolution, originating from the diffraction grating used. Of the physical limitations, only the quality of the sample has thus far been explored. This was carried out in the previous chapter. Sample temperature on the other hand has so far been only an incidental point. Temperature not only determines the population of thermal phonons in cuprous oxide but it also provides an alternate ionisation pathway [156; 157]. This occurs when the characteristic thermal energy $k_{\mathrm{B}}T$ becomes comparable to the exciton binding energy. As a result, temperature can play a key role in observing such states. This role will be explored in more detail in the following section. The results of the previous chapter do not indicate which of these factors, or a combination thereof, are limiting this experiment.

Thus to determine what factors limit the detection of high principal quantum number excitonic states transmission spectroscopy will be carried out using a narrow-band tuneable laser. This offers improved spectral resolution over broad-band transmission spectroscopy, as indicated in Fig. 4.1. In addition to this, the temperature of the sample can be changed to study its impact on resolving high-lying states. Taken together this enables a determination of the key limit to our system, which is concluded to be the temperature and not the quality of the sample.

4.1 Experimental Setup

This section will lay out the experimental setup used to carry out narrow-band laser spectroscopy. Transmission through a cryogenic sample of cuprous oxide is measured using a 572 nm tunable laser. The schematic for this is shown in Fig. 4.2. Broadly speaking the setup is split into three components: laser control, signal detection, and control of sample position/temperature. These will be discussed separately in the following sections. The vast majority of the equipment described in the following section is controlled using a single computer through the LabView software. Communication between various components and the computer is achieved using a pair of DAQ devices (National Instruments USB-6008), further details on computer control of this experiment can be found in [55].

4.1.1 Sample Control

Both sample temperature and position are controlled through the use of a closed-loop helium cryostation (Montana instruments C2 Cryostation) which cools samples of cuprous oxide to cryogenic temperatures. Sample temperature is measured using a thermister probe measuring the base temperature inside the cryostation. Following the sample preparation steps carried out in the previous chapter ∼100 µm thick high-quality natural samples are placed into copper mounts. As before the samples are glued onto transparent CaF_2 windows using nail varnish. To minimise strain during cooling only a corner is stuck down. A spacer is then placed on top of the window such that an additional CaF_2 window can be placed on top of this without touching the sample. A spacer between the windows is

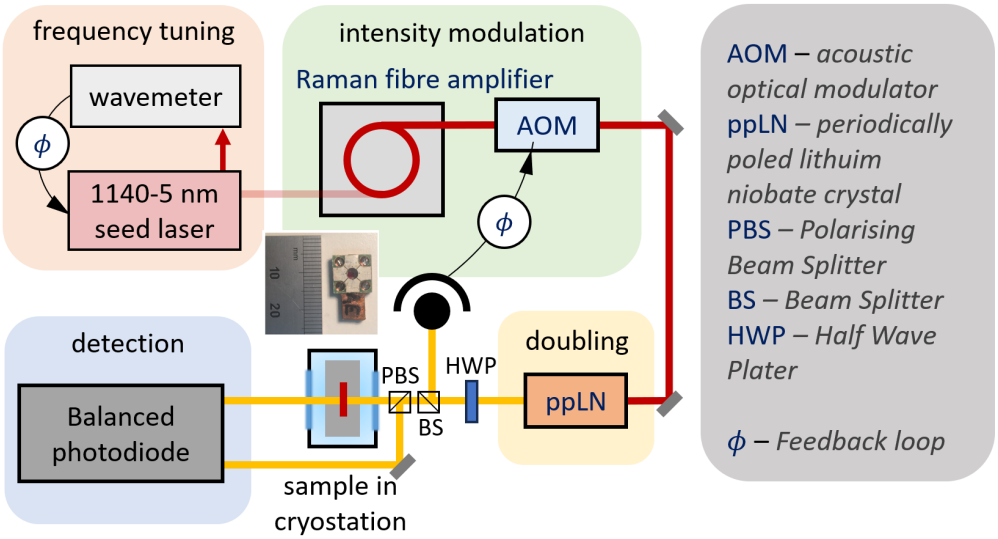

Figure 4.2: Schematic of the experimental setup used to resolve excitons. Upon generation, the visible laser is split using a 90:10 BS cube. The larger signal is directed through the sample. The amount of light incident onto the reference port of the BPD is controlled using a HWP and a PBS cube. Pictured is one of the copper sample mounts used throughout these experiments.

used to ensure this. This entire setup is glued in place in the clear aperture of the copper mount. This in turn is mounted onto a copper block atop the piezo stage. The piezo stage offers 5 mm of travel and a stability of 0.5 µm. This enabled precise control over the position of the sample within the cryostation. Further details on this setup can be found in [55]. A major challenge during this step is ensuring that there is sufficient thermal contact between the sample and the cold head. Failing to do so can lead to the sample being warmer than expected. The limiting factor here is nearly always the contact between the CaF_2 window and the samples. This is compounded by the fragile nature of the thin samples which are prone to breaking during the mounting process. The temperature of the sample stage was set to 4 °K.

4.1.2 Laser System

The laser system shown in Fig. 4.2 is based on an external cavity diode laser (TimeBase ECQDL-1146) used as a seed laser. This provides up to 200 mW of IR power. The seed laser can be tuned between 1140 and 1145 nm. The tuning element is a diffraction grating in the Littrow configuration [158]. Coarse tuning

of the laser is achieved by manually adjusting the grating angle via a screw. Fine-tuning is done by applying a voltage to a piezo stack to tilt the diffraction grating. Utilising a feed-forward method [159] to simultaneously vary the piezo voltage and diode current a mode-hop free tuning range of up to 20 GHz can be achieved. Building up a spectrum requires repeated re-tuning of the laser between subsequent scans, further details on this are discussed in the following section. The frequency was monitored on a self-calibrating wavemeter (Bristol Instruments 671A). This measures the frequency at a rate of 4 Hz to an accuracy of ±60 MHz.

The seed laser is then amplified using a Raman fiber amplifier (MPB Communications Inc. RFL-P-5-1143-SF-NS) generating up to 5 W of power. This provides more than enough IR power for our purposes. This IR light is then frequency doubled in a periodically poled lithium niobate crystal (Covesion MSHG1220-1.0-xx). The amount of IR power sent into the ppLN crystal is controlled using an AOM. Here, the first-order deflection couples light down a fiber to the ppLN whereas the rest of the light is safely dumped. Further details on this setup can be found in [55]. The resulting visible light intensity is monitored using a pick-off in front of the cryostation. This provides a feedback loop to stabilize the power.

The stabilization loop itself operates by reading a voltage from a photodiode (PD) which implies a visible intensity. The conversion between voltage and intensity is calibrated using a power meter (Thorlabs S120VC). The voltage applied to the AOM is then changed by an amount proportional to the difference between the current and target intensities. Thus forming a proportional feedback loop. However, the DAQ has a digital resolution of 2 mV, placing a floor on the smallest change in voltages. Some care must be exercised when selecting the gain of this feedback loop to ensure convergence to the target power.

4.1.2.1 Generating Yellow Light

The key challenge in achieving efficient frequency doubling is fulfilling the phase-matching condition. This arises due to the different refractive indices of the two different wavelengths involved in the process. A ppLN crystal can give a quasi-phase matching condition, so long as the spacing between the poles is correct for a given wavelength. In this work, a Covesion MSHG1220-1.0-xx ppLN crystal is used which offers 5 different polling channels. The poling length can be further

modified by changing the temperature of the crystal. Throughout this work, the 7.78 µm polling channel is used.

Another major factor affecting the doubling efficiency is the beam waist of the IR laser within the crystal. This is a result of the doubled light intensity depending on the square of the IR intensity. The optimal beam waist is determined by ensuring the ratio of the optical length of the crystal ηL and the Rayleigh range, z_R, are related by $\eta L/(2z_R) = 2.84$ [61] where η is the refractive index and L is the length of the crystal. Here, the ppLN is 20 mm long with a refractive index of 2.23 at 1140 nm [160] resulting in an optimal beam waist of 35 µm. A 40 mm focal length lens was modelled in Zemax and gave a waist of 34 µm with an input beam diameter of 2.5 mm.

To obtain efficient doubling at 1142 nm the ppLN needs to be heated to approximately 45 °C. This was achieved using a Peltier heater controlled by a temperature controller (MPT2500 2.5 A). The temperature of the ppLN crystal is controlled by applying a voltage to the Peltier heater via computer control. This in turn varies the temperature of the crystal. The voltage required to achieve optimal doubling was determined first by fixing the wavelength of the laser. The temperature of the ppLN is then varied over a range and the resulting intensity was recorded using a power meter (Thorlabs S120VC). This results in an Airy function pattern which can be fitted to locate the voltage that corresponds to the optimal doubling. This procedure is then carried out at a wide range of wavelengths and subsequently fit using a 3^{rd}-order polynomial. The results of this are indicated in Fig. 4.3. Using this calibration allows for the generation of up to 50 mW of yellow light using 5 W of input IR light. This is more than enough for this thesis.

4.1.3 Detection

The transmission through the sample was measured using a Nirvanna auto-balanced optical receiver (2007 model). This offers the advantage of cancelling out fluctuations in laser intensity. The model of balanced photodiode (BPD) used offers a differential and logarithmic output to monitor the transmitted intensity. Owing to the relatively small change in absorption across the excitonic spectrum the logout function was used. The output voltage, $V_{\log}$ is given by:

$$V_{\log} = -\ln\left(\frac{P_{\text{ref}}}{P_{\text{sig}}} - 1\right), \tag{4.1}$$

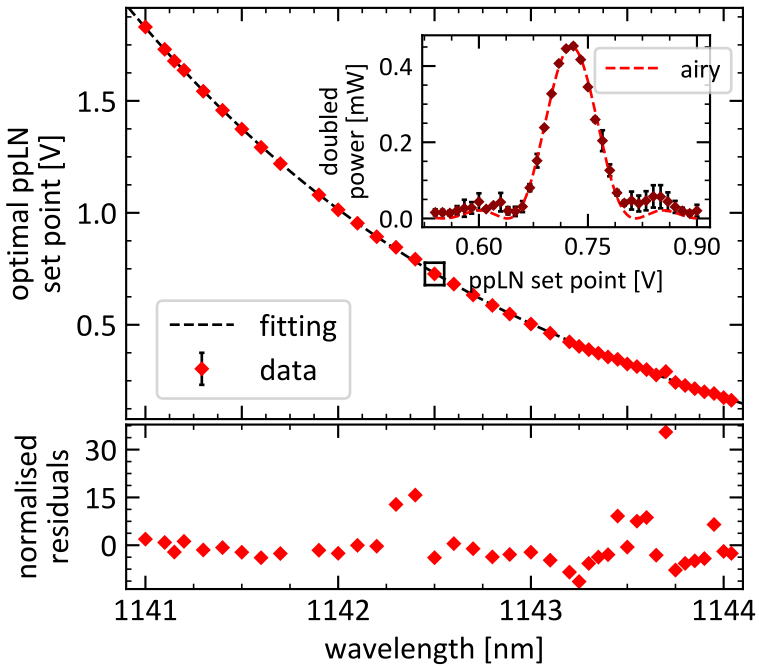

Figure 4.3: Calibration of the ppLN used throughout this chapter. The optimal set point is described by a cubic polynomial in wavelength as indicated by the dashed line. This is of the form: $V = a\lambda^3 + b\lambda^2 + c\lambda + d$, for wavelength λ. The numerical values of the parameters used are $a = -1.96 \cdot 10^{-2}$, $b = 6.75 \cdot 10^{1}$, $c = -7.73 \cdot 10^{4}$ and $d = 2.95 \cdot 10^{7}$. The archetypal dependence of doubled power vs set point is shown in the inset, which corresponds to the data point in the black box.

where P_{ref} is the power incident on the reference port and P_{sig} is the power incident on the signal port. To convert this to optical depth it is required to know the amount of power incident onto the sample and P_{ref}. The power incident onto the sample was 10 µW and the P_{ref} used was 0.42 µW. The optical depth is then given by:

$$OD = -\ln\left(\frac{P_{\text{ref}}}{(e^{V_{\log}} + 1)P_{\text{inc}}}\right), \tag{4.2}$$

where P_{inc} is the intensity incident onto the surface of the sample. The detector is only able to return a range of voltages from -10 V to +10 V, so care must be taken when selecting P_{ref}. Here, this intensity was controlled using a PBS and a HWP in tandem. For these transmission experiments, the laser light was collimated and fixed at a diameter of 250 µm using an iris. This configuration allowed for a relatively high input power to be maintained without risking damage to the sample. The width here is set by the physical size of the sample.

The output of the detector was recorded using an oscilloscope (R&S RTO1024) to take advantage of the higher voltage resolution offered over the DAQ. The oscilloscope was able to record with a precision down to 0.2 mV compared to the 2 mV limit of the 12-bit DAQ. This higher precision is achieved owing to the dynamic range of the oscilloscope, despite its lower 8-bit depth.

This recorded the time-resolved output of the BDP. However, this introduced an experimental challenge as the scope was unable to directly communicate with the lab computer. As such, it was not possible to simultaneously record the laser wavelength and the response from the scope during a laser scan. To overcome this an additional syncing signal was used. This signal would be sent to the scope when the laser frequency changed, such that it was clear which region of the trace corresponded to which part of the laser scan. Data was saved onto a USB and then manually placed onto the lab computer.

4.1.4 Obtaining a Spectrum

To obtain a transmission spectrum the laser must be scanned over the entire excitonic spectrum. This is carried out using the coarse and fine-tuning methods described in the previous section. Here, the laser is course-tuned to a desired frequency before scanning the laser over a short range using the piezo. This scans across approximately 20 GHz. The course tuning is then used again to navigate to a new frequency. The fine-tuning steps will be referred to as laser scans. It is crucial to ensure that the frequency range of adjacent scans overlaps to avoid gaps in the spectrum. Each scan is saved separately and then compiled together in post-processing to produce a full spectrum. A typical laser scan takes up to 200 s, depending on the desired resolution. This is set by the step size in the piezo voltage during the feed forwards scan. In the vast majority of cases, this was set between 1 and 2 V in this work. Approximately 20 scans are required to obtain a full spectrum. With additional re-tuning steps between subsequent scans, it typically takes several hours to obtain a spectrum. At each laser detuning data was collected for 1000 ms.

4.2 Resolving Rydberg Excitons

Using the setup described in the previous section it is possible to resolve excitonic states. Carrying this out at 5 °K results in the spectrum shown in Fig. 4.4. Here, up to 16P is resolvable. As indicated in Fig. 4.1, this narrowband approach can resolve much further into the spectrum than its broadband counterpart. Quantitative information on the individual states can be extracted by separately fitting the spectrum with a series of asymmetric Lorentzian line shapes plus a background term:

$$\alpha_{\mathrm{n}} = C_{\mathrm{n}} \frac{\omega_{\mathrm{n}} + Q_{\mathrm{n}}(E - E_{\mathrm{n}})}{\omega_{\mathrm{n}}^2 + (E - E_{\mathrm{n}})^2} + B_{\mathrm{n}}, \tag{4.3}$$

where α_{n} is the absorption in optical depth, C_{n} is related to the oscillator strength, E_{n} is the energy of the state, ω_{n} is the linewidth, Q_{n} is the asymmetry and B_{n} is a constant term accounting for the background absorption. Fittings were obtained by selecting energy ranges to separate and individually fit each excitonic state. Here, the energy ranges are selected such that adjacent ranges would be as close to one another as possible without overlapping. Once these had been selected, eqn. 4.3 was fit to the resulting feature. This method of local fitting was used over a global fitting procedure due to degeneracies arising from the asymmetric lineshape. Because eqn. 4.3 allows for a negative contribution to the absorption situations that can arise in which neighbouring states essentially "correct" for each other in the fitting procedure. Such a global fitting may result in the fitting of adjacent states to be highly related.

The characteristic decrease in feature size and width with increasing principal quantum number can be seen. Alongside this, the typical reduction in spacing between adjacent states is visible. Moreover, the asymmetry of the states is changing, seeming to increase towards the band edge. These changes are illustrated in Fig. 4.5. This shows the expected n^{-2} dependence on the energy levels of excitonic states, yielding a Rydberg constant of (88±3) meV, a band gap of (2.17207±0.00008) eV, and a quantum defect of 0.2±0.1. These are in agreement with previous measurements [58]. The oscillator strength initially scales with the expected n^{-3} scaling up to 11P. Beyond this, it drops off much faster with n^{-12}. This may originate in interactions between the high-lying excitonic states, but it is more likely a result of defects within the crystal structure. Defects will disproportionately impact the highest principle quantum number states owing to their exaggerated radii.

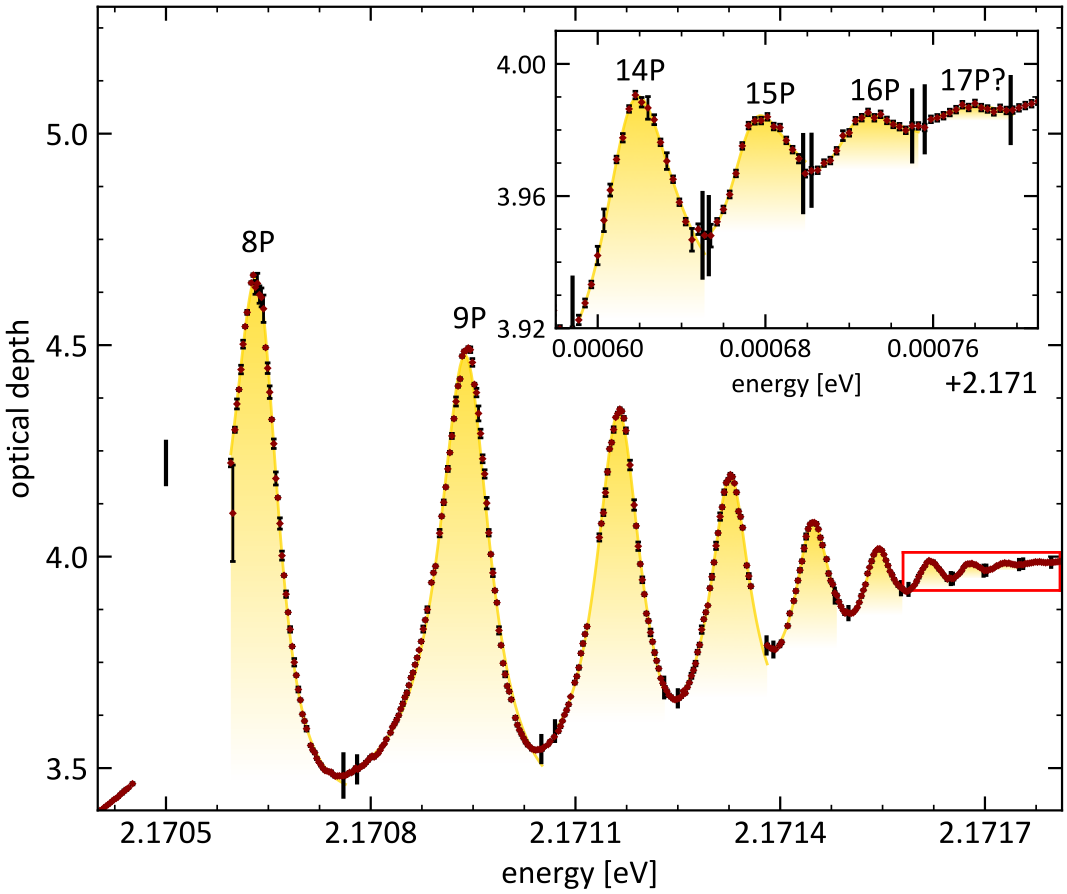

Figure 4.4: Transmission spectrum of cuprous oxide at 5 °K. The fit shown by yellow shaded regions gives excellent agreement with the experimental data. Small black vertical lines indicate the energy ranges used to fit each excitonic peak. Inset shows the region in the red box showing the very highest nP states. While there is an additional feature beyond 16P it is not clear that this is 17P.

The line widths appear to deviate from the expected n^{-3} dependence at low n, falling instead more slowly than expected. Then for high n the agreement is much stronger. The dependence on n is more accurately captured by a n^{-3} with an additional constant. In both cases, the width of the 8P exciton is poorly predicted, but the apparent narrowness of this feature is due to the laser being multi-mode during the scanning at 5 °K. The unexpected dependence on n likely physically originates in crystallographic inhomogeneity. This will disproportionately impact high-lying states owing to their larger physical extents. Such inhomogeneity can result in the broadening of states and similar results have been reported by Kazimierczuk et al [58]. It is also possible that the asymmetry parameter impacts the apparent width of the states.

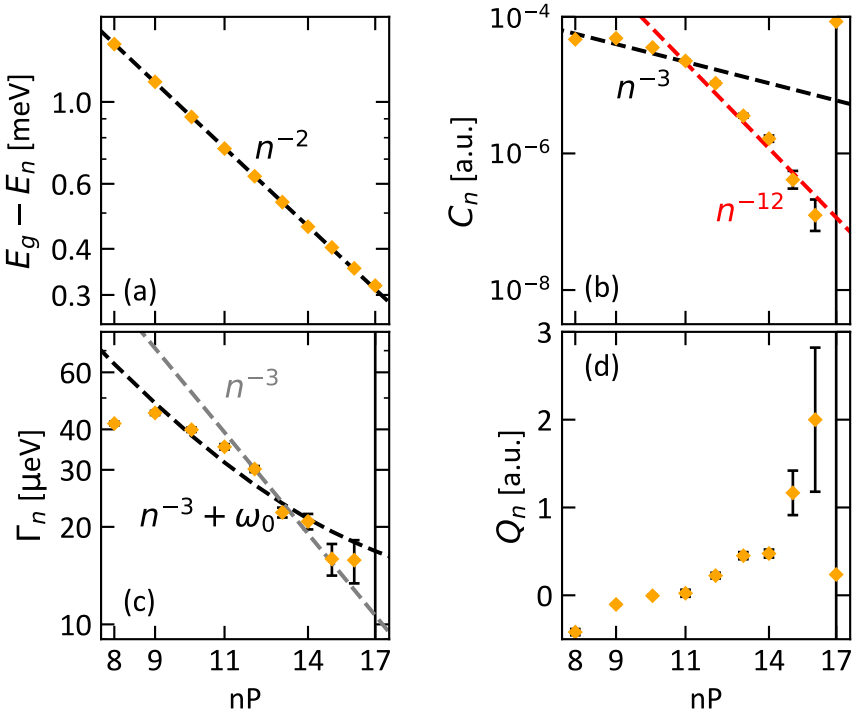

Figure 4.5: Extracted fitting parameters for the excitonic spectrum at 5 K. (a) binding energy is well described by the Rydberg formula showing the characteristic n^{-2} dependence. (b) characteristic dependence on n^{-3} trend before falling far more rapidly with n^{-12}. (c) for higher n states the expected n^{-3} dependence is observed, but this fails to describe the variation for low n. (d) asymmetry of the peaks increases with increasing nP, but limited data points lead to an unreliable fitting above 14P.

Unlike the other parameters, the asymmetry does not have a clear associated theoretical prediction. In general, it increases with increasing principal quantum number changing signs between 9P and 12P. For the states above 15P, the fitting is less reliable owing to fewer data points constituting each feature. It is reassuring to find many of the trends in fitted parameters scale with principal quantum numbers in the expected fashion. The fitting of the widths is the only major exception to this, which may find its origins in the method of fitting instead of reflecting physical phenomena. The asymmetry is perhaps the clearest illustration of the limits of this technique as they grow with increasing n. This dependency may well originate in the constant background term used in the fitting procedure. A linear background may be more appropriate as the phononic absorption becomes more significant closer to the band edge. However, this linear background would serve the same role as the asymmetry parameter: essentially

improving the fitting capability of the fitting function. As such, it is difficult to argue which is more superior in this context. We now move on to investigating how temperature impacts this spectrum. It is through the methods outlined above that the temperature dependence will be investigated.

4.3 Temperature Dependent Transmission Spectroscopy

In semiconductor systems, the most pronounced impact of temperature comes from the shifting of the band gap. As the temperature is increased the band gap is reduced [161] owing to the shifting Fermi energy of the system due to interactions with phonons [162] and the expanding crystal lattice [163]. This in turn impacts the excitonic spectrum by shifting all of the states to lower energies. This shift can be characterized by a semi-empirical model based on the Bose-Einstein statistical distribution for phonons [164]:

$$E_{\mathrm{g}} = E_{\mathrm{B}} - a_{\mathrm{b}} \left(1 + \frac{2}{e^{\Theta/T} - 1}\right), \tag{4.4}$$

where $E_{\mathbf{B}} - a_{\mathrm{b}}$ is the band gap at 0 °K and $\Theta = \hbar\omega/k_{\mathrm{B}}$ characterizes the energy of the phonons with frequency ω. This can describe the temperature dependence in archetypal semiconductors such as GaAs and InGaAs [165]. Additionally, excitons can be ionized by thermal phonons. The energy at which this occurs is characterized by E_L. As with the band gap, this parameter moves with the band gap. But, as temperature is increased so too does the energy of thermal phonons, resulting in E_L shifting more with temperature than E_g. As a result, it is the difference $E_L - E_g$ which is the main interest.

The same procedure described in the previous section was carried out over a range of different temperatures. Data was collected by scanning a particular mode of the laser and then changing the temperature before scanning the same mode again. Once all relevant temperatures were scanned the mode was then changed. The results of this are shown in 4.6. At each temperature, the laser was scanned until excitons were no longer resolvable.

Several trends can be seen in this data. The first is the change in energy of the 10P exciton, corresponding to the shifting of the band gap with temperature. The

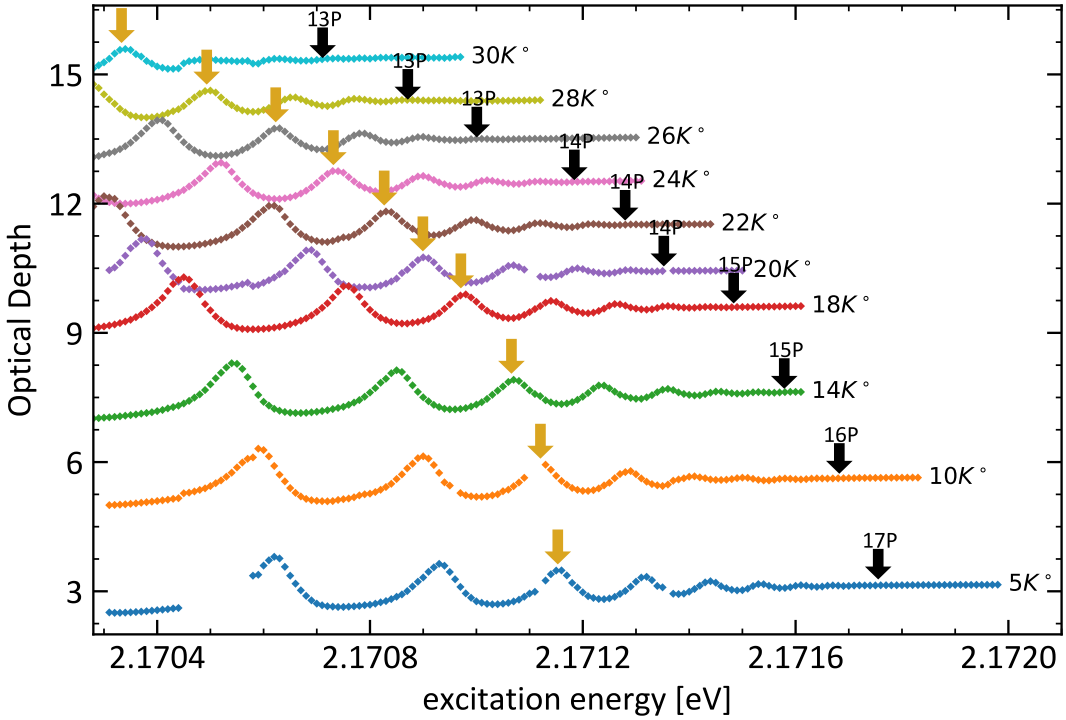

Figure 4.6: Change in excitonic spectrum with temperature. Subsequent temperatures have been offset vertically for clarity. The golden arrow corresponds to the position of the 10P exciton. This shifts with the band gap as the temperature is increased. The black arrow shows the highest resolvable exciton at each temperature. Gaps or discontinuities in the spectra are the result of the laser not being single mode during part of the scan.

shift here is nearly 1 meV from 5 °K to 30 °K. Despite this shift it does appear the relative position of the excitons is largely unchanged as the temperature is increased. This is confirmed by fitting the resulting Rydberg series as shown in Fig. 4.8. This fitting protocol is less effective for the highest temperatures as there are far fewer resolvable excitons. However, up to 26 °K, there is no clear change to the extracted quantum defect or binding energy. This is in line with the band gap shifting, which is well described by using the Vina function yielding a band gap of 2.17204 eV and Θ =74. In particular, this measurement of Θ is comparable to the value extracted by Kang et al. of $\Theta \approx 100$ [166]. With the bandgap being very much in line with the measurements made in the previous section.

The other clear impact of temperature is the limit to resolvable states. This varies from 16P at 5 °K and drops to 13P at 30 °K, as indicated in Fig. 4.7. As temper-

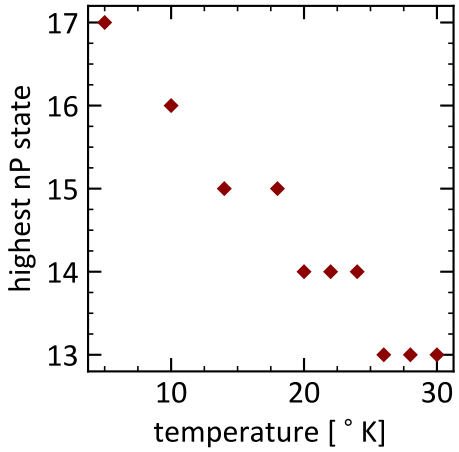

Figure 4.7: Temperature limited observation of high nP states. As temperature is increased the highest resolvable nP state decreases. The rate at which this occurs slows down with increasing temperature.

ature is increased the rate at which states become unresolvable slows. This is a reflection of the larger oscillator strength of lower nP states. States are initially 350 µeV away from the band edge, growing to around 450 µeV at the highest temperatures. Given the characteristic thermal energy at 5 °K, which is approximately 400 µeV this observation supports high-lying states being thermally ionised. Furthermore, the convergence to 16P as the highest observable state as temperature is decreased also supports this hypothesis. An additional check of this can come in the form of comparing the excitonic binding energy with the characteristic thermal energy. At 30 °K the ratio of characteristic binding energy to the 13P binding energy is ∼5. This value is notably higher than the same ratio for the 16P exciton at 5 °K which is 1 instead. This discrepancy suggests that the relationship between $k_{\mathrm{B}}T$ and the highest observable exciton is not simply a linear one owing to the Boltzmann factor. Part of the reason for this may lie in the larger oscillator strength of lower-lying excitonic states. This may lead to such states being more robust to thermal ionization due to a larger excitonic population.

The results shown in Fig. 4.7 imply that additional states would become resolvable if the experiments were carried out at a lower temperature. However, the trend appears to be largely linear, suggesting that only up to around 20P could be resolved at 40 mK, in contrast to 25P in [58]. The discrepancy between these values is likely due to differences in sample quality, namely in the inclusion of

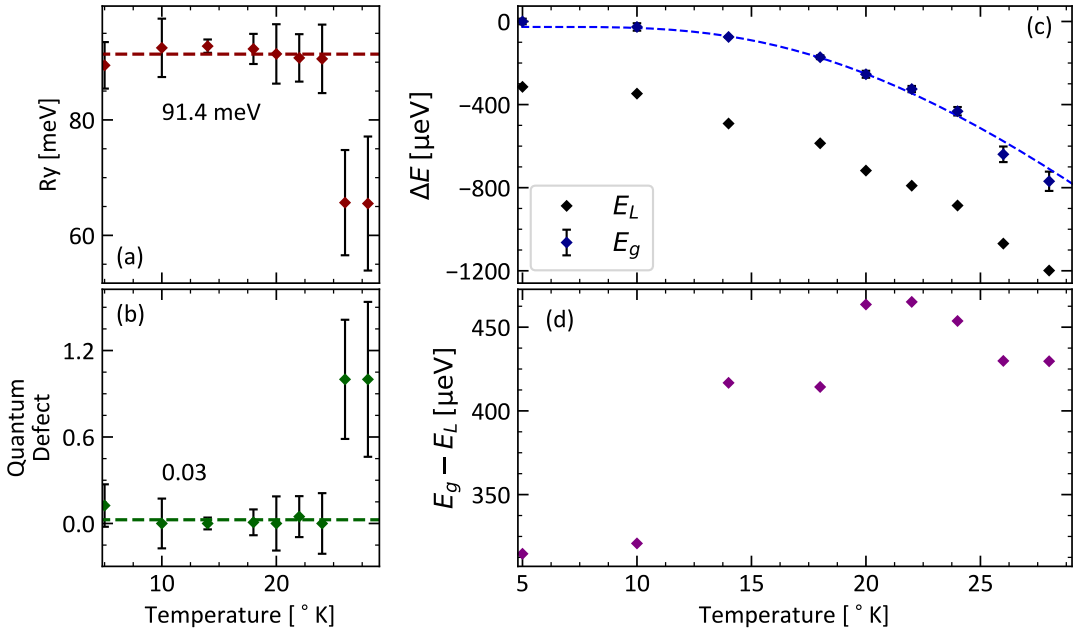

Figure 4.8: Fitting parameters of the excitonic spectrum at different temperatures. (a) and (b) show that the binding energy and quantum defect do not depend on temperature until the very highest temperatures. (c) variation in band gap and highest resolvable n state. The band gap shift is well described by the Vina function, plotted as a blue dashed line. (d) the difference in energy between the highest lying observable state and the band gap.

defects. Such defects reduce the oscilator strength of higher-lying excitons, as was previously discussed with regards to Fig. 4.5. As such, we conclude that we are limted by both the temperature and the quality of the sample. By fitting the 10P exciton line at each temperature it is possible to investigate the more subtle changes in lineshape. Such fittings are shown in Fig. 4.9. There is a clear reduction in oscillator strength and an increase in the width of the exciton features. The former corresponds to increasing thermal ionization of the excitons, while the latter shows thermal broadening of the states due to the increased population of phonons. Notably, the asymmetry remains largely unchanged as the temperature is changed. This seems to suggest that this property is, for the most part, independent of the population of thermal phonons. These observations are comparable with results observed by Kang et al [166].

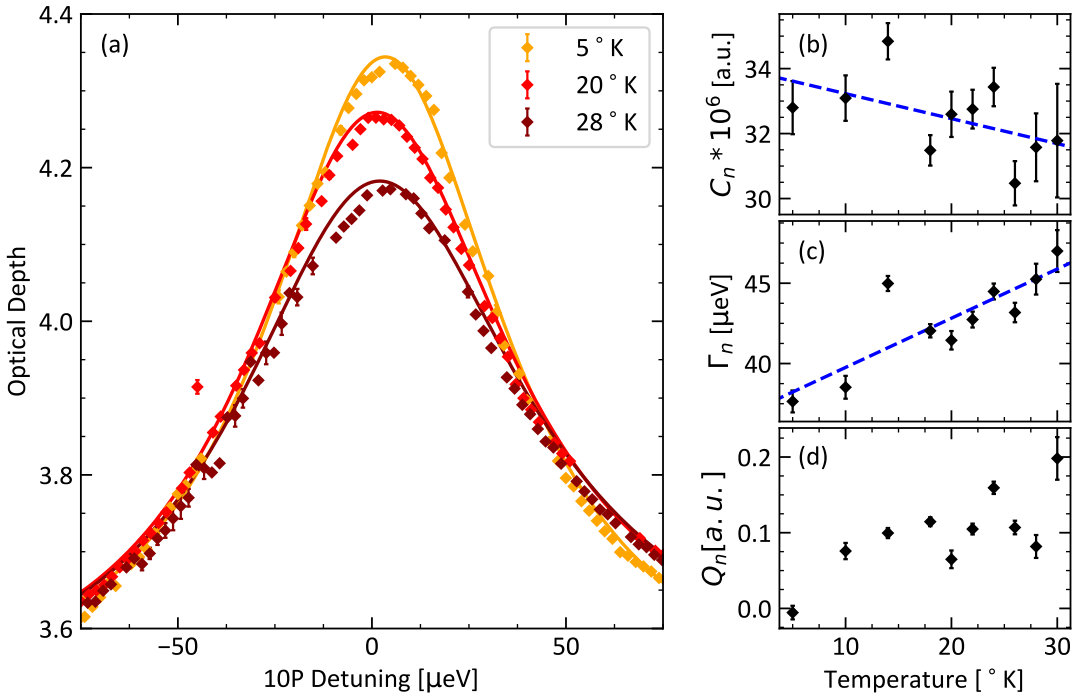

Figure 4.9: Variation in the 10P exciton as the temperature is increased. (a) 10P feature becomes noticeably lower and broader with increasing temperature. This is more clearly shown in (b) and (c). (b) variation in the oscillator strength with increasing temperature. There is a weak linear decrease in oscillator strength which is indicated by the dashed line. (c) linewidth increases linearly with increasing temperature. This is indicated by the dashed line. (d) variation in the asymmetry of the 10P state. For most temperatures, the asymmetry is approximately constant around 0.1 a.u. Only the highest and lowest temperatures break this trend.

4.4 Conclusions

Transmission spectroscopy was carried out using a narrowband tuneable visible laser to determine the factors limiting the resolution of higher nP states in our samples. At 5 °K odd-parity excitonic states up $n = 16$ were resolved and the trends in those states generally fit well with previous reported findings. Notably, the band gap was measured to be 2.170274(8) eV with a binding energy of (88±3) meV. The behaviour in the line widths however with increasing n did not follow the expected n^{-3} dependence. This deviation has been attributed to inhomogeneities in the crystal lattice and the nature of the asymmetric lineshape used for fitting.

By then resolving the excitonic spectrum over a range of temperatures up to 30 °K it has been determined that the most significant factor limiting the observation of higher n states is the temperature of our system. This comes from the highest state observable at each temperature converging to $n = 16$ as the temperature is decreased. Additionally, the increasing gap between the band gap edge and the highest resolvable state with temperature implies an increasing tendency towards ionization. Within this range of states, the binding energy is of a similar order to the characteristic thermal energy. Alongside this, the shifting in the band gap with temperature was studied yielding comparable fitting parameters to other measurements made in this material.

Chapter 5

Microwave Induced Nonlinearities

The primary focus of this thesis so far has been the study of what limits the observation of high principal quantum number states in cuprous oxide. While our system is limited by the relatively high operational temperature of 4 °K, we are still able to resolve far enough into the excitonic spectrum to make use of exaggerated Rydberg properties. Of particular interest is the large dipole moments, originating from the large physical extent of Rydberg excitons, enabling strong coupling to external fields. Here, we seek to utilise the microwave frequency separation between opposite parity states, alongside the large dipole moments, to observe microwave-induced nonlinearities. Owing to cuprous oxide possessing an inversion symmetry such nonlinearities are described by the $\chi^{(3)}$ nonlinear electronic susceptibility.

Among these nonlinearities, we are particularly interested in the modulation of the phase of transmitted light due to the Kerr effect. The corresponding Kerr coefficient measured here is of the order of 10^{-2} mV^{-2}. This is several orders to magnitude larger than what is observed in the archetypal Kerr medium of nitrobenzene [167] or even Rydberg atoms [152; 168]. Most atmospheric gases have a Kerr coefficient of the order of 10^{-12} mV^{-2} [169]. A table of Kerr coefficients is shown in table 5.1. This takes all-optical processes one step closer to realisation and further cement the role of cuprous oxide as a viable platform for atomic physics in the solid state.

This chapter will outline the modifications to the previous experimental setup needed to measure the Kerr effect. Principally, these changes take the form of the capability to apply microwave frequency fields across the sample, to spectrally

Media	Kerr Coefficient [mV^{-2}]
Water	10^{-16} [167]
Carbon di-sulphuride	10^{-14} [167]
Nitrobenzene	10^{-12} [167]
Rydberg Atoms	10^{-6} [152]
Rydberg Excitons	10^{-2}

Table 5.1: Comparisons between the orders of magnitude of the measured Kerr coefficients in different media.

resolve the transmitted light and to determine the polarisation state of the transmitted light. This modified setup will then be used to determine the elements of the $\chi^{(3)}$ tensor for our geometry and extract a Kerr coefficient by examining the additional frequency responses due to the microwave field. The predicted value is comparable to a parameter-free model based on an atomic approach as laid out in Chapter 2.

5.1 Experimental Methods

This section will describe the experimental setup used throughout this chapter, which is largely similar to that used in the previous chapter. However, there are three key changes to the setup. The first is the addition of a stripline antenna, and a microwave amplifier, enabling high-power microwave fields to be applied across the sample. The second is the addition of a Fabry-Perot etalon (FPE) (LightMachinery OP-7423-1686-1) to spectrally resolve transmitted light. The etalon had a free spectral range (FSR) of 59.2±0.2 GHz and a finesse of 42.6±0.3. The third is control over the input polarisation state and the capability to determine the polarisation state of the transmitted light. Finally, the balanced photodiode was replaced with a photon counter. These changes are indicated in Fig. 5.1. Each of these changes will be described in greater detail throughout this section.

Overall, the purpose of these modifications is to enable the observation of changes to the spectrum as high-power microwave fields are applied across this sample. This can take the form of changes in transmission, polarization or the additional frequency components in the transmitted light. In the simplest case, where only transmission is concerned, this can lead to changes in the excitonic spectrum as shown in Fig. 5.2. Many aspects of the excitonic spectrum are still visible, such as well-defined peaks at nP resonances and troughs between. But the transmission

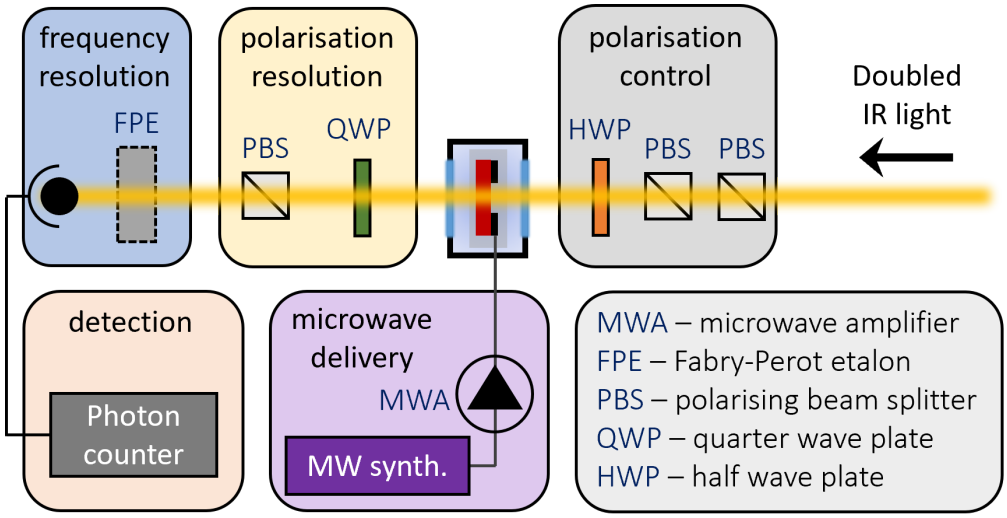

Figure 5.1: Modifications to pre-existing setup for transmission spectroscopy, enabling spectral and polarisation resolution of transmitted light. The FPE used had a finesse of
Additionally, enables the control of input polarisation and the delivery of microwave fields across the sample.

on nP states reduces, while between nP states it increases. This can be interpreted as a mixing of the S and P-like characters resulting in more S-like characters at the nP resonance, and thus less absorption.

5.1.1 Delivering Microwave Fields

In the vast majority of materials the Kerr coefficient is very small [167]. As such, the length of the Kerr medium must be long, often in the form of long cells, and the power of the applied electronic field must be high. In this setup, the absorptive nature of cuprous oxide requires that only very thin samples are used, ∼100 um. As such, it is important that high-power microwave fields can be delivered across the sample. In this setup, the microwave field is generated using a microwave synthesizer (Rhode & Schwarz SMB100A). To then obtain the required high powers the field is amplified through a microwave amplifier (minicircuits TVA-82-213A+). The field is delivered by placing a sample of cuprous oxide between the two wires of a stripline antenna. Further details of this can be found in [55]. The characterization and implementation of this system are shown in Fig. 5.3. As before, the sample is mounted on a transparent CaF_2 window placed over a hole in the antennae to enable optical access.

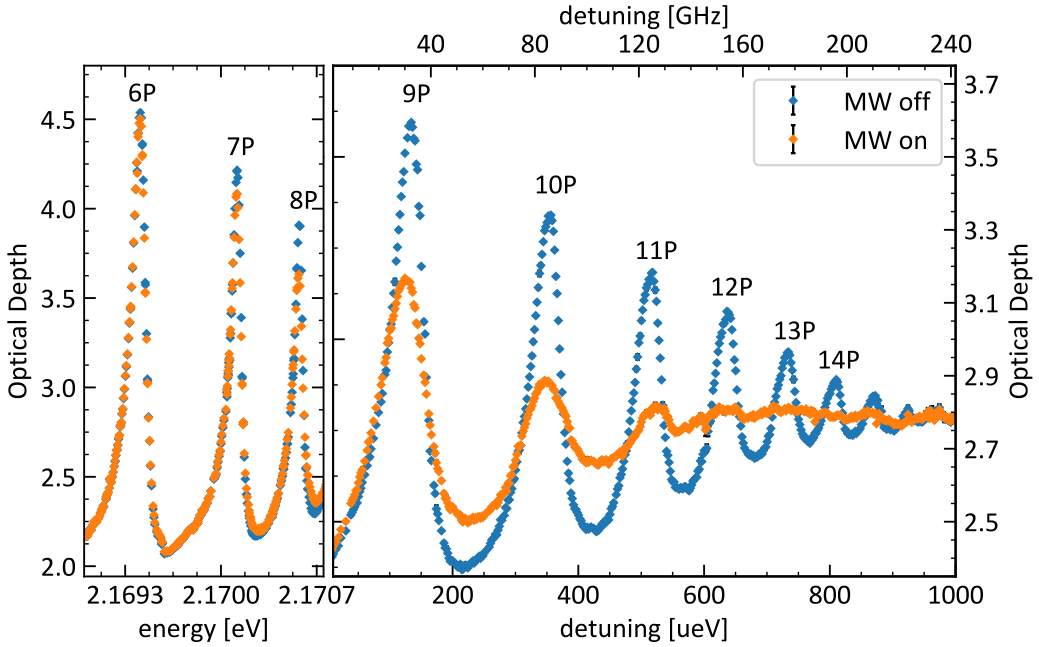

Figure 5.2: Modified excitonic spectrum due to the application of a 75 mW 7 GHz microwave field across the sample. For states above 12P, the lineshape is changed so dramatically that the nP states can no longer be resolved. Clearly towards higher principal quantum numbers states are separated by 10s of GHz.

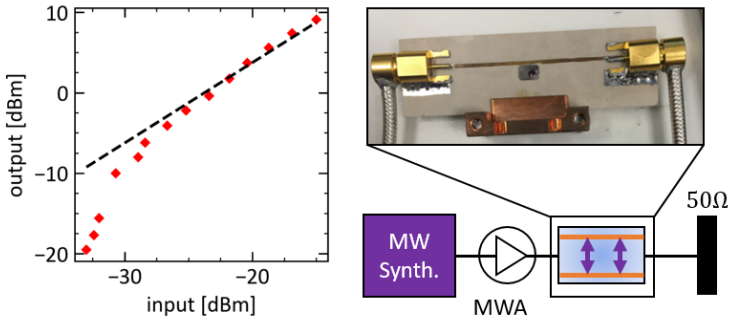

Figure 5.3: Characterisation and delivery of microwave fields across the sample. Left: determination of amplifier gain. The dashed line shows a linear gain of 24 dBm. The discrepancy at low input powers arises from the detection floor of the spectrum analyser. Right: schematic of implementation of antennae. Pictured is the antennae with a sample mounted in a clear aperture.

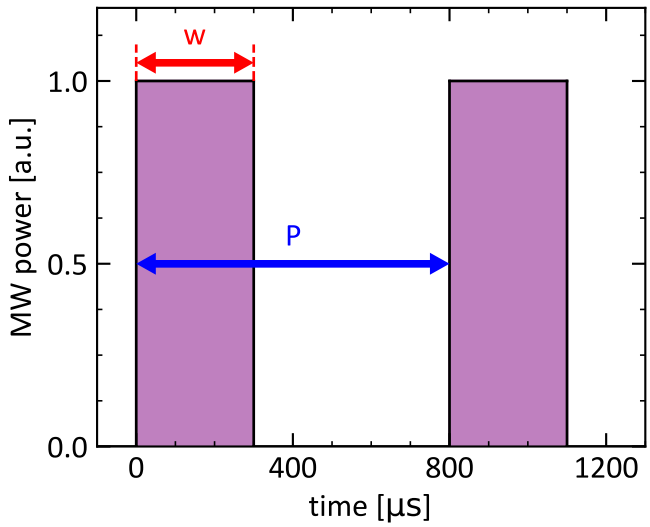

Figure 5.4: Illustration of pulse width, w, and pulse period, P. The duty cycle is the proportion of time a microwave field is applied for and is characterised by the ratio of w to P.

The microwave field was applied across the sample in pulses. These are characterised by a time period between subsequent pulses, the pulse period, and the length of time the microwave field is on for, the pulse width. By using these pulses to trigger the photon counter it is simple to separate where the microwave field is on and off in the transmitted intensity. The relationship between these parameters is described by the duty cycle, as illustrated in Fig. 5.4. Throughout this chapter, the pulse period is 800 μs.

A consequence of using high-power fields is the heating of the sample mount, and correspondingly the sample, due to the finite resistance of the copper strips. Heating can be prevented by reducing the duty cycle as the microwave power is increased, leading to constant time-averaged power. The maximum allowed power was determined by scanning over the 11P exciton to identify shifts in the peak. The duty cycle is then set according to:

$$D = P_0/2P, \tag{5.1}$$

where P_0 is the highest power that does not result in heating and P is the power of the microwave field. For powers below this value, the duty cycle was set to 0.5. The heating and corresponding duty cycles are shown in Fig. 5.5. At low microwave powers, there is still heating of the sample. This was deemed adequate to prevent the duty cycle from dropping so low that data could not be acquired

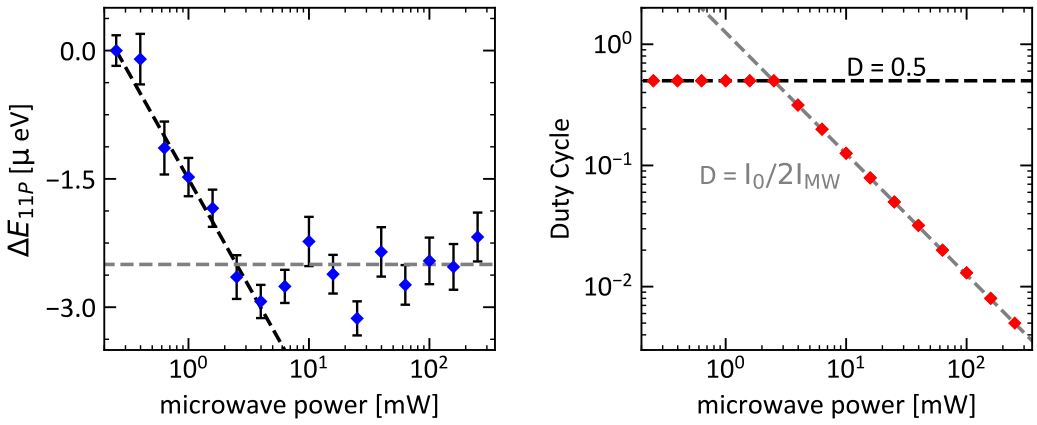

Figure 5.5: Heating resulting from high microwave power and the duty cycle implemented to prevent this. Left: Shift in the 11P exciton, black line corresponds to a duty cycle of 0.5, grey line is the duty cycle set by 5.1. Right: Duty cycle for a range of microwave powers used.

in a reasonable time frame.

5.1.2 Frequency Resolving and Sidebands

The different frequency components of the transmitted light are resolved using a Fabry-Perot etalon (FPE). Scanning the etalon reveals the spectrum of the transmitted light. In this experiment, the frequency-resolved transmission is made up of "the carrier", which is at the same frequency as the laser, and sidebands spaced at integer multiples of the microwave frequency to either side. This results in a spectrum like the one shown in Fig. 5.6. Further details on the setup and characterisation of this etalon can be found in [55]. The etalon has also been used extensively to study the $\chi^{(3)}$ nonlinearity in the SHG regime [74]. The resonant frequency of the etalon is determined by its width, which is controlled by its temperature. Scanning the etalon involves resolving frequencies over its free spectral range (FSR) with the carrier frequency in the centre.

The optical processes describing the change in the carrier, and the appearance of the sidebands are quite similar. In each case, the optical photon excites an odd parity P-state which then transitions to another P-state via an intermediary S/D state using microwave photons. The distinction between the processes is in the final P-state, as illustrated in Fig. 2.6. The large line widths and small spacing between states relax the criteria that such processes need to be resonant. Indeed,

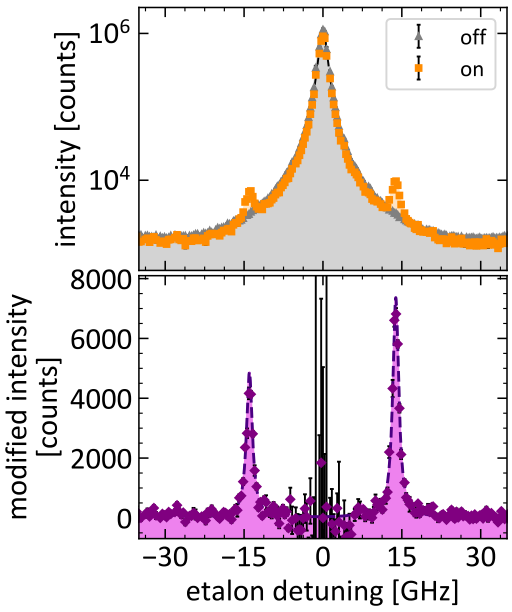

Figure 5.6: Archetypal spectrum obtained by frequency scanning the etalon. The FSR is 60 GHz, meaning scanning further in either direction would result in repeating features. Top: Spectrum of the transmitted light as a function of the detuning of the etalon with the microwave on/off. The microwave frequency and power were 7 GHz and 35 mW respectively. Sidebands are visible at the second harmonic of the microwave frequency Bottom: Spectrum after subtraction of the scaled carrier from the microwaves off data. Sidebands are approximately 2 orders of magnitude smaller than the carrier.

as many of these states are overlapping, particularly at high principal quantum numbers, these processes occur at virtually all laser detunings. An advantage of such a system is that a significant response can be seen at a range of microwave frequencies as well.

Throughout this thesis, a microwave frequency of 7 GHz was used. There are two key reasons for this choice of frequency. The first is that the metallic internal structure of the cryostation creates a surprisingly resonant structure at microwave frequencies, more details of this can be found in [74]. The result of this is that large amounts of the field can couple to this structure instead of being applied across the sample. This effect is at a manageable level at 7 GHz. Additionally, this frequency results in sidebands appearing at 14 GHz and 28 GHz, meaning they do not overlap due to the FSR of the etalon and they are far enough apart to be easily resolvable.

5.1.3 Resolving Polarisation

The polarization state of transmitted light was determined using a quarter wave plate and a linear polarising filter. Light is first passed through the QWP, then the LP before its intensity is recorded. By then rotating the QWP through 180 degrees to obtain the following curve:

$$\mathrm{I}(\theta) = \frac{1}{2}(A + B\sin(2\theta) + C\cos(4\theta) + D\sin(4\theta)), \tag{5.2}$$

where the parameters A, B, C and D in turn relate to the Stokes parameters by:

$$\begin{aligned} S_0 = A - C, S_1 = 2C \\ S_3 = 2D, S_4 = B, \end{aligned} \tag{5.3}$$

allowing for experimental measurement of the Stokes parameters. The typical results from this experiment are shown in Fig. 5.7. The Stokes parameters are capable of describing unpolarised states of light as well as fully polarised states. The ratio of the polarised to unpolarised fraction of light is described by the degree of polarisation, D_P, in terms of the Stokes parameters:

$$D_\mathrm{P} = \frac{S_1^2 + S_2^2 + S_3^2}{S_0^2}, \tag{5.4}$$

and takes values $0 < D_\mathrm{P} < 1$ with 0 corresponding to fully unpolarised light and 1 to fully polarised light. Converting from a polarisation state which is partially polarised to one that is fully polarised is achieved simply by multiplying S_0 by D_P. This was carried out throughout this work such that only the polarised component of the transmitted light is considered. The source of unpolarised light is from random scattering off the surface of the sample and from scattering throughout the setup. Typically, the D_P is of the order of 0.70. Often it is not convenient to directly compare the Stokes parameters to one another, instead, their normalised counterparts, S_n^norm, are used. These are defined according to:

$$S_n^\mathrm{norm} = \frac{S_n}{S_0}, \tag{5.5}$$

where S_n is one of the three Stokes parameters with $n > 0$. This describes the fraction of light which is in each polarization state. A compact way of showing the normalised polarisation state is by plotting it onto a unit sphere known as the Poincare sphere. Each point on this sphere is a different normalised polarisation

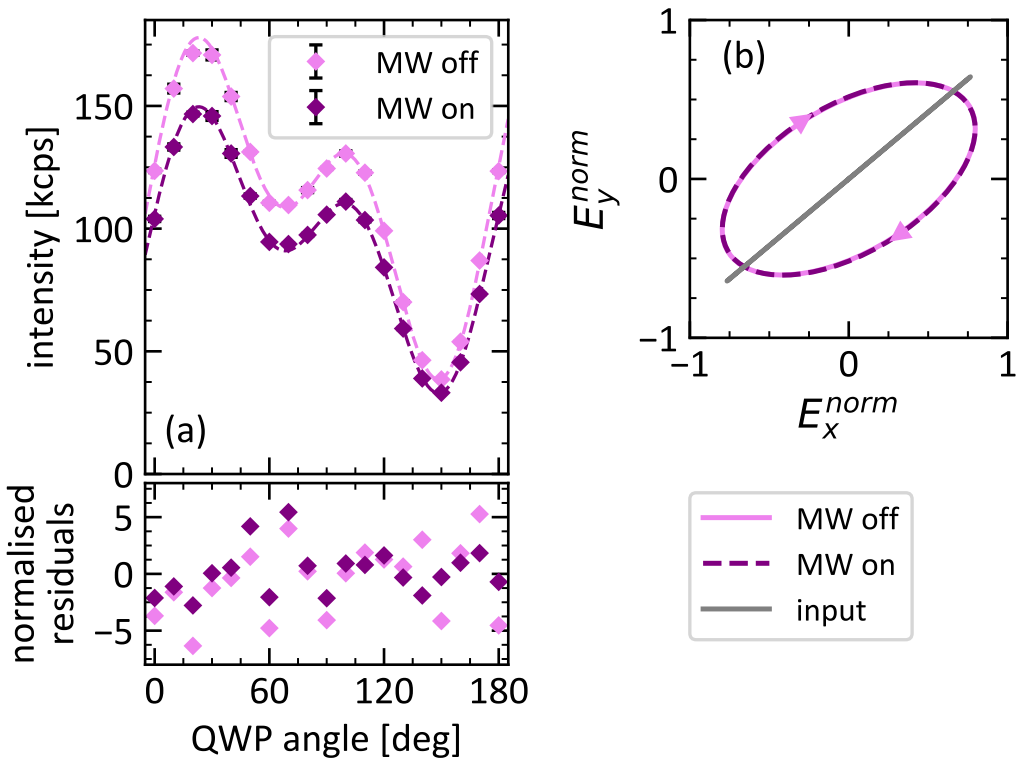

Figure 5.7: Typical results for resolving the polarisation state of transmitted light. This data was collected at 2.1713 eV, on the blue detuned side of 11P, using a microwave power of 16 mW. (a) The typical lineshape from rotating the QWP through 180 degrees. Normalised residuals show a good agreement between fitting and data. (b) Polarisation ellipse corresponding to the data shown in (a) as well as input polarisation. The field parameters have been normalised such that the time-averaged magnitude of the field is 1.

state. Furthermore, the polarisation state of the sidebands and carrier can be measured separately using the FPE.

There are several challenges associated with resolving the output polarisation as the input polarisation is varied. The first is as a result of rotating the HWP to control the input polarization can alter the alignment of the system, and so change the resulting intensity. Here, this misalignment could change the resulting intensity by up to 30%. As such it is not possible to directly compare the measured Stokes parameters between different laser detunings. Instead, it is the normalised Stokes parameters which are compared. However, this does not allow for meaningful comparisons between S_0. The only interest in S_0 from these experiments is in how it changes when the microwave field is applied. As such the fractional change in S_0 as a result of the microwave field can be used. This is

defined as:

$$\Delta S_0^{\text{frac}} = \frac{S_0^{\text{on}} - S_0^{\text{off}}}{S_0^{\text{off}}}, \tag{5.6}$$

where S_0^{off} is S_0 without a microwave field applied across the sample and S_0^{on} is S_0 when the microwave field is applied.

Resolving the polarisation of the different frequency components of the transmitted light also poses a logistical challenge. It is impractical to scan the FPE to resolve all transmitted frequencies while simultaneously resolving the output polarization. As such the second-order sidebands and the carrier were resolved by selecting three frequencies which correspond to each feature. While this does dramatically speed up the process it does introduce a new problem: the etalon does not always achieve the same temperature under the same conditions. This can result in the frequency being up to 1 GHz off from the target frequency. At the frequency of the carrier, a microwave response can still be resolved in these cases. But for the sidebands, this is not always the case as the sideband response is typically 2-3 orders of magnitude smaller, with intensities of only a few thousand counts in many cases.

5.2 Determining $\chi^{(3)}$ Elements

This section will outline the experimental determination of the elements of the $\chi^{(3)}$ tensor of cuprous oxide. This will be achieved by resolving the polarisation state of transmitted light using the setup indicated in Fig. 5.7. The nonlinear contribution to the polarisation induced in the medium can result in a change to the polarisation state of the transmitted light. As explored in Chapter 2, the geometry of this setup, alongside the intrinsic symmetries of cuprous oxide, leads to the nonlinear contribution to the polarisation state taking the following form:

$$\mathbf{P}^{(3)} = \begin{pmatrix} \frac{1}{2}(\chi_{\text{xxxx}} + \chi_{\text{xxyy}} + 2\chi_{\text{xyyx}})\cos(\theta) \\ \frac{1}{6}(\chi_{\text{xxxx}} + 5\chi_{\text{xxyy}} - 2\chi_{\text{xyyx}})\ \sin(\theta) \\ 0 \end{pmatrix}, \tag{5.7}$$

where χ_{ijkl} are the elements of the $\chi^{(3)}$ tensor. The polarization state of the carrier and sidebands was resolved from the 10P exciton to the 12P exciton in small increments. Doing so would result in polarisation dependence around the

11P exciton being fully characterised. This state in particular was selected owing to the significant response in the presence of the microwave field up to the highest possible powers. Furthermore, the 11P state still has a significant oscillator strength, which drops off rapidly for higher nP. Four microwave powers were used, spanning two orders of magnitude, to explore the power dependence of the polarization. At each detuning the input polarisation was varied by rotating a HWP in increments of 10 degrees through 180 degrees.

5.2.1 Carrier Polarisation

We begin our discussion of the polarisation state of the carrier with S_0, in particular the fractional change in absorption due to the microwave field. The fractional change in intensity as a function of the HWP angle is shown in Fig. 5.8. These results indicate that the fraction change in S_0 is described by two separate terms: one which is independent of the angle, and one which is dependent on the angle. This response is accurately described using:

$$\mathrm{I}(\theta) = C + A\cos(4\theta + \phi), \tag{5.8}$$

where C is describes the angle-independent response, A is the magnitude of the angle-dependent response and ϕ is the relative phase compared to the HWP angle. Both the angle-dependent and independent terms depend on the power of the microwave field. Initially, they both increase with increasing microwave power. However, the angle-independent term saturates above 63 mW while the angle-dependent term rapidly decreases above 15 mW. This results in the visibility of the angular dependence decreasing as the microwave power is increased. The visibility is characterised by the ratio of the dependent term to the independent term, and is shown for all wavelengths in Fig. 5.9. In general this results in a ratio of around 0.1 or less. However, on the red detuned side of the 11P exciton, this ratio climbs far higher, up to 0.6. The origin of this lies in the angle-independent term vanishing with the microwave response vanishing at this particular detuning.

The key takeaway from this is that the magnitude of the angle-dependent term is small compared to the angle-independent term. Thus, to first order, it is accurate to model the change in carrier intensity as independent of the plane of the linearly polarised light.

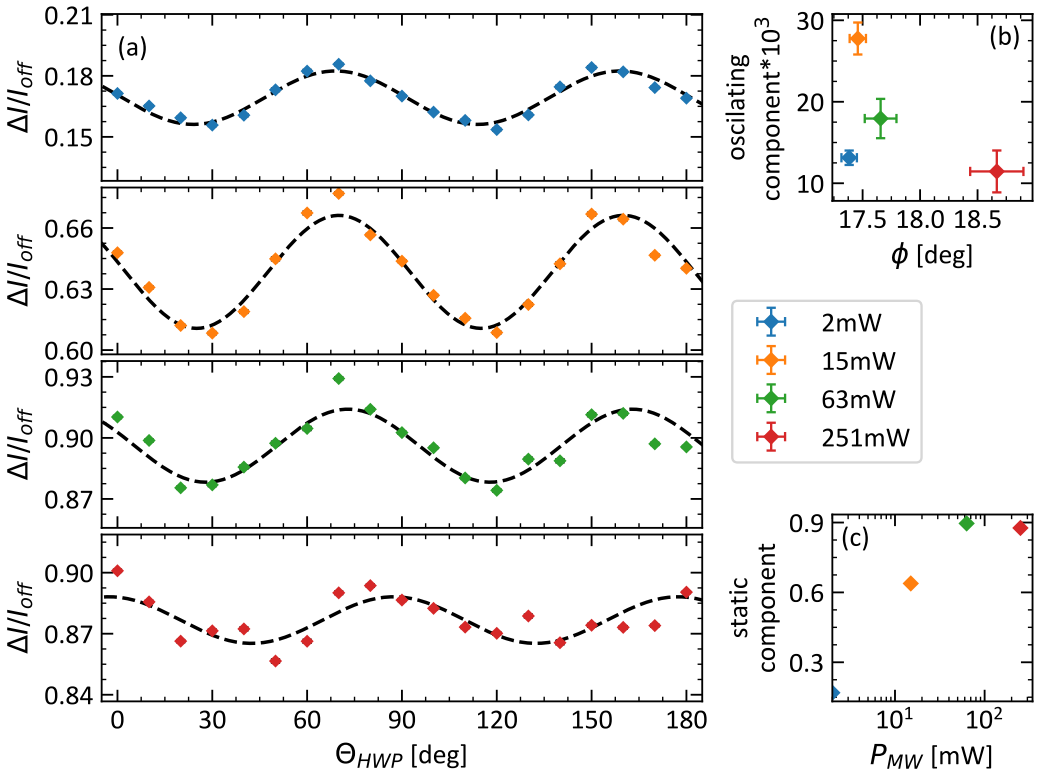

Figure 5.8: The fractional change in S_0 as input polarization is changed. (a) The fractional change can be characterised by two parts, an angle-independent part and an angle-dependent part. Both are dependent on the applied microwave power. (b) Magnitude and phase obtained from fitting. Owing to the reduced duty cycle at high powers the fitting is less accurate at higher powers. (c) Magnitude of the angle-independent part. This appears to saturate above 63 mW.

Now turning our attention to the normalised stokes parameters. These are measured using the same setup. The typical dependence of the normalised Stokes parameters is shown in Fig. 5.10. The Stokes parameters shown here can be fitted using the following function:

$$S_n^{\text{norm}} = S_n^A \cos\left(4\theta + S_n^\phi\right), \tag{5.9}$$

where S_n^A is the amplitude and takes a maximum value of 1 and S_n^ϕ is the phase. If cuprous oxide was a non-birefringent material this analysis would lead to S_1^{norm} and S_2^{norm} having amplitudes of 1 and being totally out of phase with one another. This corresponds to the polarisation state of the light after the HWP. However, these results show a clear non-zero contribution to the polarization from S_3^{norm} indicating birefringence. In this case, the fast axis appears to be at around 45 degrees to the input polarisation angle.

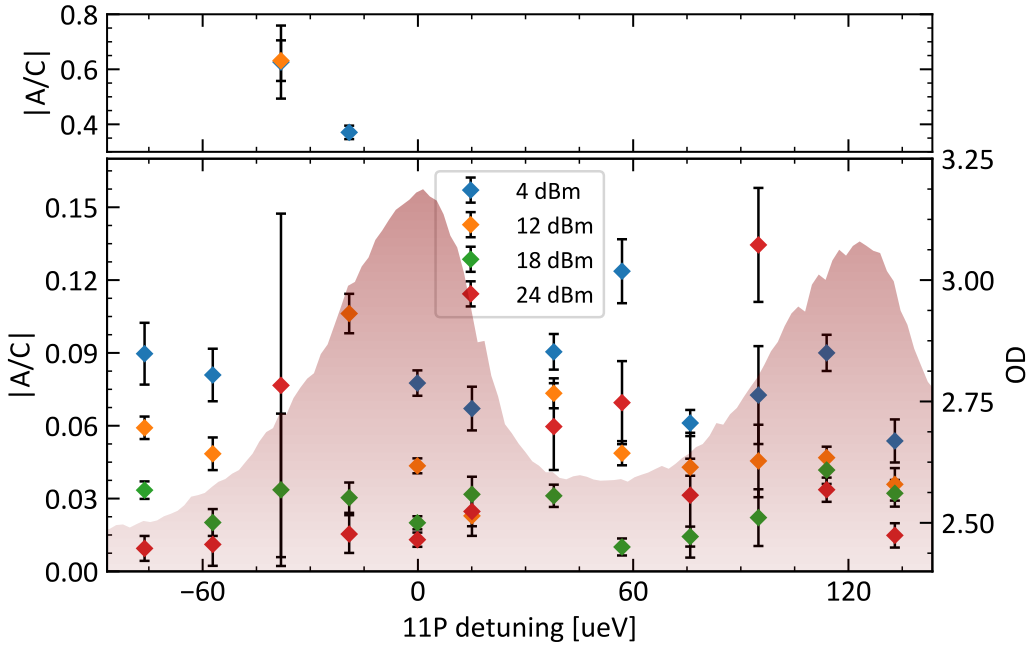

Figure 5.9: Characterisation of angle dependence on the change in S_0 parameter with input polarization. As microwave power is increased the relative impact of the variation in S_0 becomes smaller at all wavelengths.

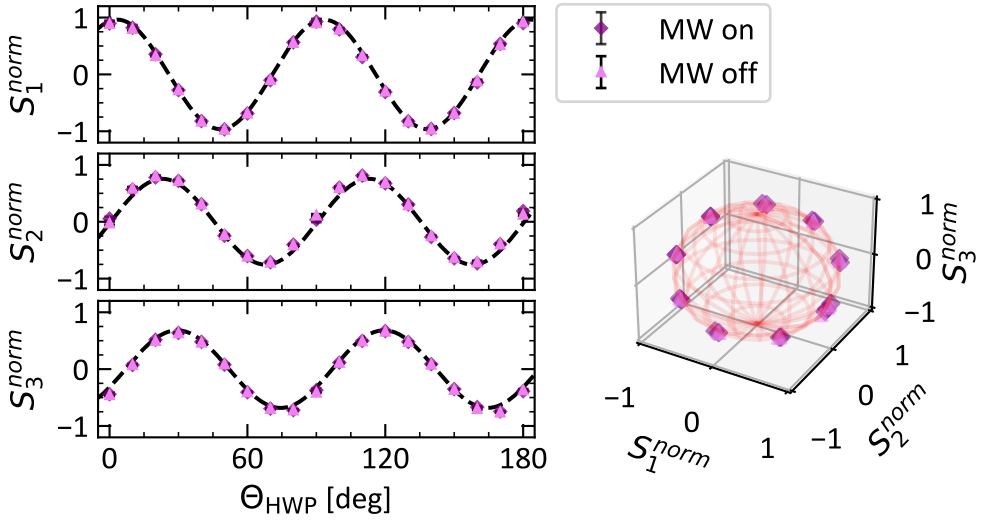

Figure 5.10: Determination of normalised polarisation at 2.16748 eV. Left: variation in normalised Stokes parameters with and without microwaves. The extracted fittings overlap with one another. Right: normalised Stokes parameters plotted on the Poincare sphere.

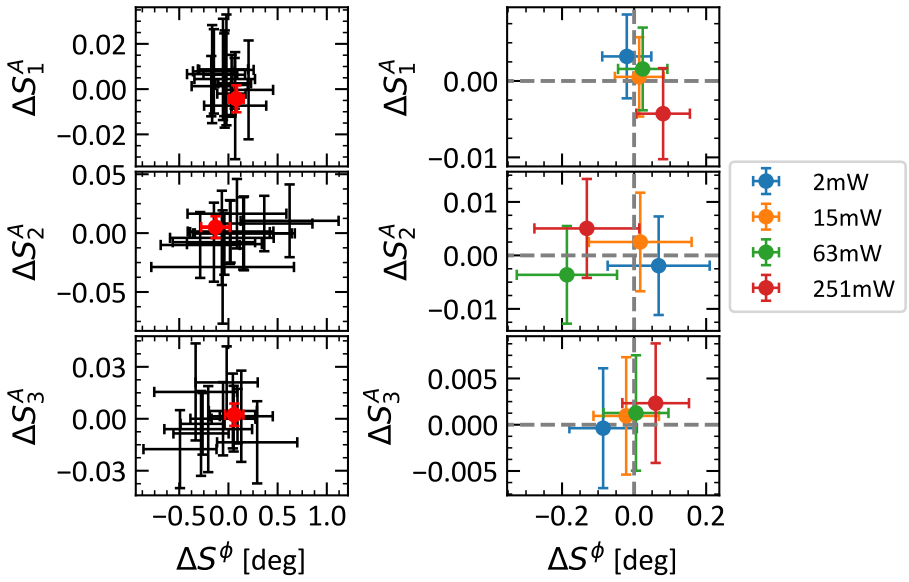

Figure 5.11: Change in normalised Stokes parameters in the presence of the microwave field. Left: change in amplitude and change in phase for the fitting parameters for S_1, S_2 and S_3 with a microwave power of 3 mW. Each black cross corresponds to a different laser detuning. The red point is the weighted average of these changes. Right: weighted mean for the four microwave powers used. In each case, these are consistent with no change in the phase or amplitude fittings.

The fitting function described in Fig. 5.9 provides an amplitude and phase for the normalised Stokes parameters at each laser detuning. A change in the polarisation state as a result of the microwave field would result in a change in these fitting parameters. The change in these parameters is shown in Fig. 5.11 all wavelengths and microwave powers. This clearly shows that in all cases any change is consistent with no change to the polarisation state.

Taking these results together, it is reasonable to conclude that there is no change in the normalised Stokes parameters of the carrier as a result of applying a microwave field across the sample. To first order, the intensity of the transmitted light is not dependent on the input polarization. However, there is a microwave-independent birefringence in the sample. We now move on to briefly discuss the same experiment on the sidebands.

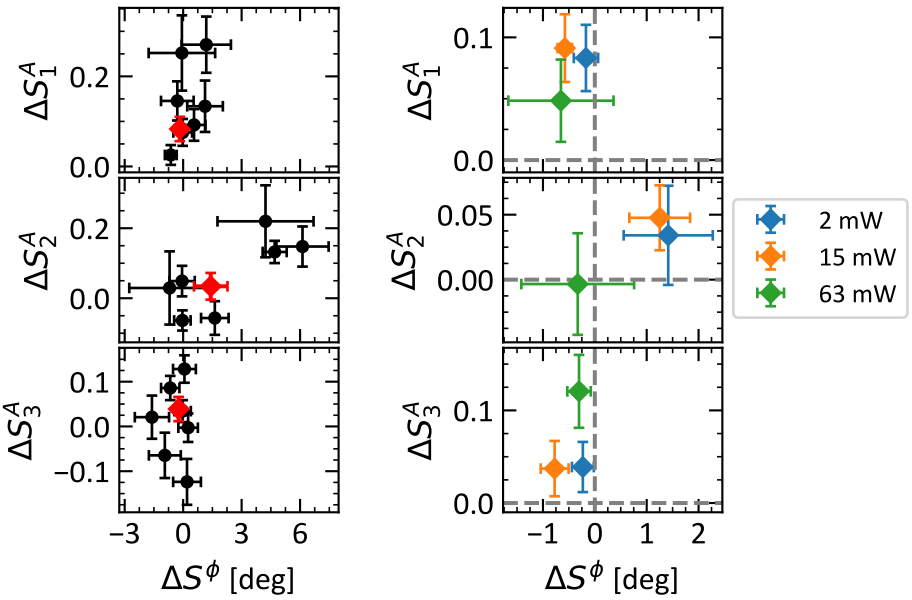

Figure 5.12: Change in normalised Stokes parameters fittings for blue sidebands. Left: change in fitting parameters for all wavelengths at 3 mW, in red is the weighted mean for that set of data. A much larger variation in extracted phase and amplitude is shown than for the carrier. Right: weighted mean for each power. In general, the results are not consistent with no change in the fittings, but large error bars challenge this.

5.2.2 Sideband Polarisation

The polarization states of the red and blue detuned sidebands were determined in the same way as the carrier. However, the polarisation states are now compared to the polarisation state of the carrier in the absence of the microwave field. For the sidebands, we study the change in the polarisation state from the carrier polarisation. As previously discussed, the small size of the sideband features combined with the imperfections of the FPE leads to the sidebands not always being resolvable. This is particularly true at the highest microwave powers where the sideband intensity is much lower. The result of this is that the quality of data obtained at the sidebands is far lower and the errors are in general larger. We will begin the discussion with the blue detuned sidebands, the change in polarisation state is shown in Fig. 5.12. Unlike for the carrier, it is not immediately clear that there is no change in polarisation state. However, many of the results are still comparable to no change in the extracted parameters. Furthermore, the lack of any clear pattern in dependence on microwave power suggests that the

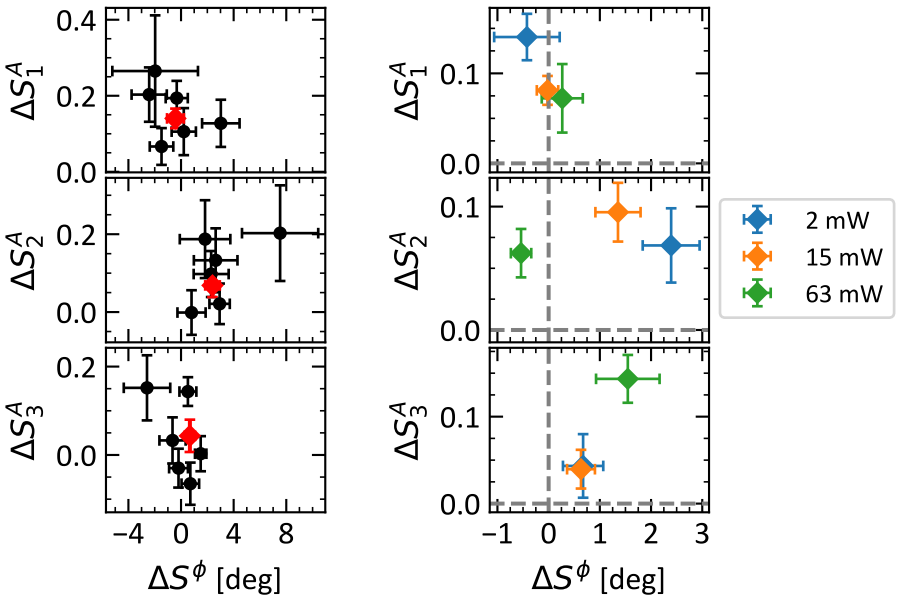

Figure 5.13: Change in normalised Stokes parameters fittings for the second-order red sideband. Left: change in fitting parameters for all wavelengths, again with the weighted mean in red. Right: weighted mean for each power. As with the blue sidebands this change is likely coming from the low quality of the data.

discrepancy originates from the far lower quality of the data instead of a genuine change in the polarisation state. Moving onto the red sidebands, Fig. 5.13 suggests much the same as for the blue sidebands. In conclusion, there is no change in the polarisation state of the carrier or the sidebands due to the application of the microwave field. This allows for an additional relationship between the elements of $\chi^{(3)}$ to be made. By recalling the derived form of the polarization from chapter two:

$$\mathbf{P}^{(3)} = \begin{pmatrix} \frac{1}{2}(\chi_{xxxx} + \chi_{xxyy} + 2\chi_{xyyx})\cos(\theta) \\ \frac{1}{6}(\chi_{xxxx} + 5\chi_{xxyy} - 2\chi_{xyyx})\ \sin(\theta) \\ 0 \end{pmatrix}, \tag{5.10}$$

and by now requiring that this has the same polarisation state as the input light leads to the magnitude of the x and y components being the same. This results in the following relationship:

$$\chi_{xxxx} = \chi_{xxyy} - 4\chi_{xyyx}, \tag{5.11}$$

as a result of the lack of change in the polarisation state. Unfortunately, this does not offer any further insight into the real or imaginary parts of the tensor elements.

5.3 Microwave Induced Nonlinearities

The $\chi^{(3)}$ nonlinearity allows for the microwave field to modify the polarisation, amplitude, phase and frequency of the transmitted light. Thus far, only the modulation of the polarisation state has been explored. This section will seek to complete the characterisation of the $\chi^{(3)}$ nonlinearity by studying the amplitude, phase and frequency modulation of the transmitted light. The phase and frequency modulations are explored using the FPE to spectrally resolve the transmitted light at a fixed number of laser detunings, much like how the polarisation data was collected. For the amplitude modulation, the laser is instead scanned over the entire spectrum due to the much higher throughput of that experiment. It is the amplitude modulation that we explore first.

5.3.1 Amplitude Modulation

We begin by recalling the change in absorption as described in Chapter 2. This change is described by the imaginary part of the nonlinear susceptibility:

$$\Delta\alpha = k\mathrm{Im}(\chi^{(3)}), \tag{5.12}$$

where k is the wave vector. This parameter is experimentally measured by first noting that the transmission through an object is given by Beer's Law:

$$I = I_0 e^{-\alpha z}, \tag{5.13}$$

where z is the distance propagated through the material. In the presence of a microwave field, the absorption is described by:

$$\alpha = \alpha_0 + \Delta\alpha, \tag{5.14}$$

where α_0 is the transmission without microwaves. By then noting that $\Delta\alpha << \alpha_0$ and Taylor expanding the exponential term the transmitted intensity is now:

$$I = I_0(1 + \alpha), \tag{5.15}$$

by Taylor expanding the exponential. From this, we note:

$$\Delta\alpha = \frac{I_{\mathrm{on}} - I_{\mathrm{off}}}{I_{\mathrm{off}}}, \tag{5.16}$$

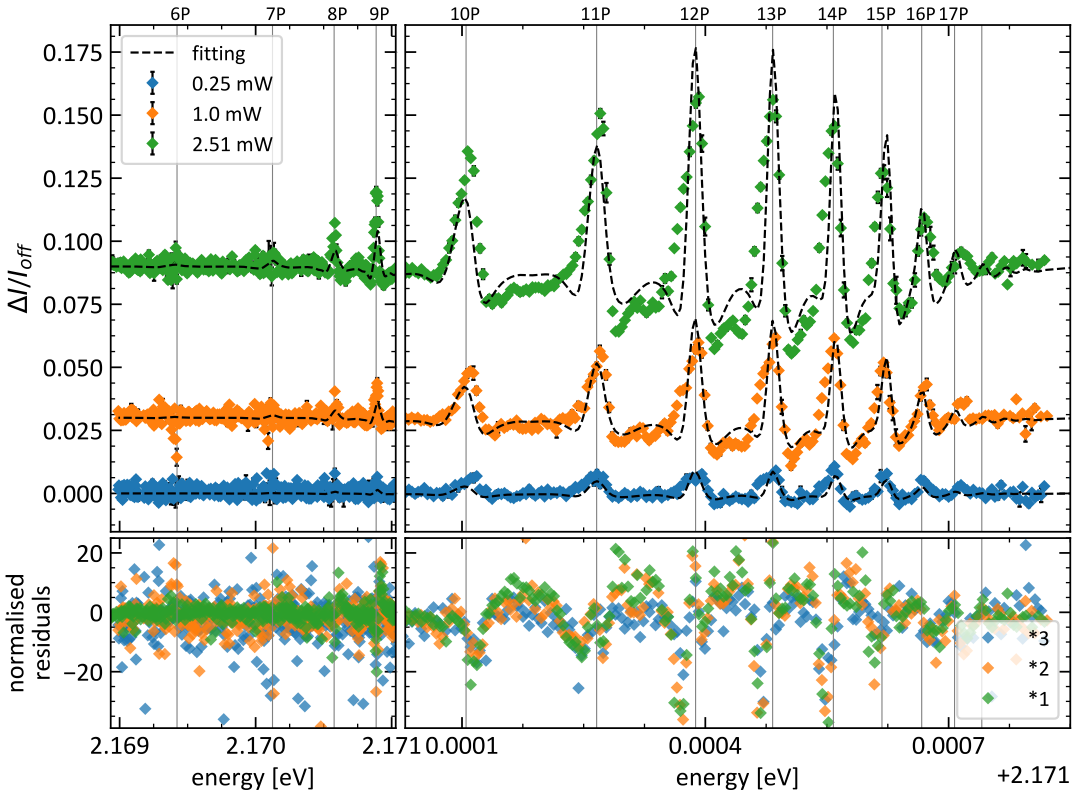

Figure 5.14: Change in transmission due to the application of a microwave field. The theory fitting shows strong agreement with the experimental data, particularly at low microwave powers.

giving us a direct measure of this quantity from the experiment. This was measured over the excitonic series at a range of microwave powers and compared with the $\chi^{(3)}$ model's prediction, as shown in Fig. 5.14. At the lowest powers, the model can provide quantitative agreement to the experimental data. This is particularly noteworthy as the only free parameter in this model is the electric field strength for the microwave field. As the microwave power is increased this agreement reduces with the measured features being noticeably broader than the predictions. However, even at higher powers the relative size of the peaks is accurately reproduced.

This model predicts that the transmission change should be directly proportional to the square of the electric field strength. This in turn is related to the power of the microwave field:

$$E_{\mathrm{MW}} = \delta\sqrt{P_{\mathrm{MW}}}, \tag{5.17}$$

where δ is a proportionality term taking into account the efficiency of the antennae

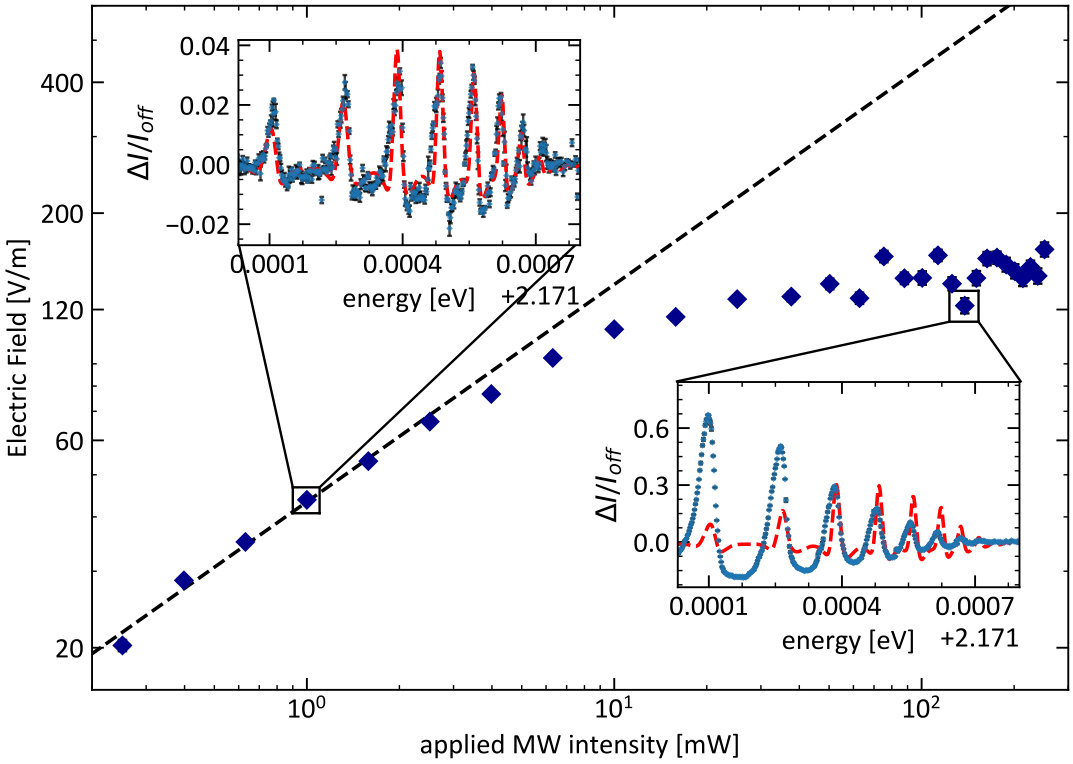

Figure 5.15: Scaling of extracted electric field strength with increasing microwave power. Insets show the fittings corresponding to the extracted powers at specific locations. For low microwave powers, the ratio of the features is in quantitative agreement with the model. However, this is not the case at high microwave powers where the extracted field no longer scales with input microwave power.

at that frequency. This aspect of the model can be verified by fitting the spectrum as a function of the microwave power and comparing the extracted field strength with the microwave power as shown in Fig. 5.15. Doing so yields a square root relationship, with δ taking the value of 43 $\mathrm{Vm}^{-1}/(\mathrm{mW})^{\frac{1}{2}}$. This is accurate for microwave powers up to 3 mW.

The discrepancy at higher microwave powers originates from the saturation of the response of the high principal quantum number states. Physically these originate in the lower excitonic population at a higher principle quantum number. That is to say, the modification of the spectrum is limited by the excitonic density. These saturation effects are not contained within the model, which predicts that the fractional change in intensity continues to grow with the increasing electric field. At the very highest powers, the shape of the spectrum is radically different to what the model predicts, notable with the largest response no longer being

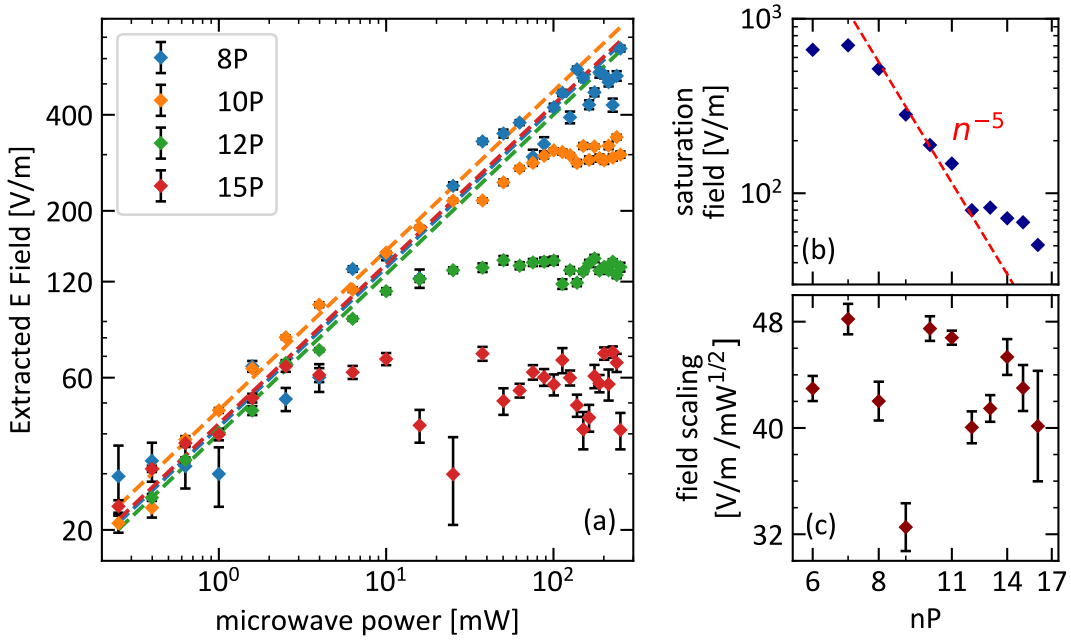

Figure 5.16: Piece-wise fitting of the microwave response using the $\chi^{(3)}$ model. (a) scaling of the extracted field for different nP states. The dashed lines show the square root dependence from low microwave powers. The vertical separation corresponds to a variation in δ. (b) the dashed red line indicates an n^{-5} scaling which fails at the very highest nP states. At lower microwave powers it is difficult to estimate exactly where the saturation sets in, if indeed it does at all. (c) the extracted field scaling is generally around the value extracted from the global fitting, with a reasonable drop at 9P. This corresponds to the model over-estimating the response in this region to the electronic field.

centred on 12P. In attempting to fit the model to these high microwave power spectra the the high nP states are disproportionately weighted leading to a lower predicted field. The onset of saturation occurs at lower microwave powers for higher nP states. Thus the range of powers for which the model is valid depends on which states we are considering. This can be characterised by separately fitting each state in turn, as shown in Fig. 5.16.

Doing so reveals several points of interest. The scaling of extracted field strength with input microwave power shown in Fig. 5.16(a) shows the same square root dependence for the different nP states. However, the actual field extracted by this procedure varies, as shown in Fig. 5.16(c). This implies that the matrix elements underpinning the model incorrectly predict the relative heights of the response at different nP states. The origin of this is in the deviation from the hydrogenic model, where these matrix elements were calculated based on that

assumption. Because the variation in field strength is only of the order of 10% this suggests that the model is largely quite robust. The square root dependency of the extracted field strength fails for high-power microwave fields. The point at which this occurs is shown in Fig. 5.16(b), which indicates this has an n^{-5} scaling law associated with it. Here, we attribute this scaling to the 5^{th}-order nonlinearity. The form of $\chi^{(5)}$ is given by:

$$\chi^{(5)} = \frac{|D|^2 d^1 d^2 d^3 d^4}{(\delta_{nP} - i\Gamma_{nP})\delta_1\delta_2\delta_3\delta_4}, \tag{5.18}$$

where $|D|^2$ is the oscillator strength of the nP state, d_i is the matrix transition element coupling between opposite parity states and δ_i is the resonance condition of that state given by $\delta_i = (\delta_{n'l'} - i\Gamma_{n'l'})$ for a detuning $\delta_{n'l'}$ which includes the energy of the relevant microwave fields. The scaling with n can be determined to leading order by considering the scaling of the individual components. The oscillator strength scales with n^{-3}, the coupling between states scales with n^2 and the resonance conditions scale with n^{-3} owing to the linewidths. This results in an overall scaling for $\chi^{(5)}$ scaling of n^{20}. This relates to the 5th-order nonlinear polarisation by $P^{(5)} = \chi^{(5)} E_{\text{L}} E_{\text{MW}}^4$. Here, we suppose that there is some critical polarisation $P_{\text{C}}^{(5)}$ which is required to impact the lower order nonlinearity. The electric field required to observe this is determined via $E_{\text{C}} = (P^{(5)}/\chi^{(5)} E_{\text{L}})^{\frac{1}{4}}$. This in turn would scale with n^{-5}, as shown in Fig. 5.16(b). For the very high n this scaling would alter as the n dependence on oscillator strength and linewidth would decrease. This will result in a weaker scaling with n at the very high nP states, as is observed in the experimental data.

5.3.2 Frequency Response

This section will explore the intensity of the red and blue sidebands as the microwave power is increased. The size of these sidebands can provide a measure for the change in phase of light owing to the Kerr effect, moreover, the fraction of the sideband to the carrier provides a direct measure of this in regions where the modulation is solely of the phase. Using the FPE, as illustrated in Fig. 5.6, the sidebands will be resolved to measure the Kerr effect over two regimes. The first is in a tight spacing between the 10P and 12P exciton to fully characterise the response over the 11P exciton. The second is on the blue detuned side of each P state exciton from 8P to 17P. This location was selected because the model

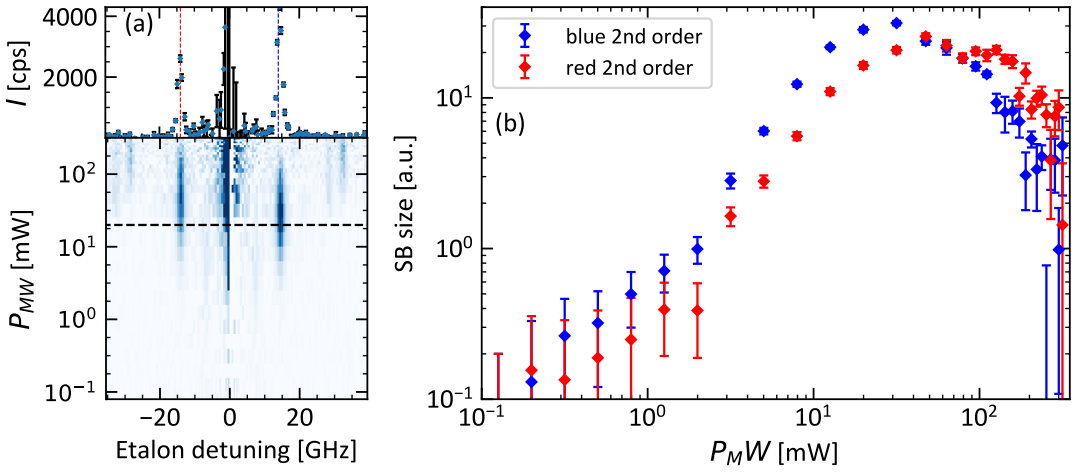

Figure 5.17: Characterisation of additional frequency components in the transmitted light. Left: As the microwave power is increased the 2nd-order sidebands appear before rolling over. Additionally, 4th-order sidebands can be seen at the highest powers. The feature at 0 GHz is an artefact of the subtraction of the on and off signals. Right: Appearance and subsequent rollover of 2nd-order sidebands. As the roll over the 4th-order sidebands appear.

predicts no amplitude modulation at these specific locations. The red detuned side was not used as the magnitude of the effect should be larger on the blue detuned side.

The experiments used in this section are logistically challenging owing to the large parameter space. This is largely due to having to scan over a range of microwave powers as the etalon is scanned. The microwave powers were selected to have two regimes of spacing. For low powers, they are logarithmically spaced. This is so the low power response can be well characterised. Then for high powers, they are linearly spaced. This spans a wide range of energy scales and ensured that there was sufficient data collected at the limit of this experiment. For each laser detuning the the laser wavelength was fixed. Then the spectral response was resolved by scanning the etalon over its FSR centred on the carrier frequency. At each etalon detuning the microwave powers were scanned over their entire range. This process is illustrated in Fig. 5.17. Notably, for higher microwave powers additional frequency components can be seen, these are 4th-order sidebands located 28 GHz away from the carrier frequency. These appear twice in mapping shown in Fig. 5.17(a) owing to the FSR of the etalon being 60 GHz. These features are notably weaker than the 2nd-order sidebands. This phenomenon will be explored further in the following chapter.

The procedure described above was carried out at multiple different locations on the excitonic spectrum. In particular, in two different regimes. The first was to resolve the frequency response of the sidebands on the blue-detuned side of each peak. This was at a location where the amplitude modulation was 0. This would enable an extraction of the Kerr coefficient in the following section. The blue side was chosen over the red side as we expected to see a larger Kerr coefficient on this side. The second regime was in a far narrower spacing over the 11P exciton to investigate the fine structure of the sidebands. 11P was selected as it displayed a significant microwave response while still maintaining a large oscillator strength. We will first discuss the red and blue sidebands in turn before comparing and contrasting the results between them.

The intensity of the red sideband across the excitonic spectrum is shown in Fig. 5.18. The experimental data has been fitted using the $\chi^{(3)}$ model for the sidebands laid out in Chapter 2. However, in that chapter $\chi^{(3)}$ was calculated based on a coherent sum of all possible transitions. That is to say, the complex amplitudes were all summed before taking the absolute value and squaring to obtain the intensity. Here, the theory curves are instead based on taking the absolute value squared before the summation. The reason for this is that there is a different phase associated with the different transitions, which will be unrelated to one another. By then assuming that this phase is randomly distributed the phases will on average cancel out instead of adding together. This results in an incoherent sum as opposed to a coherent one. The only free parameter in the fittings is a scaling factor which accounts for the sample thickness, re-absorption and laser intensity. This same procedure is applied for both the red and blue sidebands. Here, $\chi^{(3)}$ is evaluated at the laser detuning plus twice the microwave frequency ($\omega + 2\Omega$) and minus twice the microwave frequency ($\omega - 2\Omega$) for the red and blue sidebands respectively.

The data shown in Fig. 5.18 shows that the sideband grows with increasing nP at all microwave field strengths until 13/14P. Following this, the intensity rapidly falls to 0. This maxima and subsequent drop occur as a result of multiple phenomena interacting with one another. The first is that the matrix transition element coupling opposite parity states together grows with n^2, meaning that the resulting sideband intensity will be larger. However, this is modified by the resonance criteria for the microwave transition alongside the decreasing oscillator strength of the nP excitons. This behaviour is also seen in the theory curve plot-

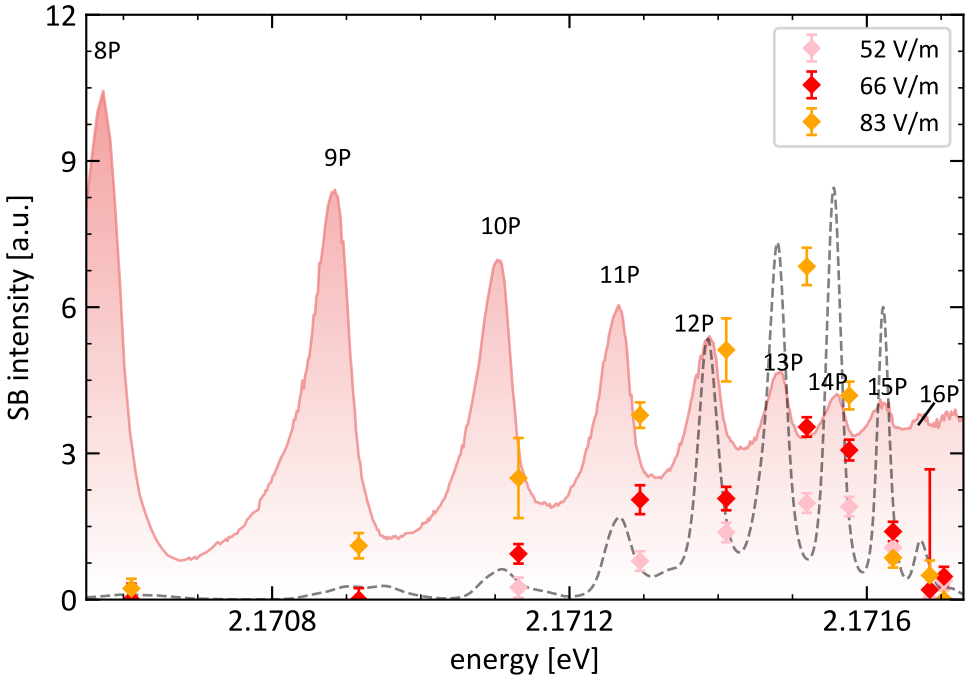

Figure 5.18: Variation in intensity for red detuned second-order sidebands. The dashed line shows the theoretical predictions based on summing transition amplitudes squared. This has been fitted to the lowest field strength data. An example transmission spectrum has been plotted in the background. Multiple field strengths have been shown to illustrate the scaling with microwave field strength at low powers.

ted alongside the experimental data. The theory curve has been fit to the lowest microwave field strength and provides good agreement. However, because the data has all been collected along the rising/falling edges of the predicted data it is perhaps unsurprising that such a fitting could be achieved. That being said, the shape of the minima and maxima of the theory curve does correspond to the same shape as that of the experimental data.

In the narrow spacing regime around 11P, as shown in Fig. 5.19 there is a clear structure to the sideband intensity. For all microwave field strengths, there are peaks in the response between nP states. This stands in contrast to the theoretical prediction which instead places these peaks on resonance with the nP states. It is however encouraging to see the same increasing trend with increasing nP in both the theory and experimental data. The origin of the discrepancy in the location of the peaks is uncertain. It may be due to the uncertainty in the location and width of the even parity states. It may also be due to the matrix transition

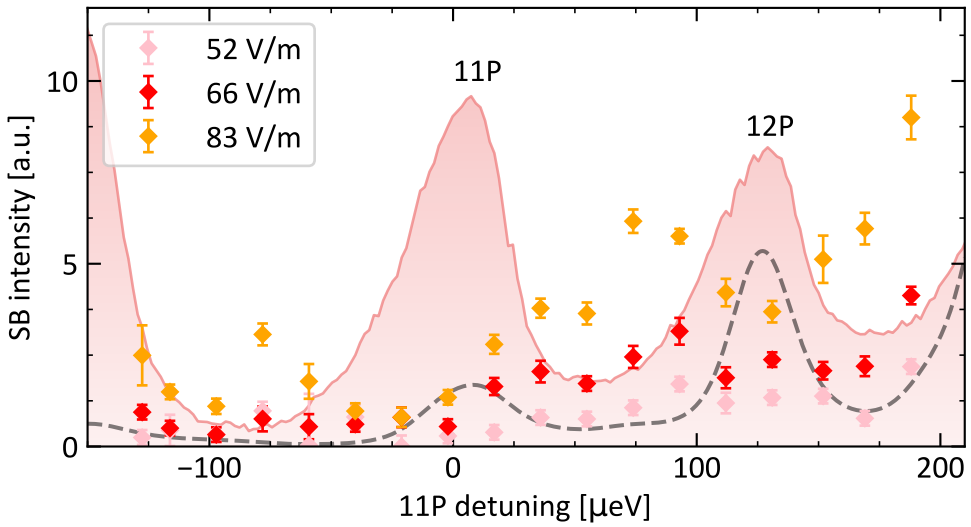

Figure 5.19: Variation in intensity for red detuned second-order sidebands around the 11P exciton. The dashed line shows the theoretical predictions based on summing transition amplitudes squared. The theory curve uses the same scaling parameter as used in Fig. 5.18.

elements not having the correct relative values. Combined, these effects can shift the location and sizes of features in the spectrum.

Similarly, the intensity of the blue detuned sidebands has also been measured across regimes of energies. This is presented in Fig. 5.20. Once again, the intensity of the sidebands initially increases with nP before rapidly dropping to 0 at all microwave field strengths. Unlike the red detuned sidebands, the peak in intensity occurs earlier around 12P instead of 13/14P. The origin of this is due to the states being coupled together in each process. For the red sidebands lower energy states are being coupled together as opposed to higher energy states for the blue sidebands. The higher states will have a stronger coupling but will lose oscillator strength earlier. As a result, the blue sidebands will decrease earlier. This will also be further impacted by the separation between opposite parity states which will be different for both the red and blue processes. As for the red sidebands the theory curve describes the change in intensity quite well, but once again the data has been taken on the rising/falling edges of the curves. It is also important to note that the scaling factor used for the blue data is approximately twice the size of that used for the red data. However, as the intensity of this process will depend on the electronic field strength raised to the fourth power this may reflect a change in field strength by 20%.

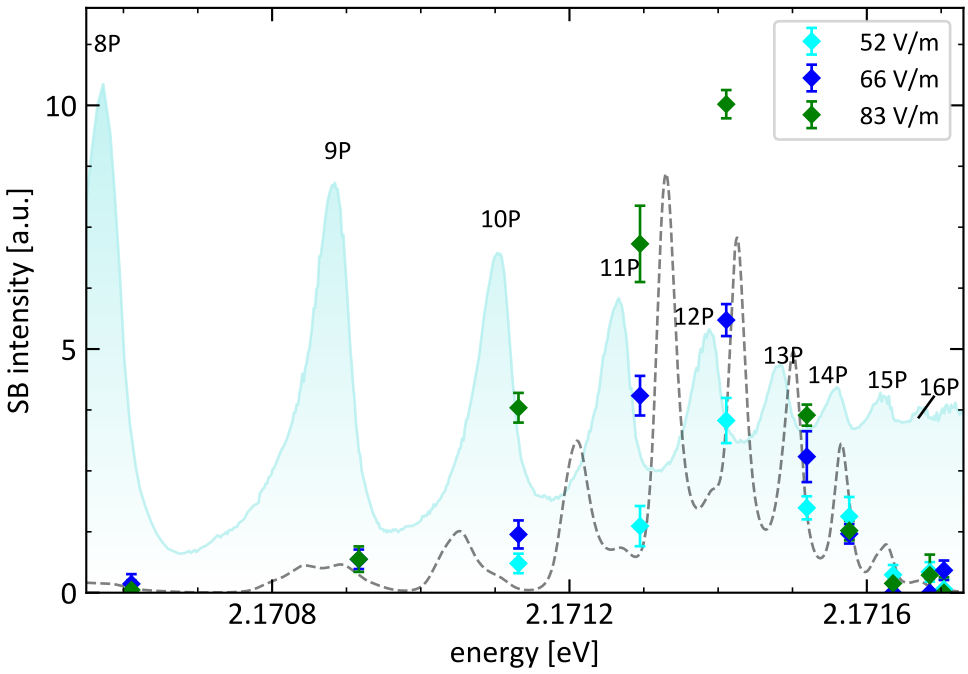

Figure 5.20: Variation in intensity for blue detuned second-order sidebands. The dashed line shows the theoretical predictions based on summing transition amplitudes squared. This is again based on the $\chi^{(3)}$ model used to generate the theory curve in Fig. 5.18. However, the scaling parameter for the theory used here is approximately twice as large as that used for the red sidebands. The same spectrum excitonic has been plotted in the background as before.

Again, the intensity of the blue detuned sidebands was measured in a narrow spacing regime across the 11P excitons. As with the red sidebands a distinctive structure can once again be seen. This time, the peaks are on the blue detuned side of the nP excitons. However, this time the theory predicts that the resonances would instead be between the excitonic states. As before, this discrepancy may be due to the matrix transition elements and the uncertainty in the location/width of the even parity states.

The structure of the intensity of the sidebands can be qualitatively reproduced using the $\chi^{(3)}$ model built up in the second chapter of this thesis. However, the fine structure around the 11P exciton does not appear to be well described by this model. Despite this, the model can place the relative size of features within the correct order of magnitude.

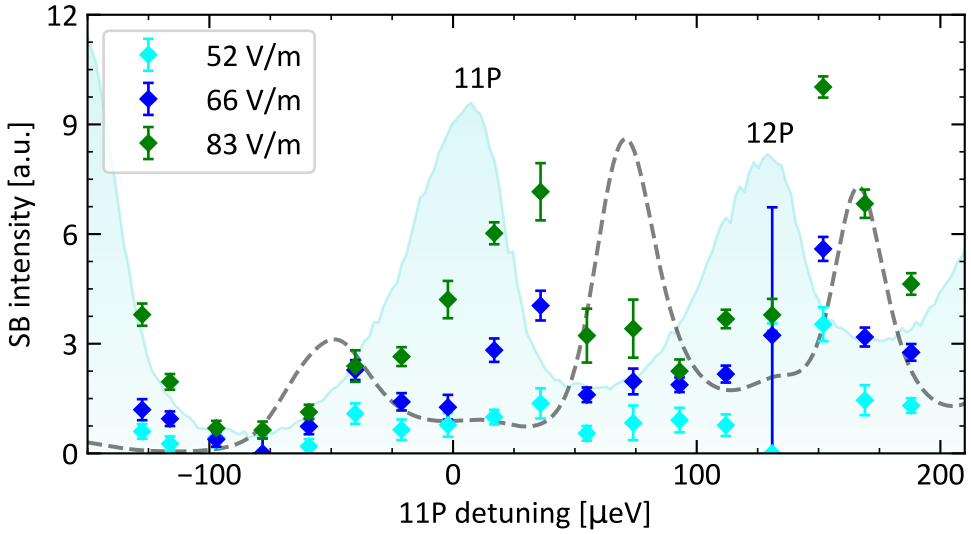

Figure 5.21: Variation in intensity for blue detuned second-order sidebands. As before, the theory line is shown by the dashed line.

5.3.3 Phase Modulation

In a purely phase-modulated system, there will be additional frequency components, manifesting as sidebands, appearing. If the modulation is owing to a Kerr effect these will be separated by an even integer multiple of the modulation frequency. The size of these sidebands is directly related to the change in phase ϕ. As discussed in Chapter 2 the ratio of the sideband to the carrier is described as:

$$\frac{I_{\mathrm{SB}}}{I_{\mathrm{Car}}} = \left|\frac{J_1(\phi)}{J_0(0)}\right|^2, \tag{5.19}$$

which enables the determination of the phase shift. For small modulations, this amounts to taking the square root of the carrier fraction. However, the experimental methods laid out in this chapter do not enable phase and amplitude modulation to be separately measured. As such it is not possible to determine if the sidebands are appearing as a result of amplitude or phase modulation. To work around this we used locations in the excitonic spectrum where the is no change in intensity due to the microwave field. At such locations, there is no amplitude modulation. Thus, a phase change can be extracted based on the ratio of the sideband intensity to the carrier intensity when the microwave field is not present. In turn, this enables a measurement of the Kerr coefficient. To experimentally measure the Kerr coefficient we extracted the change in phase as a function of increasing electronic field strength. This is achieved by measuring

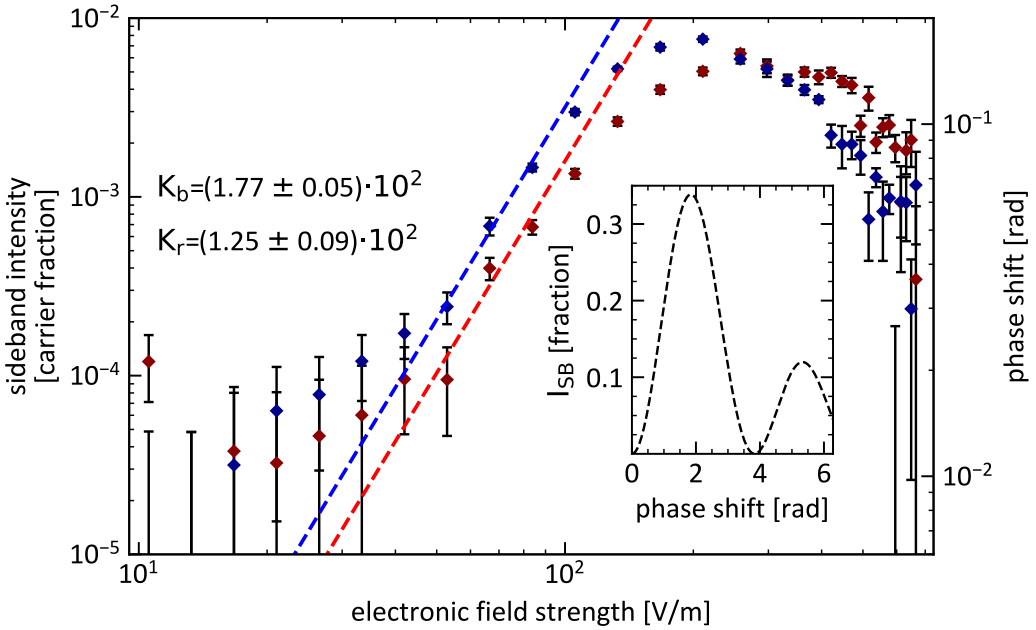

Figure 5.22: Kerr coefficient at 2.17128 eV, on the blue detuned side of 11P. Fractional size of blue and red sidebands compared to the carrier as a function of electronic field strength. Inset: the square of the second-order Bessel function which implies the shift in phase corresponding to the sideband fraction. Dashed lines show the quadratic fit of the phase change, which in turn corresponds to a Kerr coefficient. For the very highest microwave powers the nonlinearity saturates.

the relative height of the sideband to the carrier as illustrated in Fig. 5.22. By then comparing this ratio to eqn. 5.19 the phase change is determined. This analysis is only valid in the region where the sideband intensity is quadratic with the applied field strength. As the power is continued to increase this is no longer the case and the sideband rolls over. This effect is further discussed in the following chapter. From this extracted change in phase, $\Delta\phi$, the Kerr coefficient, K, is calculated using:

$$\Delta\phi = 2\pi K E^2 L, \tag{5.20}$$

where L is the length of the crystal, taken to be 100 µm, and E is the electronic field strength. This was evaluated at multiple points across the excitonic spectrum. The experimental procedure used for this was the same as described in the previous section. For clarity, the process of determining the Kerr coefficient at a point in the spectrum is as follows:

1. Measure the size of the 2$^{\text{nd}}$-order sidebands at different electronic field strengths.
2. Convert this into a change in phase using eqn. 5.19.
3. Fit this to eqn. 5.20 in the regime where the scaling is quadratic to extract a Kerr coefficient.

Using the blue detuned measurements made in the previous section, the Kerr coefficient was determined across the entire excitonic spectrum. The results for which are shown in Fig. 5.23. The predicted value for the Kerr coefficient is derived from the real part of $\chi^{(3)}$ evaluated on the carrier:

$$\Delta\phi = k\,\mathrm{Re}(\chi^{(3)}), \tag{5.21}$$

where k is the associated wave vector. The method laid out of using the relative size of the sidebands is not able to determine the sign of the phase change. As a result, we compare the absolute size of the predicted Kerr coefficient to the data. The Kerr coefficient calculated from the red and blue sidebands both increase with nP until around 13P. Here the extracted Kerr coefficient drops. This is in part due to the difficulty in accurately extracting the Kerr coefficient at the highest nP states. The theory predicted value Kerr coefficient largely scales with the extracted values. This is once again due to the values having been extracted on the falling edges of the theory curves. But of key importance is the same envelope function describing both sets of data.

To further investigate the nature of this effect, the power scaling with n has been investigated. The results of this are shown in Fig. 5.24. Here, the blue Kerr coefficient scales with $n^{6.5}$, compared to the weaker n^5 for the red coefficient. These are comparable to the n^7 scaling of polarisability of Rydberg states. The expected dependence can be derived by considering the functional form of $\chi^{(3)}$. This is given by:

$$\chi^{(3)} = \frac{|D|^2 d_1 d_2}{(\delta_{\text{nP}} - i\Gamma_{\text{nP}})\delta_1\delta_2}, \tag{5.22}$$

where $|D|^2$ is the oscillator strength of the nP exciton and scales with n^{-3}, d_i is the coupling between opposite parity states and scales with n^2. The denominator δ_i is the resonance condition of the microwave transitions and scales as the linewidth with n^{-3}. Taken together this would predict a scaling of n^{10}. This is higher than the measured power laws for either detuning. However, for high n the oscillator strength for the nP excitons falls with n^{-12}, which would result in a considerably weaker scaling of simple n^1. As the data has been collected on the side of a peak

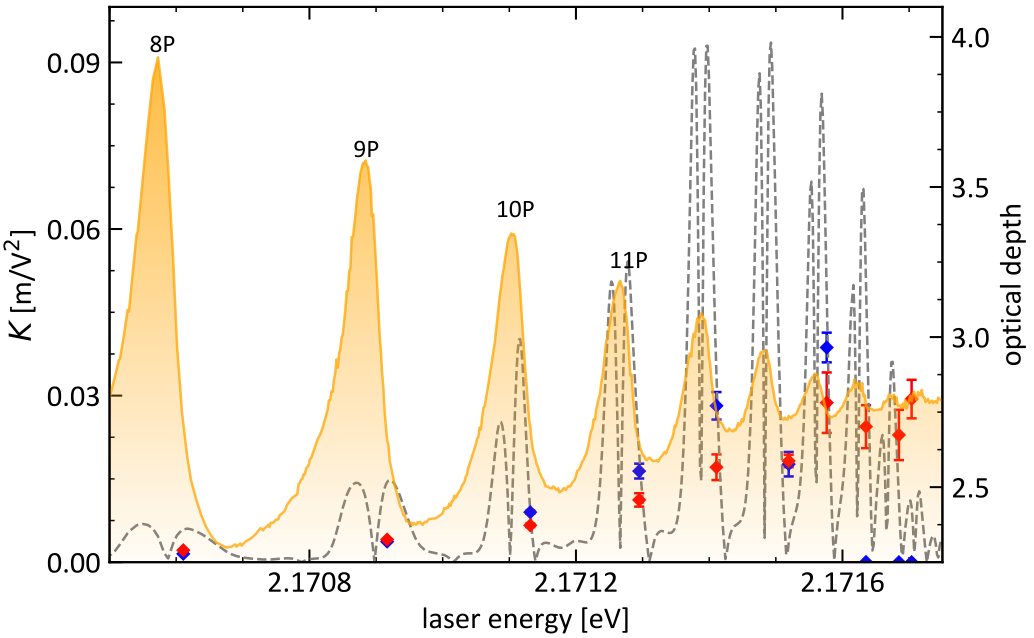

Figure 5.23: Extracted Kerr coefficient over the excitonic spectrum for the red and blue sidebands. The grey line shows the predicted value from the model. At nearly every detuning the magnitude of the effect from the model matches that extracted from the experiment.

it may result in a much weaker scaling. The difference in scaling between the red and blue extracted measurement originates in the approximation that the value of $\chi^{(3)}$ is independent of frequency.

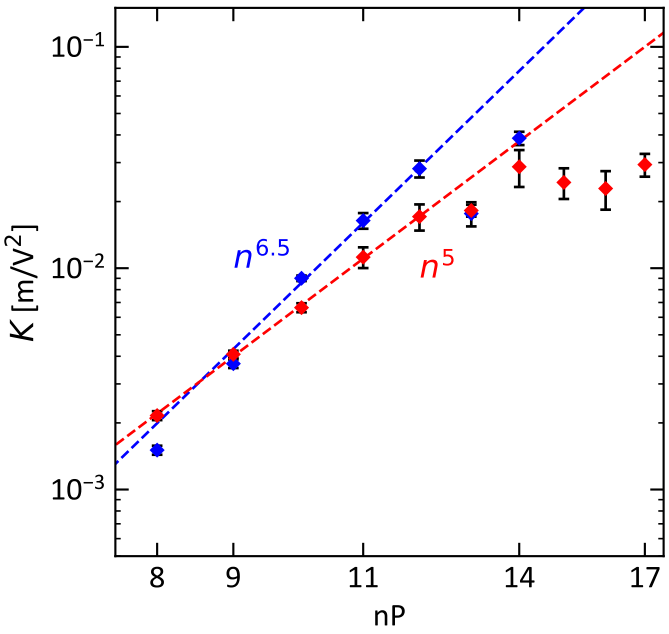

Figure 5.24: Scaling with principal quantum number of the extracted Kerr coefficient from the red and blue detuned sidebands. The dashed line shows the extracted scaling for the red and blue lines respectively.

5.4 Conclusions

In conclusion, the impact of an external microwave field on the transmission spectrum of cuprous oxide has been examined using an atomic physics-based model of $\chi^{(3)}$. This was carried out using a modified experimental setup laid out in Chapter 3 of [55]. This encompassed the change in absorption, the change in the polarisation state of transmitted light and the generation of additional frequency components as a result of the microwave field.

By resolving the polarisation state of the transmission it was determined that the microwave field did not affect the polarisation state of this transmitted light. Furthermore, the polarisation state of the sidebands was the same as that of the transmitted light. This implies that the elements of the $\chi^{(3)}$ tensor are related in the following way: $\chi_{\mathrm{xxxx}} = \chi_{\mathrm{xxyy}} - 4\chi_{\mathrm{xyyx}}$.

The model for $\chi^{(3)}$ was able to provide quantitative agreement to the measured change in absorption. This was only valid in the low microwave field strength regime. The deviations from this model occurred at a lower microwave field strength for higher nP states. The n^{-5} dependence on this critical field was attributed to

the higher order $\chi^{(5)}$ nonlinearity becoming significant. However, the $\chi^{(3)}$ was less effective at describing the additional frequency components. It was not able to provide quantitative agreement in this regime, instead only being able to describe the correct relative height between features and not the corresponding lineshape. This disagreement is attributed to the greater importance that the state energy and positions play for these components compared to the carrier frequency.

Finally, by measuring the dependence of the size of the 2^{nd}-order sidebands as microwave field strength is increased a measurement of the Kerr coefficient was made. This was carried out at regions where the change in absorption was 0. This meant that any additional frequency components were only a result of the modulation of the phase of transmitted light. The extracted Kerr coefficient was of the order of 10^{-2} mV^{-2}, 10 orders of magnitude larger than that of nitrobenzene. This extracted value is in good agreement with the theory value predicted by the $\chi^{(3)}$ model. The scaling of this value with the principle quantum number was found to be $n^{6.5}$ for the blue extracted value or n^5 for the red. This is comparable to the leading order scaling of $\chi^{(3)}$, with the discrepancy highlighting the approximations made to make this measurement of the Kerr coefficient.

The measurement of such a large Kerr nonlinearity and the success of the $\chi^{(3)}$ model further cements cuprous oxide as a viable platform for Rydberg physics in the solid state. However, a range of interesting physics is still to be explored in the form of higher-order nonlinearities and the breaking down of this model.

Chapter 6

Strong Driving Regime

The response of a medium to an external electric field is determined by the motion of the charge carriers within it. For suitably weak fields the charge carriers are only displaced by a small amount. As a result, the potentials describing the motion of these charges can be treated as parabolic [61]. This describes, the regime of linear optics, where the polarisation induced with a medium is at the same frequency as the driving field. As a result of this the polarisation, $\tilde{\mathbf{P}}$, is related to the external electronic field, $\tilde{\mathbf{E}}$, by:

$$\tilde{\mathbf{P}} = \chi \tilde{\mathbf{E}}, \tag{6.1}$$

where χ is the electronic susceptibility of the material. In Chapter 2 a quantum mechanical approach based on line widths and energy levels was laid out which can calculate the numerical value of χ for cuprous oxide. This enables a theoretical description of the spectra obtained in Chapter 4. The primary focus of this thesis however has been the change to the excitonic spectrum in the presence of a strong microwave field. In such a regime the displacement of charge carriers is no longer small, and their potentials can no longer be treated as harmonic. This requires that the polarization is now described by a power series in the electronic field:

$$\tilde{\mathbf{P}} = \chi^{(1)}\tilde{\mathbf{E}} + \chi^{(2)}\tilde{\mathbf{E}}\tilde{\mathbf{E}} + \chi^{(3)}\tilde{\mathbf{E}}\tilde{\mathbf{E}}\tilde{\mathbf{E}} + \dots , \tag{6.2}$$

where $\chi^{(n)}$ is the n^{th} nth-order nonlinear susceptibility. Here, $\chi^{(1)}$ is the linear susceptibility. As cuprous oxide is a centrosymmetric crystal, all even-order nonlinearities go to 0. As a result, even order terms are neglected and the lowest order nonlinearity is the $\chi^{(3)}$ term. As $\chi^{(1)}$ the numerical value of $\chi^{(3)}$ can be calculated. Doing so enabled quantitative predictions for the change in the transmission of

cuprous oxide in the presence of a microwave field. This also enabled the extraction of an enormous Kerr coefficient, many orders of magnitude larger than that seen in conventional Kerr media. However, as with the linear susceptibility model this $\chi^{(3)}$ model too will break down in sufficiently strong fields. This leads to the $\chi^{(5)}$ term becoming significant. As before, this will introduce additional frequency components to the transmitted light and further modify the transmission. Of course, this trend of requiring higher-order terms will only continue as the microwave power is further increased.

To model the increasing complexity of the microwave-induced nonlinearities in cuprous oxide a more robust, physics-based model is required. Such a model is being built up by Alistair Brewin in Durham, in collaboration with the work presented in this thesis. The model used here is a Floquet theorem-based approach, in which excitons are modelled as spinless hydrogen. This will be expanded upon within the chapter. The advantage of such a model is that it enables a more detailed understanding of the nature of the excitonic states to be built up. An additional benefit of this approach is that higher-order nonlinearities are built into the model, and so do not need to be separately incorporated. While the inner workings of this model are beyond the scope of this thesis, some of the initial results of it will be compared and contrasted with experimental data in this chapter.

This chapter serves partially as an outlook, to report on higher-order nonlinearities and to make some of the initial comparisons to a new theoretical tool. Much of the work presented here is more recent, and as such is less well understood. Regardless, this chapter stands to illustrate the limitations of the models developed so far and to explore a new avenue to understanding the optical properties of cuprous oxide. All of the data presented in this chapter was collected alongside the data shown in the previous chapter. The key difference here is that the focus of the analysis is on the higher-order effects.

6.1 Higher Order Nonlinearities

The focus of the previous chapter was on describing the modifications to the transmission of cuprous oxide in the low-field strength regime. Here, the dominant contribution to the nonlinear response is the $\chi^{(3)}$ term. One of the key

characteristics of this nonlinearity is the inclusion of additional frequency components to the transmitted light. This manifests as sidebands separated from the laser frequency by integer multiples of the microwave frequency. In the case of $\chi^{(3)}$ these sidebands are separated by twice the microwave frequency. Similarly, for the next lowest order nonlinearity, $\chi^{(5)}$, the sidebands will be separated from the carrier by four times the microwave frequency. This section will explore the power dependence of the 4^{th}-order sidebands. Alongside this, it will examine the field strength required for these higher-order sidebands to appear.

The setup and experimental procedure used to collect this data are laid out in the previous chapter. The typical spectrum of the transmission from such an experiment is shown in Fig. 6.1(a). As with the 2^{nd} order sidebands the red and blue sidebands appear on the red and blue detuned side of the carrier. Only this time they are separated by 28 GHz as opposed to 14 GHz. A notable change is that the sidebands also appear 32 GHz away from the carrier. These additional features are copies arising from the 60 GHz free spectral range (FSR) of the etalon. They are instead 28 GHz detuned from the carrier feature that is 60 GHz away from the central carrier feature.

It is immediately clear that the magnitude of the 4^{th}-order sidebands is much smaller than that of the 2^{nd}-order sidebands. The reason for this is in the resonance condition required for their generation. This can be illustrated by considering the resonance condition for the 2^{nd} order sidebands. Here, there are three conditions which need to be simultaneously met. The first is that the laser is resonant with an nP state. The second is that this nP state is detuned by a microwave frequency to a neighbouring nS/D state. The third and final condition is that this nS/D state is separated from a higher-lying n'P state by the microwave frequency again. This condition is never perfectly met, instead being allowed by the large widths of the excitonic states. In the case of the 5^{th}-order nonlinearities, an additional two criteria are added. The n'P state must be separated from another n'S/D state by the microwave frequency, which must in turn be separated from a final n"P state by another microwave frequency. The result of this additional step is that the 5^{th} order process is essentially "less" resonant than the 3^{rd} order process.

The dependence on microwave field strength is shown in Fig. 6.1(b). Similarly to the results for the 2^{nd} order sidebands, the 4^{th} order sidebands scale with the V^4, as one would expect of a 5^{th} order process. However, this scaling is only valid for

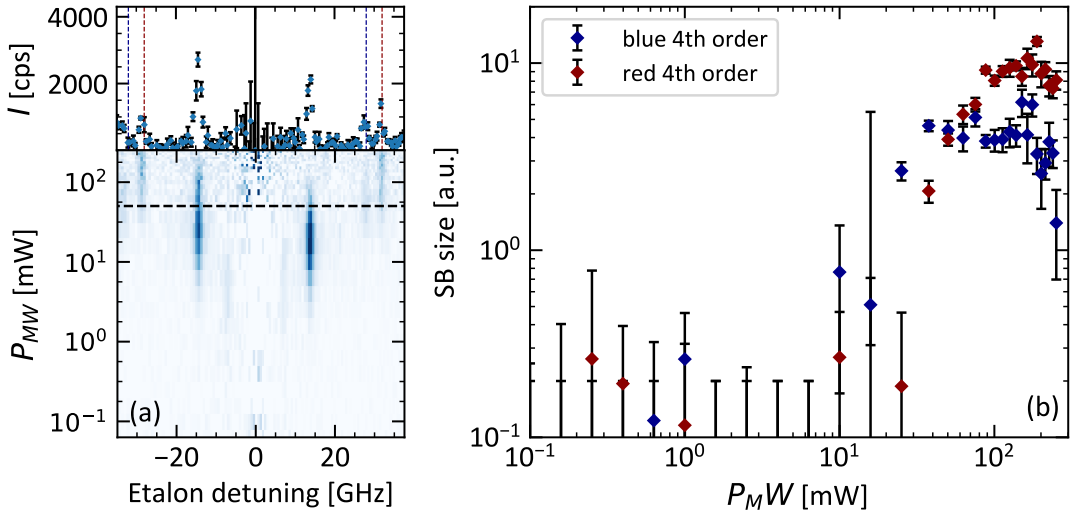

Figure 6.1: Power dependence for the 4$^{\text{th}}$ order sidebands. (a) frequency resolved transmission at 1142.04 nm, on the blue detuned side of the 11P exciton. As the microwave power is increased first 2$^{\text{nd}}$-order sidebands appear before weaker 4$^{\text{th}}$-order sidebands at very high microwave powers. The dashed line is the power at which the spectrum above is plotted. (b) power dependence of the 4$^{\text{th}}$-order sidebands. As with the 2$^{\text{nd}}$-order sidebands they are only resolvable in sufficiently strong fields.

a small range of powers. Above this range, the nonlinearity is either saturating, or even higher-order nonlinearities are starting to become important.

A higher electronic field strength is required to produce the 4$^{\text{th}}$-order sidebands as compared to their 2$^{\text{nd}}$-order counterparts. The required electronic field strength was investigated across the excitonic spectrum by utilizing a threshold intensity. The value for this was selected to be 0.5 a.u. This value was chosen because it was above the noise floor of the sideband intensities at all wavelengths, and it was well below the intensities for which the nonlinearity appears to saturate. This field strength was identified by fitting the sideband intensity using a 6$^{\text{th}}$-order polynomial in the electronic field strength. This fitting is phenomenological and offers a simple procedure to identify the threshold field strength. The results of this are shown in Fig. 6.2. Clearly, for both the red and blue sidebands, the scaling is consistent with approximately n^{-3}.

The expected scaling for the visibility of the sidebands comes from the intensity resulting from a 5$^{\text{th}}$-order nonlinearity. This is given by:

$$I_5 = |\chi^{(5)}|^2 E^8, \tag{6.3}$$

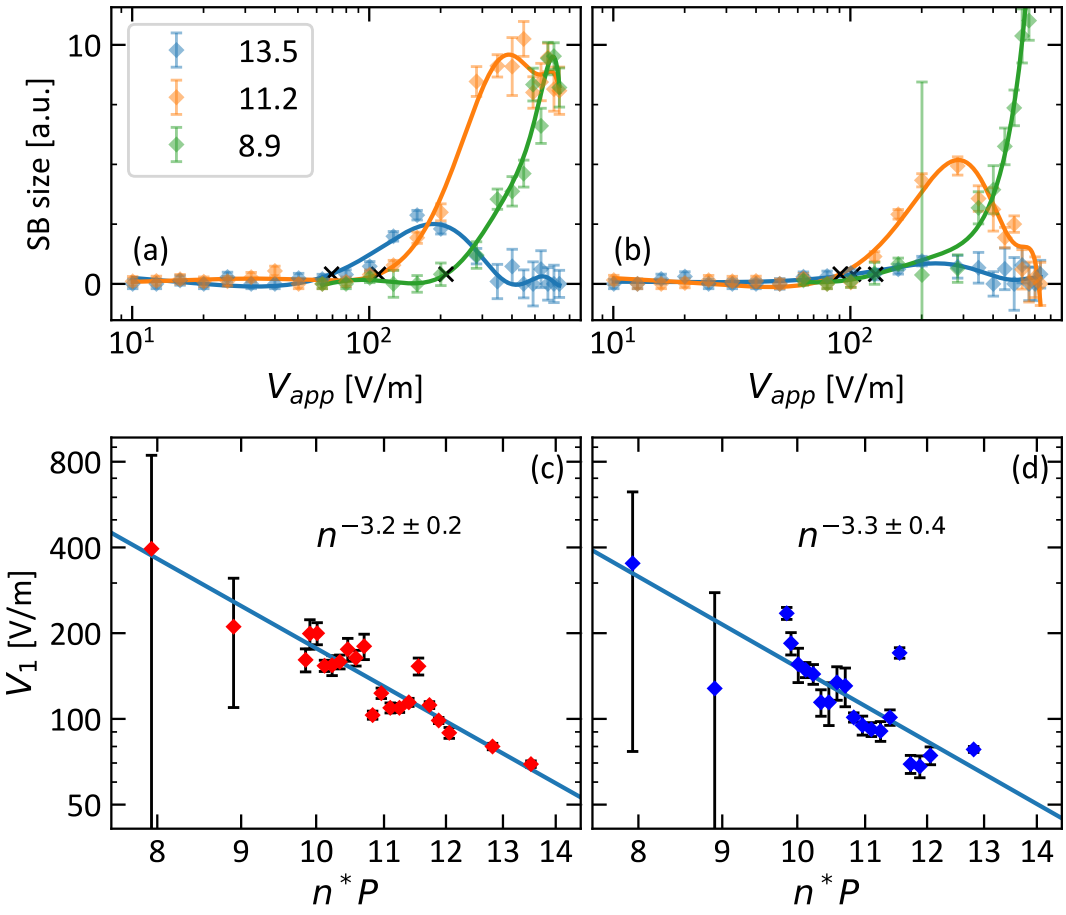

Figure 6.2: Detect-ability of the 4$^{\text{th}}$ order sidebands. (a) and (b) intensity of the 4$^{\text{th}}$-order red and blue sidebands respectively. The power dependence is fit using a 6$^{\text{th}}$-order polynomial function, the black x indicates the intensity is above the threshold 0.5 at that microwave field strength. (c) and (d) detect-ability of the red and blue 4$^{\text{th}}$ order sidebands respectively. Both red and blue are consistent with an n^{-3} dependence.

We can extract a scaling by suggesting that there is some I_5^0 for which the intensity can be detected. To obtain an n dependence we must obtain the n dependence of $\chi^{(5)}$. The form for $\chi^{(5)}$ is given by:

$$\chi^{(5)} = \frac{|D|^2 d^1 d^2 d^3 d^4}{(\delta_{\text{nP}} - i\Gamma_{\text{nP}})\delta_1\delta_2\delta_3\delta_4}, \tag{6.4}$$

where D is the matrix transition element from the valance band to the nP state, d^n a transition between S/D and P states (as with $\chi^{(3)}$) and δ_i is the resonance condition for the nth transition. For the numerator, D ordinarily scales with n^{-3}. However, spectroscopy of the high n states carried out in Chapter 4 revealed that this instead scales with n^{-12} above $n = 10$. The matrix transition elements

d^i, scale with n^2 meaning the scaling of the entire numerator is with n^{-4}. The scaling with n from the denominator is found by considering the scaling with line width. This scales with n^{-3} and results in an over-scaling of n^{-15}. Thus the overall scaling is n^{-11}. Placing this into eqn 6.3 and rearranging such that E is the subject reveals that the field should scale with $n^{\frac{11}{4}}$. This is in reasonable agreement with the extracted parameters shown in Fig. 6.2.

However, much like the oscillator strengths the widths deviate from the expected n dependence at high principal quantum numbers. Instead, they fall much slower. This would result in lowering the expected n dependence for higher nP states to be lower than $n^{\frac{11}{4}}$. However, this effect is only really appreciable for the very highest nP states. As a result, this dependence with n is only in reasonable agreement with the predicted value.

6.2 Saturation of Microwave Modulation

The previous chapter made use of a $\chi^{(3)}$ based model to quantitatively predict the change in the excitonic spectrum due to the application of a microwave field. This model was valid for relatively low microwave field strengths. Beyond this, higher-order nonlinearities become significant and the nonlinear response of the media can saturate.

Utilizing the experimental data collected throughout the previous chapter this breaking down of the $\chi^{(3)}$ model can be seen in Fig. 6.3. Several features in this figure are immediately striking. Perhaps the most obvious is that the most significant change in the spectrum occurs between 9P and 11P, and corresponds to a decrease in the optical depth. This is the suppression of the P character of these states leading to an increase in transmission. However, this decrease is largely focused on the red detuned side of each exciton. On the blue detuned side, we instead see an increase in the transmission. This increase corresponds to the mixing of the P-like character into the S states. It is interesting to note that the onset of the microwave response occurs at lower and lower microwave field strengths for increasing n. This can be explained by the increasing dipole moment of higher-lying states. But this effect competes with the separation between states, for the very highest n states the resonance condition is less well fulfilled and the oscillator strength begins to drop away more significantly. As a

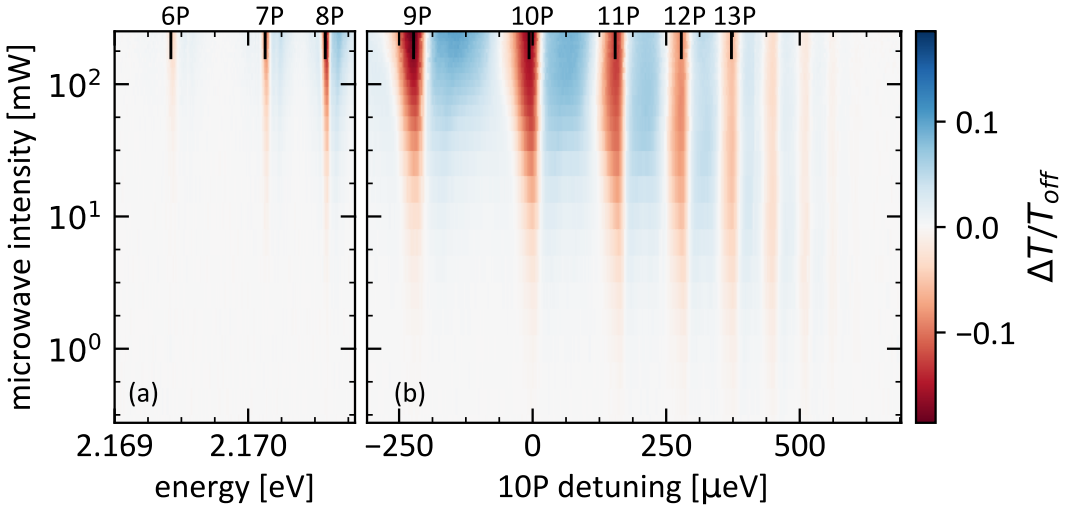

Figure 6.3: Impact of the microwave field on the transmission spectrum. As before we see a decrease in optical depth on resonance with nP states and an increase off resonance. There is a larger fractional decrease. The effect saturates at lower microwave powers for increasing nP, with the highest states appearing to saturate nearly immediately.

result, the size of the effect begins to drop. The next feature which attracts the eye is the onset of saturation at each state. For sufficiently large powers the change in the spectrum begins to slow down. This is most clear for the very highest states, further illustrated in Fig. 6.4. Here it is clear that the 16 and 17P states saturate nearly immediately, while the 14P and 15P states do not saturate at such low powers. For all nP states there is an asymmetry in the response within the low power regime. This can be seen as a preferential spreading out of the red regions. This is likely a result of the asymmetric nature of the excitons themselves. For the highest powers, the shape of the response begins to be determined by the spectrum in the absence of microwaves. In terms of spectra, this originates in the highest-lying states being completely washed out by the microwaves. This can be thought of as a strong mixing of the S and P-like character resulting in a flat response.

The impact of higher-order nonlinearities occurs at lower microwave powers for higher-lying excitonic states. This is a result of the increasing polarisability of such states alongside a smaller coupling strength. The result of the smaller coupling strength is a lower excitonic population. This means that saturation terms can kick in much faster.

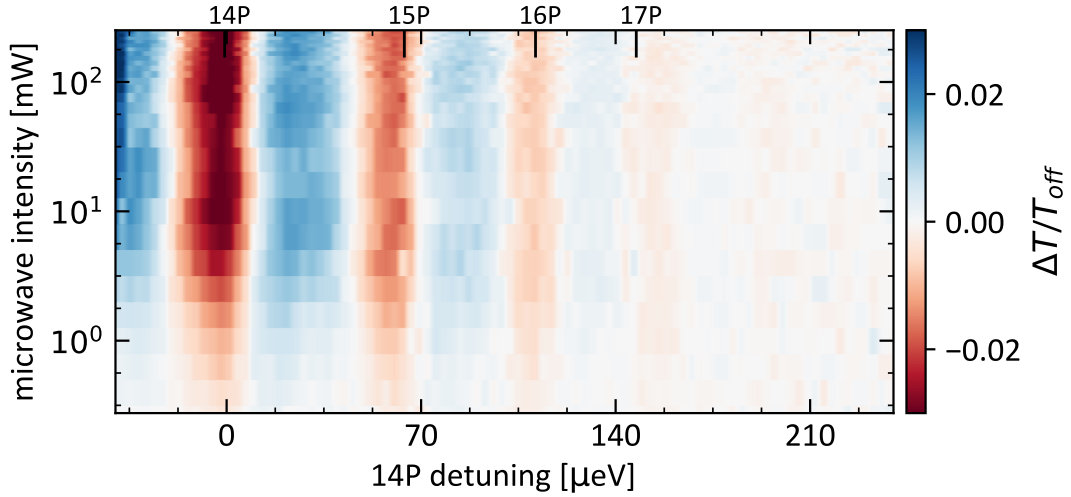

Figure 6.4: Change in the transmission of high nP states. The onset of saturation can be seen for low microwave intensity for 14P and 15P but is far less clear for 16P. There is a weak response in the region of 17P, but beyond this it is unclear.

6.3 Change to Excitonic States

A characteristic of atomic systems in the presence of external electric fields is the Stark effect. This results in the moving, broadening, and eventual splitting of states. This effect has so far not been explored in this thesis, instead with the focus being on the overall change in absorption and refractive index through an electronic susceptibility model. As such, this section will focus on characterizing the change to the excitonic states owing to a microwave field on increasing field strength.

Much like the first section of this chapter, the data for this section was collected by scanning the laser over the entire excitonic spectrum. Simultaneously, the microwave field strength was varied over a wide range. An overview of the change in excitonic states resulting from this is shown in Fig. 6.5. Broadly speaking, states become broader and less tall as a result of the microwave field. This effect is stronger in higher n states, where for sufficiently strong fields it is no longer possible to resolve them. An additional impact of the microwave field is an increase in the absorption between states. This is seen by looking at the gaps between states, where subsequent spectra overlap more at higher microwave powers.

For states above 9P, there is also a clear shift in the energy levels of the states.

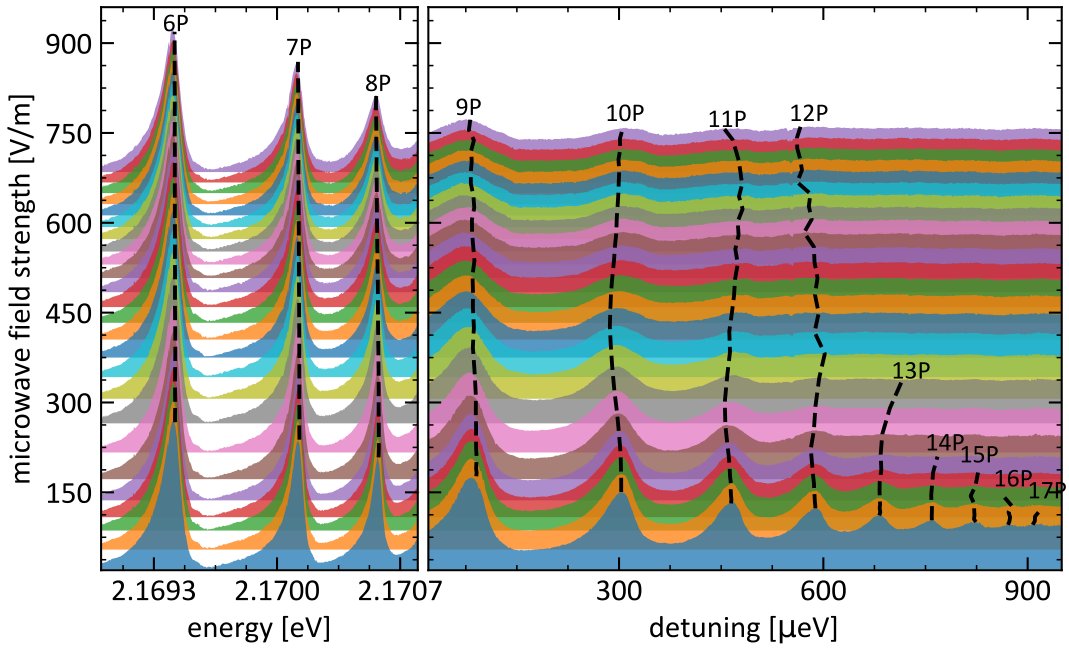

Figure 6.5: Excitonic spectra in microwave fields of increasing strength. Spectra are vertically separated according to the applied field strength. Dotted lines corresponding to the peak position of states have been added for clarity. This does not always trace the peak in the absorption as the states are asymmetric.

This only becomes more pronounced with 13P appearing to shift by more than its linewidth before becoming unresolvable. We observed similar effects in excitonic states with increased microwave field strengths. This is shown in Fig. 6.5. Here the transmission change can be seen between subsequent field strengths. Moreover, the higher-lying states dramatically change in appearance. They become broader and even begin to shift in energy levels. For the very highest lying states they become completely washed out and cease to be resolvable. To further study the change in excitonic character the spectrum was fitted using the same procedure laid out in chapter 4. Here, an asymmetric Lorentzian is fit to each excitonic peak separately. The initial conditions for each peak are acquired by fitting the data where no microwave field is present. An example of this process is illustrated in Fig. 6.6 for the 11P exciton. Here the shift in location of the state and the broadening of the estate are clearly shown. It is worth noting that for increasing microwave field strengths the state becomes increasingly asymmetric. A significant result of this is that the extract peak position begins to deviate from the peak of the absorption feature.

This same procedure was then applied to all excitonic states in turn. The results

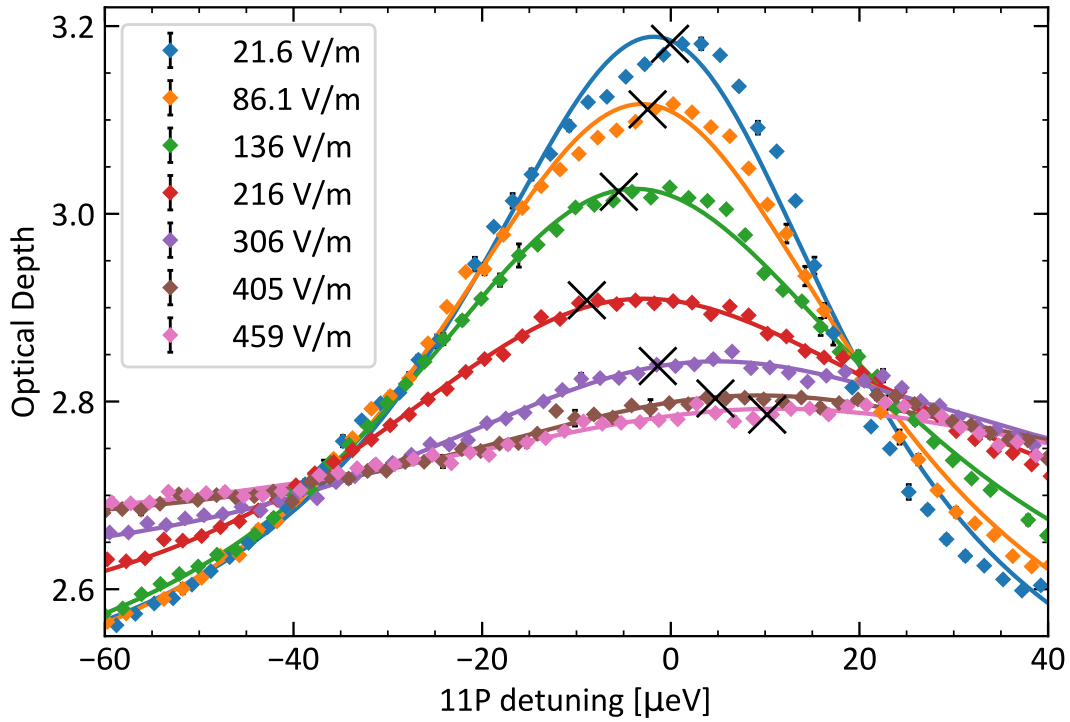

Figure 6.6: Comparison between experimental data and fittings around the 11P exciton. The black "x" marks indicate the extracted peak position from the asymmetric Lorentzian lineshape.

of this are shown in Fig. 6.7. Here, trends in the extracted parameters have been fitted using a 5^{th}-order polynomial. The purpose of this is to illustrate trends in the extracted parameters and to identify trends in the data. As seen in Fig. 6.5 the oscillator strengths, shown in Fig. 6.7(a), drop with increasing microwave field for virtually all states, with the sole exception of the 8P state. Moreover, the drop in oscillator strength occurs more sharply and at a lower microwave field for increasing n. The fitted curves describing the extracted parameters all appear to be from the same "family" of curves, they do not overlap much and appear to have similar behaviours with increasing n. Moreover, the suppression of states only increases with increasing n. For 9P the state is only reduced by a factor of around 0.3, whereas the 14P state is nearly totally suppressed by the microwave field.

Similarly, the line trend in energy levels, shown in Fig. 6.7(b), appears as a family of curves. This time they are distinguished by first shifting to lower energies before "swinging back" and shifting states to higher energies. The dependence on n for this turning point is shown in Fig. 6.7(d) and is consistent with an n^{-7}

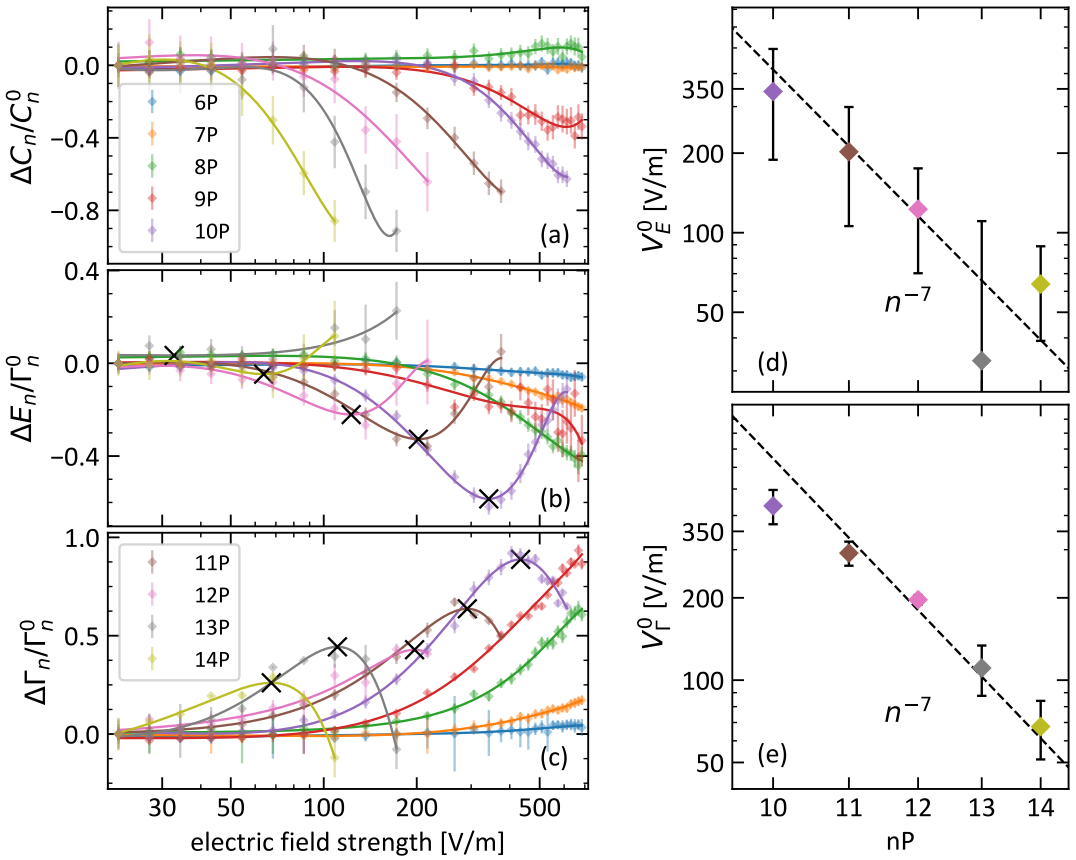

Figure 6.7: Change to excitonic states as the microwave field strength is increased. Throughout, fittings to extracted parameters are carried out using a 5^{th}-order polynomial. (a) Fractional change in the oscillator strength. Only the 8P state shows an increase in microwave field strength. (b) fractional shift in energy level. States all shift to lower energy. At a characteristic field strength V_E^0 some states swing back to higher energies. (c) fractional change in line width. Similarly to energy levels states initially broaden before swinging back at a characteristic field strength V_Γ^0. (d) n dependence of V_E^0 is consistent with an n^{-7} dependence. (e) similar to the n dependence for V_E^0, the n dependence of V_Γ^0 is consistent with an n^{-7} dependence.

dependence. This is the scaling for polarisability in atomic systems. Here, it is the 10P exciton which is shifted by the most.

Finally, the widths, shown in Fig. 6.7(c) behave oppositely to the energy levels. At first, the states become broader, before then swinging back t become narrower in increasing microwave fields. As before, the trend in the location of this turning point scales with n^{-7}. Unlike the energy level, it is the 9P state that is most impacted by the change in widths. This fitting can show a great deal of interesting

physics for the state which have been investigated. However, it is challenging to ensure that the fitting is accurate in all cases. For the high-lying states, it is difficult to resolve states from the phonon background, which is only made worse in a strong microwave field. Moreover, the analysis carried out in Fig. 6.7 does not take into account the asymmetry of the fitting function. This may have resulted in states being overfitted. The n^{-7} dependence on the turning point suggests that it is the increasing polarisability of the states that are leading to the earlier turning points. However, the limited number of data points makes any conclusions challenging to draw. The turning points present in the widths and energy trends suggest that there are competing effects present in the material. Which become significant in different energy regimes and have the opposite effect on the respective states.

Excitonic states are becoming highly coupled in the strong driving regime. To account for this we seek to utilize the Floquet model which can take these effects into account.

6.3.1 Comparison to the Floquet Model

We now turn to a theoretical approach to model this phenomenon. As described in the introduction this model is built by Alistair Brewin and is based on treating excitons as spinless hydrogen. Here, the primary appeal of the Floquet theory is in its ability to take additional frequency components into account [170; 171]. Within the rotating wave approximation, we only consider frequencies which are resonant with the atomic system in question. The Floquet theory enables an extension of this theory by essentially rotating the system at different frequencies to extract information regarding those frequency components [172]. In practice, this allows for analysis of the nonlinear electronic fields by examining the components of the field which are rotating at $\omega + n\Omega$, where laser frequency ω and microwave frequency Ω. As a result, we can take the microwave field into account much better than through a simple nonlinear susceptibility approach, and easily extend this Floquet model to higher-order nonlinearities.

As in the experimental data, excitonic spectra are obtained over the entire spectrum for different microwave field strengths. The results of this are shown in Fig. 6.8. Qualitatively the change observed in the spectrum below is similar to that shown above. The notable difference is that states begin to split under

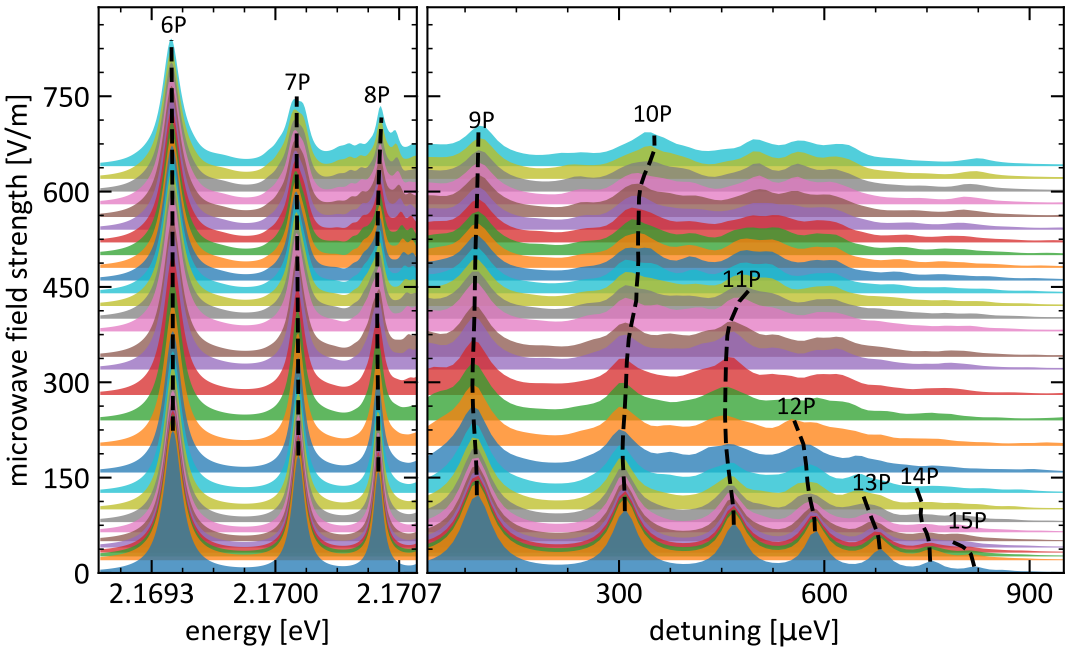

Figure 6.8: Variation in predicted excitonic spectrum with increasing microwave field strength. As before, vertical separation indicates a higher microwave field strength. Dashed lines indicate the extracted peak location while peaks are resolvable.

increasing microwave powers. This corresponds to Autler-Townes splitting and is not present in the experimental data. However, this may be what is being captured by the broad effects at higher-lying states.

Alongside the appearance of additional states similar behavior in the broadening and lowering of peaks can be seen. This is again particularly clear by looking between the excitonic states. The change in state position is immediately far more dramatic and the shifts can be greater than the linewidth of the initial state. Again the change in position of and widths of these states has been investigated. However, this model is based on symmetric Lorentzian line shapes, and without a background term. This does affect the numerical values of the following analysis, so we see to compare orders of magnitude and overarching trends, the results of this are shown in Fig. 6.9.

The extracted fitting parameters from the experimental and Floquet model data are quite different from one another. As shown in Fig. 6.9(a)(d) the theoretical parameters and experimental parameters are quite different. For low nP, both sets of data exhibit a decrease in oscillator strength with increasing electronic

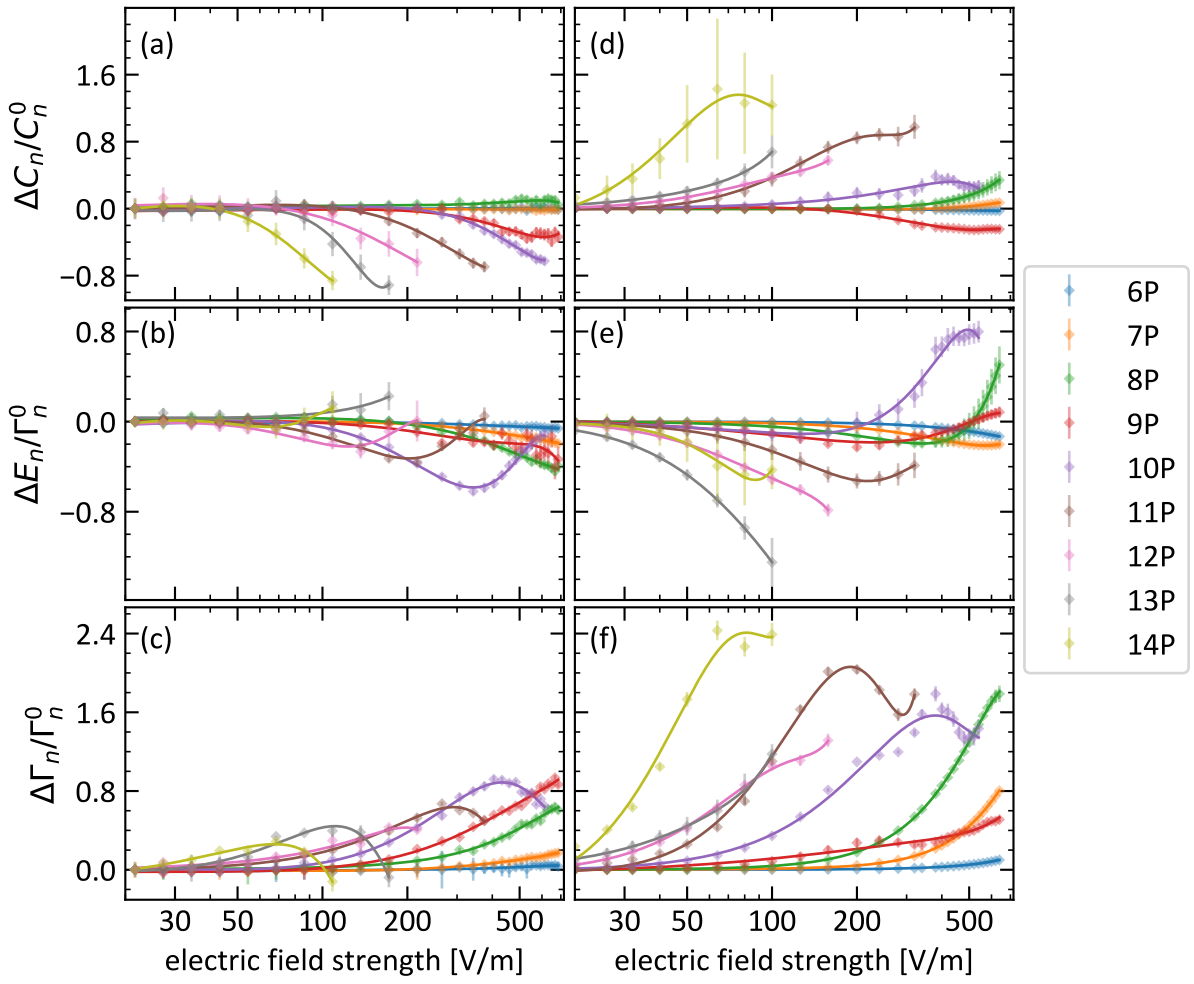

Figure 6.9: Comparison of extracted peak parameters from experimental data (left) and theory data (right). (a, b) fractional change in oscillator strength. (c) and (d) fractional shift in energy level (e) and (f) fraction shift in peak width.

field. However, only the theoretical data shows an increase for high nP states. Similar discrepancies are shown in Fig. 6.9(b)(e) where for higher nP states a far more dramatic change in energy level is observed for the theory parameters. It is however interesting to note that some states do show the previously observed turning point in state position in sufficiently strong fields. The widths, shown in Fig. 6.9(c)(f), show the strongest agreement. In both sets of data, the linewidths grow with increasing electronic field strength. Moreover, both sets of data show the presence of turning points in these trends.

Across all of the data sets there is only weak agreement as to the order of magnitude of the changes in state parameters. With the agreement of the oscillator

strength being particularly poor. This disagreement may be a reflection of flaws in the model. At present, it does not take the asymmetry of the nP states into account and it does not include the role of the phonons. Both of these factors may contribute to the lineshape resulting from the model. Additionally, the model seems particularly weak at higher nP states. This is likely a result of the uncertainty in parameters of the high-lying states due to the difficulty in resolving the even parity series [74].

A further source of the disagreement comes in the form of the fitting procedure used to extract the parameters shown in Fig. 6.9. For the experimental data, the lines could be well described by asymmetric Lorentzians. While for the theory curves that is not the case, it is unlikely that the fitting of a single symmetric Lorentzian is suitable in this case.

While the model is not able to achieve quantitative agreement with experimental data this does present a promising start. Incorporating the missing elements of the model provides the obvious next path.

6.4 Conclusions

Further investigations into the optical response of cuprous oxide in the presence of a microwave field have been able to yield several interesting properties. The saturation of the modulation of the transmission spectrum was shown to saturate at lower microwave field strengths for increasing n of the excitonic states. This was a result of the decreasing oscillator strength and increasing coupling between opposite parity states. Alongside this saturation, additional frequency components corresponding to $\chi^{(5)}$ were detected across the excitonic spectrum. The scaling of the required field with n was in line with the theory predictions of a nonlinearity model. These sidebands were notably weaker than those observed in the previous chapter owing to the requirement of additional transitions. This leads to a weaker coupling due to none of the processes being resonant.

Fitting the excitonic spectra in the increasing microwave field was able to show the changing nature of the states. Virtually all states showed a decrease in oscillator strength and an increase in width. These are the precursors to Autler-Townes splitting. Alongside this, the energy levels of states were shown to move due to the microwave field. In very strong fields the widths were shown to start decreasing

again. Similarly, the energy levels began to shift in the opposite direction. These behaviours indicate that there are two competing effects determining the role of the microwave field. The field where these effects are equally scaled with n^{-7} indicated the polarisability of the state may play a role.

These findings were compared to a Floquet-based atomic theory model. This model was not able to provide good agreement on the behavior of excitonic states but it was able to produce turning points in many trends nonetheless. However, results from this comparison are not strictly speaking accurate as the fitting methods applied to the experimental data are less suited to the theory data due to the much clearer role of Autler-Townes splitting. This was compounded by the difficulty of resolving many high n states in the presence of a strong microwave field in both the experimental and the theory data.

Further work is underway to improve the Floquet model, namely to incorporate the asymmetry of the excitonic states. This should yield improved agreement between experiments and data. A stronger theory will also shed light on the nature of excitonic states in the presence of such strong fields and enable a better understanding of the higher-order nonlinear processes detected throughout this chapter.

Chapter 7

Conclusions

Using photoluminescence spectroscopy and broadband transmission spectroscopy the quality of natural and synthetic samples were compared. The clearest difference between them is the inclusion of copper vacancies in the structure of synthetic materials. These vacancies could be removed with thermal annealing in the air. However, this did not improve the quality of the sample. It appeared to reduce it. This was attributed to the presence of oxygen vacancies in the crystal lattice. It may be possible to remove these vacancies by annealing under different conditions. It is hugely important to continue the development of synthetic materials to remove the dependence on natural samples.

Conducting narrowband transmission spectroscopy on our highest-quality natural samples allowed for a resolution of up to 17P. This value was determined to be limited by the temperature of the crystal rather than the quality of the stone. This was done by resolving the excitonic spectrum over a range of temperatures, where successive states vanished as the temperature was increased. Measurements of the change in width, and oscillator strength, of states with increasing temperature are consistent with those reported in previous investigations. Despite this limitation sufficiently high excitonic states could be resolved to allow for novel Rydberg physics to be carried out.

The microwave-induced $\chi^{(3)}$ optical nonlinearities were studied through the application of microwave fields across the best sample. This resulted in significant changes to the transmission spectrum which were in quantitative agreement with an atomic physics-based model of $\chi^{(3)}$ for low microwave field strength. Alongside this, additional frequency components were introduced into the transmission

spectrum corresponding to frequency sum and difference generation processes. These were not well predicted by the model. The capability of the model to accurately predict the transmission, but fail for additional frequency components, was attributed to the different resonant conditions of the two processes. For the carrier, only two states were involved, compared to the three for the sidebands. Combined with the uncertainty in the location and width of states this may have led to the inaccuracies. Additionally, resolving the polarisation states of the different frequency components yielded the following relationship for the elements of the $\chi^{(3)}$ tensor. This was derived from the invariance of the polarisation state in the presence of a microwave field. Finally, by measuring the intensity of the additional frequency components at a location on the excitonic spectrum where the change in absorption was zero, a massive cross-Kerr nonlinearity was estimated. This is many orders of magnitude larger than what is seen for the archetypal Kerr media.

The response of cuprous oxide in even larger microwave fields was investigated in the final chapter. Here, the onset of saturation of the modulation was shown to occur at lower microwave field strengths for higher nP. This was attributed to the lower oscillator strength leading to a lower threshold for saturation. Alongside things, higher-order nonlinearities were observed which appeared to obey the expected power law scaling with n. Further work is underway to model this higher-order phenomenon using a Floquet theorem-based approach. This was not able to reproduce the variation in states with increasing microwave field strength. However, the model does not take into account the asymmetry of the nP states or the interactions between excitons and phonons which may account for this discrepancy.

This thesis has continued the work carried out by [55] in developing cuprous oxide as a Rydberg physics platform. The observation of a large $\chi^{(3)}$ nonlinearity highlights the potential of this material. This is particularly notable as this work has been conducted on a natural sample that has been subjected to minimal processing. Combined with the relative simplicity of the microwave antennae used to apply microwave fields it is clear that larger nonlinearities could be observed if better control over the microwave field was achieved. To this end, work is underway in developing and characterising resonator microwave antennae. This will instead offer a much clearer picture of the microwave fields across and within the sample. This will also be a more realistic mapping to superconducting res-

onator circuits, offering a chance to demonstrate the viability of cuprous oxide in this context. Alongside this, the Floquet model will be further developed to better understand the emergence and behaviour of higher-order nonlinearities. In particular, this will help to make quantitative predictions for the change in the optical properties of cuprous oxide in the presence of a microwave field. Here, treating the polarisation state of the input laser light remains an outstanding challenge.

Moving forward, this project will also seek to observe quantum states of light generated from cuprous oxide. Specifically anti-bunched light. These states can be generated through the exploitation of the Rydberg blockade by using tightly focused laser spots. Here, only a single exciton is made within the blockaded region [9]. This can be realised in either the second harmonic generation or transmission regime and verified by measuring the correlation function $g^{(2)}$. Specifically, two photon-counters are already present in the lab for such an experiment. Preliminary measurements of this have already been made in the transmission regime, but the results are inconclusive. In all likelihood, the best chance to observe the characteristic drop in $g^{(2)}$ associated with anti-bunched will be in the SHG regime. Here, we do not need to worry about the phononic part of the excitonic spectrum as we excite directly to the excitonic states. Success here will enable cuprous oxide to be used as a source of single photons. Doing so would further cement this material as a viable platform for Rydberg physics.

Appendix A

Calculating Nonlinear Susceptibility

As laid out in Chapter 2 excitons can be reasonably treated as hydrogenic objects. This enables the use of a nonlinear susceptibility model to describe the optical properties of cuprous oxide in the presence of a microwave field. Such a model requires the oscillator strengths, line widths and energies of the excitonic resonances. These can be experimentally determined by fitting spectra. Alongside this, we require the matrix transition elements describing the coupling between different excitonic states. These are determined from theoretical calculations based on the excitonic wavefunctions. Once all of these parameters have been obtained the nonlinear susceptibility can be evaluated to provide a quantitative comparison between theory and experiment. A further complication is that the broad linewidths in cuprous oxide result in the states overlapping at higher principle quantum numbers. This demands that we must sum over all available transitions rather than only considering a few isolated resonances. We will start this discussion by exploring how the spectral parameters are determined.

A.1 Extracting Spectral Parameters

The excitonic linewidths, Γ_{n}, energies, E_{n}, and oscillator strengths, C_{n}, are determined by fitting transmission spectra using:

$$\alpha_{\mathrm{n}} = C_{\mathrm{n}} \frac{\Gamma_{\mathrm{n}}}{\Gamma_{\mathrm{n}}^2 + \delta_n^2} + B_{\mathrm{n}}, \tag{A.1}$$

for an isolated resonance, where δ_n is the detuning of the laser from a state with energy E_{n} and B_{n} is a constant term taking the background into account. Here.

the asymmetry term has been neglected. States are fitted separately using this method. Applying this to the spectra collected in Chapter 4 enables parameters for states up to 17P to be determined. This was the highest resolvable state in this system. To account for the role of higher-lying states we extrapolate on trends in spectral parameters, such as those shown in Fig. 4.5 to estimate their parameters. This of course only accounts for odd parity nP states, which can be observed using transmission spectroscopy. To determine these parameters for even parity nS and nD states we instead make use of second harmonic generation (SHG) spectroscopy. The details of such an experiment can be found in [84; 74]. Here, we can only observe up to 12D, so far more extrapolation must be used to estimate the properties of higher-lying states.

The oscillator strength is converted into a dipole matrix element through the following relationship [123]:

$$C_{\mathrm{n}} = \frac{k}{\epsilon_0 \eta} |D^{\mathrm{VB}\Rightarrow\mathrm{nP}}|^2, \tag{A.2}$$

for wavevector k and refractive index η. This is derived by taking the real part of the linear susceptibility to find the corresponding absorption.

A.1.1 Calculating Matrix Transition Elements

Matrix transition elements are calculated from the theoretical values of the excitonic wave functions. Further details on this can be found in [173; 174].

A.2 Determining Optical Properties

Both the refractive index and absorption can be determined from the electronic susceptibility. These are obtained from the real and imaginary parts of χ respectively. We are specifically interested in the modification to these properties as a result of the third-order nonlinearity $\chi^{(3)}$, which only plays a role when the microwave field is turned on. This is determined by evaluating:

$$\chi^{(3)}(\omega_L \pm \Omega \mp \Omega) = \sum_{n,n',l,\pm} \frac{N}{\epsilon_0 \hbar} \frac{|\mathrm{D}^{\mathrm{VB}\Rightarrow\mathrm{nP}}|^2 D^{\mathrm{nP}\Rightarrow\mathrm{n'l}} D^{\mathrm{n'l}\Rightarrow\mathrm{n''P'}}}{(\delta_{\mathrm{nP}} - i\Gamma_{\mathrm{nP}})(\delta_{\mathrm{n'l}} - i\Gamma_{\mathrm{n'l}} \pm i\Omega)(\delta_{\mathrm{n''P'}} - i\Gamma_{\mathrm{n''P'}})}, \tag{A.3}$$

where Ω is the microwave frequency, ω_{L} is the laser frequency, $\mathrm{D}^{\mathrm{VB}\Rightarrow\mathrm{nP}}$ is the dipole matrix element for the transition between the valance band and nP exciton, $D^{\mathrm{nP}\Rightarrow\mathrm{n'l}}$ is the transition matrix element between opposite parity states, Γ is the linewidth of the associated state and δ is the detuning from the associated state. This is expressed as a summation due to the overlapping nature of adjacent states. In this work, this is evaluated in three different frequency regimes. The first, known as the "carrier" frequency is at the same frequency as the excitation laser. This corresponds to the final state nP state being the same as the initial nP state or one which is overlapping with it. The other two regimes are detuned from the laser frequency by twice the microwave frequency known as the "red" and "blue" sidebands. In this regime, the final nP state is typically different from the initial one. However, for particularly wide states this is may not be the case.

Bibliography

[1] N. Bohr, "Ii. the trilogy: On the constitution of atoms and molecules," in *Work on Atomic Physics (1912–1917)*, Niels Bohr Collected Works, Vol. 2, edited by L. Rosenfeld and U. Hoyer (Elsevier, 1981) pp. 159–233.

[2] A. Lakhtakia and E. E. Salpeter, "Models and Modelers of Hydrogen," American Journal of Physics **65**, 933 (1997).

[3] B. H. Bransden and C. J. Joachain, *Physics of Atoms and Molecules; 2nd ed.* (Prentice-Hall, Harlow, 2003).

[4] J. L. Bromberg, "The Birth of the Laser," Physics Today **41**, 26 (1988).

[5] T. Gallagher, A. Dalgarno, C. U. Press, F. Read, and R. Zare, *Rydberg Atoms*, Cambridge Monographs on Atomic, Molecular and Chemical Physics (Cambridge University Press, 1994).

[6] A. S. Edelstein and T. Gallagher, "Rydberg," (Academic Press, 1979) pp. 365–392.

[7] S. Yoshida, J. Burgdörfer, X. Zhang, and F. B. Dunning, "Rydberg blockade in a hot atomic beam," Phys. Rev. A **95**, 042705 (2017).

[8] D. Tong, S. M. Farooqi, J. Stanojevic, S. Krishnan, Y. P. Zhang, R. Côté, E. E. Eyler, and P. L. Gould, "Local blockade of rydberg excitation in an ultracold gas," Phys. Rev. Lett. **93**, 063001 (2004).

[9] N. Šibalić and C. S. Adams, *Rydberg Physics* (IOP Publishing, Bristol, UK, 2018).

[10] S. Ravets, H. Labuhn, D. Barredo, L. Béguin, T. Lahaye, and A. Browaeys, "Coherent dipole–dipole coupling between two single rydberg atoms at an electrically-tuned förster resonance," Nature Physics **10**, 914 (2014).

[11] C. S. Adams, J. D. Pritchard, and J. P. Shaffer, "Rydberg atom quantum technologies," Journal of Physics B: Atomic, Molecular and Optical Physics **53**, 012002 (2019).

[12] A. A. Morgan and S. D. Hogan, "Coupling rydberg atoms to microwave fields in a superconducting coplanar waveguide resonator," Phys. Rev. Lett. **124**, 193604 (2020).

[13] A. K. Mohapatra, T. R. Jackson, and C. S. Adams, "Coherent optical detection of highly excited rydberg states using electromagnetically induced transparency," Phys. Rev. Lett. **98**, 113003 (2007).

[14] N. Šibalić and C. S. Adams, *Rydberg Physics*, 2399-2891 (IOP Publishing, 2018).

[15] E. Urban, T. A. Johnson, T. Henage, L. Isenhower, D. D. Yavuz, T. G. Walker, and M. Saffman, "Observation of Rydberg blockade between two atoms," Nature Physics **5**, 110 (2009).

[16] N. Tomm, A. Javadi, N. O. Antoniadis, D. Najer, M. C. Löbl, A. R. Korsch, R. Schott, S. R. Valentin, A. D. Wieck, A. Ludwig, and R. J. Warburton, "A bright and fast source of coherent single photons," Nature Nanotechnology **16**, 399 (2021), arXiv:2007.12654 [quant-ph] .

[17] F. Ripka, H. Kübler, R. Löw, and T. Pfau, "A room-temperature single-photon source based on strongly interacting Rydberg atoms," Science **362**, 446 (2018).

[18] D. Barredo, S. Ravets, H. Labuhn, L. Béguin, A. Vernier, F. Nogrette, T. Lahaye, and A. Browaeys, "Demonstration of a strong rydberg blockade in three-atom systems with anisotropic interactions," Phys. Rev. Lett. **112**, 183002 (2014).

[19] D. P. Ornelas-Huerta, A. N. Craddock, E. A. Goldschmidt, A. J. Hachtel, Y. Wang, P. Bienias, A. V. Gorshkov, S. L. Rolston, and J. V. Porto, "On-demand indistinguishable single photons from an efficient and pure source based on a rydberg ensemble," Optica **7**, 813 (2020).

[20] J. Vaneecloo, S. Garcia, and A. Ourjoumtsev, "Intracavity rydberg superatom for optical quantum engineering: Coherent control, single-shot detection, and optical π phase shift," Phys. Rev. X **12**, 021034 (2022).

[21] A. Padrón-Brito, J. Lowinski, P. Farrera, K. Theophilo, and H. de Riedmatten, "Probing the indistinguishability of single photons generated by rydberg atomic ensembles," Phys. Rev. Res. **3**, 033287 (2021).

[22] S. Baur, D. Tiarks, G. Rempe, and S. Dürr, "Single-photon switch based on Rydberg blockade," Phys. Rev. Lett. **112**, 073901 (2014).

[23] H. Zhang, J. Wu, M. Artoni, and G. C. La Rocca, "Single-photon-level light storage with distributed Rydberg excitations in cold atoms," Frontiers of Physics **17**, 22502 (2022).

[24] C. Tresp, C. Zimmer, I. Mirgorodskiy, H. Gorniaczyk, A. Paris-Mandoki, and S. Hofferberth, "Single-photon absorber based on strongly interacting Rydberg atoms," Phys. Rev. Lett. **117**, 223001 (2016).

[25] J. Kumlin, C. Braun, C. Tresp, N. Stiesdal, S. Hofferberth, and A. Paris-Mandoki, "Quantum optics with Rydberg superatoms," Journal of Physics Communications **7**, 052001 (2023).

[26] P. Minzioni, C. Lacava, T. Tanabe, J. Dong, X. Hu, G. Csaba, W. Porod, G. Singh, A. E. Willner, A. Almaiman, V. Torres-Company, J. Schröder, A. C. Peacock, M. J. Strain, F. Parmigiani, G. Contestabile, D. Marpaung, Z. Liu, J. E. Bowers, L. Chang, S. Fabbri, M. Ramos Vázquez, V. Bharadwaj, S. M. Eaton, P. Lodahl, X. Zhang, B. J. Eggleton, W. J. Munro, K. Nemoto, O. Morin, J. Laurat, and J. Nunn, "Roadmap on all-optical processing," Journal of Optics **21**, 063001 (2019).

[27] A. E. Willner, S. Khaleghi, M. R. Chitgarha, and O. F. Yilmaz, "All-optical signal processing," J. Lightwave Technol. **32**, 660 (2014).

[28] Y. He, P. Wang, C. Wang, J. Liu, H. Ye, X. Zhou, Y. Li, S. Chen, X. Zhang, and D. Fan, "All-optical signal processing in structured light multiplexing with dielectric meta-optics," ACS Photonics **7**, 135 (2020).

[29] C. Langrock, S. Kumar, J. Mcgeehan, A. Willner, and M. Fejer, "All-optical signal processing using chi(2) nonlinearities in guided-wave devices," Journal of Lightwave Technology **24**, 2579 (2006).

[30] D. Paredes-Barato and C. S. Adams, "All-optical quantum information processing using rydberg gates," Phys. Rev. Lett. **112**, 040501 (2014).

[31] A. N. Tuan, D. L. Van, and B. N. Huy, "Manipulating multi-frequency light in a five-level cascade-type atomic medium associated with giant self-kerr nonlinearity," J. Opt. Soc. Am. B **35**, 1233 (2018).

[32] K. Srakaew, P. Weckesser, S. Hollerith, D. Wei, D. Adler, I. Bloch, and J. Zeiher, "A subwavelength atomic array switched by a single rydberg atom," (2022).

[33] J. Block and S. Scheel, "Casimir–polder induced rydberg macrodimers," (2019).

[34] A. Laliotis, B.-S. Lu, M. Ducloy, and D. Wilkowski, "Atom-surface physics: A review," AVS Quantum Science **3**, 043501 (2021).

[35] D. Petrosyan, K. Mølmer, J. Fortágh, and M. Saffman, "Microwave to optical conversion with atoms on a superconducting chip," New Journal of Physics **21**, 073033 (2019).

[36] J. D. Pritchard, D. Maxwell, A. Gauguet, K. J. Weatherill, M. P. A. Jones, and C. S. Adams, "Cooperative atom-light interaction in a blockaded rydberg ensemble," Phys. Rev. Lett. **105**, 193603 (2010).

[37] X. Wu, X. Liang, Y. Tian, F. Yang, C. Chen, Y.-C. Liu, M. K. Tey, and L. You, "A concise review of rydberg atom based quantum computation and quantum simulation*," Chinese Physics B **30**, 020305 (2021).

[38] M. Saffman, "Quantum computing with atomic qubits and Rydberg interactions: progress and challenges," Journal of Physics B: Atomic, Molecular and Optical Physics **49**, 202001 (2016).

[39] S. R. Cohen and J. D. Thompson, "Quantum computing with circular rydberg atoms," PRX Quantum **2**, 030322 (2021).

[40] C. Adams, J. Pritchard, and J. Shaffer, "Rydberg atom quantum technologies," (2019).

[41] P. L. Ocola, I. Dimitrova, B. Grinkemeyer, E. Guardado-Sanchez, T. Dordevic, P. Samutpraphoot, V. Vuletic, and M. D. Lukin, "Control

and entanglement of individual rydberg atoms near a nanoscale device," (2022), arXiv:2210.12879 [physics.atom-ph] .

[42] M. T. Simons, A. B. Artusio-Glimpse, A. K. Robinson, N. Prajapati, and C. L. Holloway, "Rydberg atom-based sensors for radio-frequency electric field metrology, sensing, and communications," Measurement: Sensors **18**, 100273 (2021).

[43] L. A. Downes, A. R. MacKellar, D. J. Whiting, C. Bourgenot, C. S. Adams, and K. J. Weatherill, "Full-field terahertz imaging at kilohertz frame rates using atomic vapor," Phys. Rev. X **10**, 011027 (2020).

[44] S. Miller, D. Anderson, and G. Raithel, "Radio-frequency-modulated rydberg states in a vapor cell," New Journal of Physics **18** (2016).

[45] H. Zou, Z. Song, H. Mu, Z. Feng, J. Qu, and Q. Wang, "Atomic receiver by utilizing multiple radio-frequency coupling at rydberg states of rubidium," Applied Sciences **10**, 1346 (2020).

[46] Y.-G. Liu, K. Xia, and S.-L. Zhu, "Efficient microwave-to-optical single-photon conversion with a single flying circular rydberg atom," Opt. Express **29**, 9942 (2021).

[47] J. Kelly, R. Barends, A. G. Fowler, A. Megrant, E. Jeffrey, T. C. White, D. Sank, J. Y. Mutus, B. Campbell, Y. Chen, Z. Chen, B. Chiaro, A. Dunsworth, I.-C. Hoi, C. Neill, P. J. J. O'Malley, C. Quintana, P. Roushan, A. Vainsencher, J. Wenner, A. N. Cleland, and J. M. Martinis, "State preservation by repetitive error detection in a superconducting quantum circuit," Nature **519**, 66 (2015).

[48] M. Hofheinz, E. M. Weig, M. Ansmann, R. C. Bialczak, E. Lucero, M. Neeley, A. D. O'Connell, H. Wang, J. M. Martinis, and A. N. Cleland, "Generation of Fock states in a superconducting quantum circuit," Nature **454**, 310 (2008).

[49] P. Kurpiers, P. Magnard, T. Walter, B. Royer, M. Pechal, J. Heinsoo, Y. Salathé, A. Akin, S. Storz, J.-C. Besse, S. Gasparinetti, A. Blais, and A. Wallraff, "Deterministic quantum state transfer and remote entanglement using microwave photons," Nature **558**, 264 (2018).

[50] Y. P. Zhong, H.-S. Chang, K. J. Satzinger, M.-H. Chou, A. Bienfait, C. R. Conner, É. Dumur, J. Grebel, G. A. Peairs, R. G. Povey, D. I. Schuster, and A. N. Cleland, "Violating Bell's inequality with remotely connected superconducting qubits," Nature **15**, 741 (2019).

[51] S.-K. Liao, W.-Q. Cai, W.-Y. Liu, L. Zhang, Y. Li, J.-G. Ren, J. Yin, Q. Shen, Y. Cao, Z.-P. Li, F.-Z. Li, X.-W. Chen, L.-H. Sun, J.-J. Jia, J.-C. Wu, X.-J. Jiang, J.-F. Wang, Y.-M. Huang, Q. Wang, Y.-L. Zhou, L. Deng, T. Xi, L. Ma, T. Hu, Q. Zhang, Y.-A. Chen, N.-L. Liu, X.-B. Wang, Z.-C. Zhu, C.-Y. Lu, R. Shu, C.-Z. Peng, J.-Y. Wang, and J.-W. Pan, "Satellite-to-ground quantum key distribution," Nature **549**, 43 (2017).

[52] Y. Yu, F. Ma, X.-Y. Luo, B. Jing, P.-F. Sun, R.-Z. Fang, C.-W. Yang, H. Liu, M.-Y. Zheng, X.-P. Xie, W.-J. Zhang, L.-X. You, Z. Wang, T.-Y. Chen, Q. Zhang, X.-H. Bao, and J.-W. Pan, "Entanglement of two quantum memories via fibres over dozens of kilometres," Nature **578**, 240 (2020).

[53] T. Vogt, C. Gross, J. Han, S. B. Pal, M. Lam, M. Kiffner, and W. Li, "Efficient microwave-to-optical conversion using rydberg atoms," Phys. Rev. A **99**, 023832 (2019).

[54] M. Khazali, K. Heshami, and C. Simon, "Single-photon source based on Rydberg exciton blockade," Journal of Physics B: Atomic, Molecular and Optical Physics **50**, 215301 (2017).

[55] L. A. P. GALLAGHER, *Optical and microwave spectroscopy of Rydberg excitons in Cu_2O*, Ph.D. thesis, Durham University (2022).

[56] H. Stolz, F. Schöne, and D. Semkat, "Interaction of Rydberg excitons in cuprous oxide with phonons and photons: optical linewidth and polariton effect," New Journal of Physics **20**, 023019 (2018).

[57] J. DeLange, K. Barua, V. Zwiller, S. Steinhauer, and H. Alaeian, "Highly-Excited Rydberg Excitons in Synthetic Thin-Film Cuprous Oxide," (2022), arXiv:2210.16416 [quant-ph] .

[58] T. Kazimierczuk, D. Fröhlich, S. Scheel, H. Stolz, and M. Bayer, "Giant Rydberg excitons in the copper oxide Cu_2O," Nature **514**, 343 (2014).

[59] M. A. M. Versteegh, S. Steinhauer, J. Bajo, T. Lettner, A. Soro, A. Romanova, S. Gyger, L. Schweickert, A. Mysyrowicz, and V. Zwiller, "Giant Rydberg excitons in Cu_2O probed by photoluminescence excitation spectroscopy," (2021), arXiv:2105.07942 [cond-mat.mes-hall] .

[60] J. Singh and R. Williams, *Excitonic and Photonic Processes in Materials* (Springer, 2015).

[61] R. W. Boyd, *Nonlinear Optics, Third Edition*, 3rd ed. (Academic Press, Inc., USA, 2008).

[62] G. H. Wannier, "The structure of electronic excitation levels in insulating crystals," Phys. Rev. **52**, 191 (1937).

[63] J. M. F. Gunn, "Collective excitations in rare gas solids," Journal of Physics C: Solid State Physics **13**, 3841 (1980).

[64] J. Heckötter, V. Walther, S. Scheel, M. Bayer, T. Pohl, and M. Aßmann, "Asymmetric rydberg blockade of giant excitons in cuprous oxide," Nature Communications **12** (2021).

[65] S. B. Nam, D. C. Reynolds, C. W. Litton, R. J. Almassy, T. C. Collins, and C. M. Wolfe, "Free-exciton energy spectrum in GaAs," Phys. Rev. B **13**, 761 (1976).

[66] G. Macfarlane, T. McLean, J. Quarrington, and V. Roberts, "Exciton and phonon effects in the absorption spectra of germanium and silicon," Journal of Physics and Chemistry of Solids **8**, 388 (1959).

[67] "Band gap energy and binding energies of z3-excitions in cucl," Solid State Communications **94**, 33 (1995).

[68] S. V. Nair, J. Usukura, and E. Tokunaga, "Accurate modeling of electron-hole binding in cucl. i. exciton states," Phys. Rev. B **102**, 075202 (2020).

[69] J. Xiao, M. Zhao, Y. Wang, and X. Zhang, "Excitons in atomically thin 2d semiconductors and their applications," Nanophotonics **6**, 1309 (2017).

[70] E. F. Gross, "Optical spectrum of excitons in the crystal lattice," Il Nuovo Cimento **3**, 672 (1956).

[71] A. Bennett, M. Pooley, R. Stevenson, M. Ward, R. Patel, A. Giroday, N. Sköld, I. Farrer, C. Nicoll, D. Ritchie, and A. Shields, "Electric-field-induced coherent coupling of the exciton states in a single quantum dot," Nature Physics **6** (2012).

[72] S. De Rinaldis, R. Rinaldi, R. Cingolani, I. D'Amico, E. Biolatti, and F. Rossi, "Intrinsic dipole–dipole excitonic coupling in gan quantum dots: application to quantum information processing," Physica E: Low-dimensional Systems and Nanostructures **13**, 624 (2002).

[73] J. Horng, Y.-H. Chou, T.-C. Chang, C.-Y. Hsu, T.-C. Lu, and H. Deng, "Engineering radiative coupling of excitons in 2d semiconductors," Optica **6**, 1443 (2019).

[74] L. A. P. Gallagher, J. P. Rogers, J. D. Pritchett, R. A. Mistry, D. Pizzey, C. S. Adams, M. P. A. Jones, P. Grünwald, V. Walther, C. Hodges, W. Langbein, and S. A. Lynch, "Microwave-optical coupling via Rydberg excitons in cuprous oxide," Phys. Rev. Research **4**, 013031 (2022).

[75] J. L. Lin and J. P. Wolfe, "Bose-Einstein condensation of paraexcitons in stressed Cu_2O," Phys. Rev. Lett. **71**, 1222 (1993).

[76] D. Snoke and G. M. Kavoulakis, "Bose–einstein condensation of excitons in cu2o: progress over 30 years," Reports on Progress in Physics **77**, 116501 (2014).

[77] R. Casella, "On the possibility of observing a bose-einstein condensation of excitons in cds and cdse," Journal of Physics and Chemistry of Solids **24**, 19 (1963).

[78] L. Butov, C. Lai, A. Ivanov, A. Gossard, and D. Chemla, "Exciton condensation in potential traps," in *2002 Summaries of Papers Presented at the Quantum Electronics and Laser Science Conference* (2002) pp. 167–.

[79] A. Mysyrowicz, D. Hulin, and A. Antonetti, "Long exciton lifetime in Cu_2O," Phys. Rev. Lett. **43**, 1123 (1979).

[80] A. Lakshmanan, Z. C. Alex, and S. Meher, "Recent advances in cuprous oxide thin film based photovoltaics," Materials Today Sustainability **20**, 100244 (2022).

[81] G. Han, W. H. Du, B.-L. An, A. Bruno, S. W. Leow, C. Soci, S. Zhang, S. G. Mhaisalkar, and N. Mathews, "Nitrogen doped cuprous oxide as low cost hole-transporting material for perovskite solar cells," Scripta Materialia **153**, 104 (2018).

[82] S. Petrovic, M. Rajčić-Vujasinović, Z. Stevic, and V. Grekulovi, "Cuprous oxide as an active material for solar cells," (2011).

[83] S. A. Lynch, C. Hodges, S. Mandal, W. Langbein, R. P. Singh, L. A. P. Gallagher, J. D. Pritchett, D. Pizzey, J. P. Rogers, C. S. Adams, and M. P. A. Jones, "Rydberg excitons in synthetic cuprous oxide Cu_2O," Phys. Rev. Materials **5**, 084602 (2021).

[84] J. P. Rogers, L. A. P. Gallagher, D. Pizzey, J. D. Pritchett, C. S. Adams, M. P. A. Jones, C. Hodges, W. Langbein, and S. A. Lynch, "High resolution nanosecond spectroscopy of even-parity Rydberg excitons in Cu_2O," (2021), arXiv:2111.13062 [cond-mat.mes-hall] .

[85] W. G. Aulbur, L. Jönsson, and J. W. Wilkins, "Quasiparticle calculations in solids," (Academic Press, 2000) pp. 1–218.

[86] C. Kittel, *Introduction to solid state physics*, 8th ed. (John Wiley Sons, New York, NY, 2023).

[87] M. Cardona and Y. Y. Peter, *Fundamentals of semiconductors*, 4th ed. (Springer, 2005).

[88] N. Ashcroft and N. Mermin, *Solid State Physics* (Saunders College Publishing, Fort Worth, 1976).

[89] J. W. Anthony, R. A. Bideaux, K. W. Bladh, and M. C. Nichols, *Handbook of Mineralogy* (Mineralogical Society of America, 2002).

[90] B. K. Meyer, A. Polity, D. Reppin, M. Becker, P. Hering, B. Kramm, P. J. Klar, T. Sander, C. Reindl, C. Heiliger, M. Heinemann, C. Müller, and C. Ronning, "Chapter six - the physics of copper oxide (Cu_2O)," in *Oxide Semiconductors*, Semiconductors and Semimetals, Vol. 88, edited by B. G. Svensson, S. J. Pearton, and C. Jagadish (Elsevier, 2013) pp. 201 – 226.

[91] J. Dahl and A. Switendick, "Energy bands in cuprous oxide," Journal of Physics and Chemistry of Solids **27**, 931 (1966).

[92] L. Kleinman and K. Mednick, "Self-consistent energy bands of Cu_2O," Phys. Rev. B **21**, 1549 (1980).

[93] J. Robertson, "Electronic structure and x-ray near-edge core spectra of Cu_2O," Physical Review B **28**, 3378 (1983).

[94] M. French, R. Schwartz, H. Stolz, and R. Redmer, "Electronic band structure of Cu_2O by spin density functional theory," Journal of Physics: Condensed Matter **21**, 015502 (2008).

[95] G. F. Koster, *Properties of the thirty-two point groups* (M.I.T. Press, Cambridge, Mass., 1963).

[96] F. Schöne, *Optical Properties of yellow Excitons in Cuprous Oxide*, Ph.D. thesis, der Universität Rostock (2018).

[97] M. Takahata and N. Naka, "Photoluminescence properties of the entire excitonic series in cu_2O," Phys. Rev. B **98**, 195205 (2018).

[98] W. Ubachs, J. Koelemeij, K. Eikema, and E. Salumbides, "Physics beyond the standard model from hydrogen spectroscopy," Journal of Molecular Spectroscopy **320**, 1 (2016).

[99] V. I. Korobov, "Precision spectroscopy of the hydrogen molecular ions: Present status of theory and experiment," Physics of Particles and Nuclei **53**, 787 (2022).

[100] D. A. McQuarrie, *Quantum chemistry* (University Science Books, Herndon, 1983).

[101] G. Dresselhaus, "Effective mass approximation for excitons," Journal of Physics and Chemistry of Solids **1**, 14 (1956).

[102] G. H. Wannier, "The structure of electronic excitation levels in insulating crystals," Phys. Rev. **52**, 191 (1937).

[103] C. Uihlein, D. Fröhlich, and R. Kenklies, "Investigation of exciton fine structure in Cu_2O," Phys. Rev. B **23**, 2731 (1981).

[104] J. Heckötter, *Strongly interacting Rydberg excitons in Cu_2O*, Ph.D. thesis, TU Dortmund University (2020).

[105] J. Heckötter, P. Rommel, J. Main, M. Aßmann, and M. Bayer, "Analysis of the fine structure of the *D*-exciton shell in cuprous oxide," physica status solidi (RRL) – Rapid Research Letters **15**, 2100335 (2021).

[106] P. Rommel, J. Main, S. O. Krüger, and S. Scheel, "Interseries dipole transitions from yellow to green excitons in cuprous oxide," Phys. Rev. B **104**, 085204 (2021).

[107] H.-R. Trebin, "Exciton—phonon interaction in the degenerate-band case," physica status solidi (b) **92**, 601 (1979).

[108] F. Schweiner, J. Main, and G. Wunner, "Linewidths in excitonic absorption spectra of cuprous oxide," Phys. Rev. B **93**, 085203 (2016).

[109] G. Kuwabara, M. Tanaka, and H. Fukutani, "Optical absorption due to paraexciton of cu2o," Solid State Communications **21**, 599 (1977).

[110] J. Brandt, D. Fröhlich, C. Sandfort, M. Bayer, H. Stolz, and N. Naka, "Ultranarrow optical absorption and two-phonon excitation spectroscopy of cu_2O paraexcitons in a high magnetic field," Phys. Rev. Lett. **99**, 217403 (2007).

[111] J. Heckötter, M. Freitag, D. Fröhlich, M. Aßmann, M. Bayer, M. A. Semina, and M. M. Glazov, "Scaling laws of Rydberg excitons," Phys. Rev. B **96**, 125142 (2017).

[112] J. Heckötter, M. Freitag, D. Fröhlich, M. Aßmann, M. Bayer, P. Grünwald, F. Schöne, D. Semkat, H. Stolz, and S. Scheel, "Rydberg excitons in the presence of an ultralow-density electron-hole plasma," Phys. Rev. Lett. **121**, 097401 (2018).

[113] M. Heckötter, J.and Freitag, D. Fröhlich, M. Aßmann, M. Bayer, M. A. Semina, and M. M. Glazov, "Influence of the wavefunction distribution on exciton dissociation in electric field," Physics of the Solid State **60**, 1506 (2018).

[114] M. A. Semina, "Fine Structure of Rydberg Excitons in Cuprous Oxide," Physics of the Solid State **60**, 1527 (2018).

[115] F. Schöne, S.-O. Krüger, P. Grünwald, M. Aßmann, J. Heckötter, J. Thewes, H. Stolz, D. Fröhlich, M. Bayer, and S. Scheel, "Coupled valence

band dispersions and the quantum defect of excitons in Cu_2O," Journal of Physics B: Atomic, Molecular and Optical Physics **49**, 134003 (2016).

[116] C. Foot, *Atomic Physics*, Oxford Master Series in Physics (OUP Oxford, 2004).

[117] F. Schweiner, J. Ertl, J. Main, G. Wunner, and C. Uihlein, "Exciton-polaritons in cuprous oxide: Theory and comparison with experiment," Phys. Rev. B **96**, 245202 (2017).

[118] A. Baldereschi and N. O. Lipari, "Cubic contributions to the spherical model of shallow acceptor states," Phys. Rev. B **9**, 1525 (1974).

[119] A. Baldereschi and N. O. Lipari, "Spherical model of shallow acceptor states in semiconductors," Phys. Rev. B **8**, 2697 (1973).

[120] A. Farenbruch, J. Mund, D. Fröhlich, D. R. Yakovlev, M. Bayer, M. A. Semina, and M. M. Glazov, "Magneto-Stark and Zeeman effect as origin of second harmonic generation of excitons in Cu_2O," Phys. Rev. B **101**, 115201 (2020).

[121] L. Frazer, E. J. Lenferink, K. B. Chang, K. R. Poeppelmeier, N. P. Stern, and J. B. Ketterson, "Evaluation of defects in cuprous oxide through exciton luminescence imaging," Journal of Luminescence **159**, 294 (2015).

[122] S. Gastev, A. Kaplyanskii, and N. Sokolov, "Relaxed excitons in cu2o," Solid State Communications **42**, 389 (1982).

[123] R. J. Elliott, "Intensity of optical absorption by excitons," Phys. Rev. **108**, 1384 (1957).

[124] F. Schöne, H. Stolz, and N. Naka, "Phonon-assisted absorption of excitons in Cu_2O," Phys. Rev. B **96**, 115207 (2017).

[125] Y. Toyozawa, "Interband effect of lattice vibrations in the exciton absorption spectra," Journal of Physics and Chemistry of Solids **25**, 59 (1964).

[126] Y. Toyozawa, "Theory of line-shapes of the exciton absorption bands," Progress of Theoretical Physics **20**, 53 (1958).

[127] A. Jolk and C. F. Klingshirn, "Linear and nonlinear excitonic absorption and photoluminescence spectra in cu2o: Line shape analysis and exciton drift," physica status solidi (b) **206**, 841 (1998).

[128] S. J. Ikhmayies and R. N. Ahmad-Bitar, "A study of the optical bandgap energy and urbach tail of spray-deposited cds:in thin films," Journal of Materials Research and Technology **2**, 221 (2013).

[129] J. D. Dow and D. Redfield, "Toward a unified theory of Urbach's rule and exponential absorption edges," Phys. Rev. B **5**, 594 (1972).

[130] S. John, C. Soukoulis, M. H. Cohen, and E. N. Economou, "Theory of electron band tails and the Urbach optical-absorption edge," Phys. Rev. Lett. **57**, 1777 (1986).

[131] S. O. Krüger, H. Stolz, and S. Scheel, "Interaction of charged impurities and Rydberg excitons in cuprous oxide," Phys. Rev. B **101**, 235204 (2020).

[132] P. Rommel, J. Main, A. Farenbruch, J. Mund, D. Fröhlich, D. R. Yakovlev, M. Bayer, and C. Uihlein, "Second harmonic generation of cuprous oxide in magnetic fields," Phys. Rev. B **101**, 115202 (2020).

[133] J. Heckötter, M. Freitag, D. Fröhlich, M. Aßmann, M. Bayer, M. A. Semina, and M. M. Glazov, "High-resolution study of the yellow excitons in Cu_2O subject to an electric field," Phys. Rev. B **95**, 035210 (2017).

[134] B. Cairncross and S. Moir, "The onganja mining district namibia," **27**, 85 (1996).

[135] M. D. Cowing, "Objective diamond clarity grading," The Journal of Gemmology **34**, 316 (2014).

[136] T. Ito, H. Yamaguchi, K. Okabe, and T. Masumi, "Single-crystal growth and characterization of Cu_2O and CuO," Journal of Materials Science **33**, 3555 (1998).

[137] S. Steinhauer, M. A. M. Versteegh, S. Gyger, A. W. Elshaari, B. Kunert, A. Mysyrowicz, and V. Zwiller, "Rydberg excitons in Cu_2O microcrystals grown on a silicon platform," Communications Materials **1**, 11 (2020).

[138] J. Heckötter, B. Panda, K. Brägelmann, and M. Aßmann, "Neutralization of impurities by cw-excitation of high-n rydberg-excitons," (2023), arXiv:2311.03170 [cond-mat.mes-hall] .

[139] G. Han, S. Wen, H. Wang, and Q. Feng, "Surface sulfidization mechanism of cuprite and its response to xanthate adsorption and flotation performance," Minerals Engineering **169**, 106982 (2021).

[140] F. Oba, F. Ernst, Y. Yu, R. Liu, H. M. Kothari, and J. A. Switzer, "Epitaxial growth of cuprous oxide electrodeposited onto semiconductor and metal substrates," Journal of the American Ceramic Society **88**, 253 (2005).

[141] A. S. Rahman, M. Islam, and K. Shorowordi, "Electrodeposition and characterization of copper oxide thin films for solar cell applications," Procedia Engineering **105**, 679 (2015), the 6th BSME International Conference on Thermal Engineering.

[142] M. Izaki, T. Shinagawa, K.-T. Mizuno, Y. Ida, M. Inaba, and A. Tasaka, "Electrochemically constructed p-Cu_2O/n-ZnO heterojunction diode for photovoltaic device," Journal of Physics D Applied Physics **40**, 3326 (2007).

[143] S. Choudhary, J. V. N. Sarma, S. Pande, S. Ababou-Girard, P. Turban, B. Lepine, and S. Gangopadhyay, "Oxidation mechanism of thin Cu films: A gateway towards the formation of single oxide phase," AIP Advances **8**, 055114 (2018).

[144] "Plasma assisted molecular beam epitaxy of cu2o on mgo(001): Influence of copper flux on epitaxial orientation," Journal of Crystal Growth **436**, 87 (2016).

[145] K. B. Chang, L. Frazer, J. J. Schwartz, J. B. Ketterson, and K. R. Poeppelmeier, "Removal of copper vacancies in cuprous oxide single crystals grown by the floating zone method," Crystal Growth & Design **13**, 4914 (2013).

[146] W. Brower and H. Parker, "Growth of single crystal cuprous oxide," Journal of Crystal Growth **8**, 227 (1971).

[147] R. G. Kaufman and R. T. Hawkins, "Annealing of copper and oxygen vacancies in cuprous oxide films monitored by low temperature luminescence," Journal of The Electrochemical Society **133**, 2652 (1986).

[148] S. Koirala, N. Naka, and K. Tanaka, "Correlated lifetimes of free paraexcitons and excitons trapped at oxygen vacancies in cuprous oxide," Journal of Luminescence **134**, 524 (2013).

[149] M. Soltanmohammadi, E. Spurio, A. Gloystein, P. Luches, and N. Nilius, "Photoluminescence spectroscopy of cuprous oxide: Bulk crystal versus crystalline films," physica status solidi (a) **220**, 2200887 (2023).

[150] T. Ha, I. Park, K. I. Sim, H. Lee, J.-S. Bae, S. J. Kim, J. Kim, T.-T. Kim, J.-H. Kim, J. Jang, and S.-Y. Jeong, "Single-crystalline cu 2 o thin films of optical quality as obtained by the oxidation of single-crystal cu thin films at low temperature," APL Materials **7**, 031115 (2019).

[151] R. D. Schmidt-Whitley, M. Martinez-Clemente, and A. Revcolevschi, "Growth and microstructural control of single crystal cuprous oxide Cu_2O," Journal of Crystal Growth **23**, 113 (1974).

[152] J. Pritchard, K. Weatherill, and C. Adams, "Non-linear optics using cold rydberg atoms," Annual Review of Cold Atoms and Molecules **1** (2012).

[153] M. Pritchard, A. Arnold, S. Cornish, D. Hallwood, C. Pleasant, and I. Hughes, "Transport of launched cold atoms with a laser guide and pulsed magnetic fields," **8** (2006).

[154] D. Ziemkiewicz, "Electromagnetically induced transparency in media with rydberg excitons 1: Slow light," Entropy **22** (2020).

[155] D. Ziemkiewicz and S. Zielińska-Raczyńska, "Electromagnetically induced transparency in media with rydberg excitons 2: Cross-kerr modulation," Entropy **22** (2020).

[156] M. Colocci, M. Gurioli, and A. Vinattieri, "Thermal ionization of excitons in GaAs/AlGaAs quantum well structures," Journal of Applied Physics **68**, 2809 (1990).

[157] T. G. Pedersen, S. Latini, K. S. Thygesen, H. Mera, and B. K. Nikolić, "Exciton ionization in multilayer transition-metal dichalcogenides," New Journal of Physics **18**, 073043 (2016).

[158] C. J. Hawthorn, K. P. Weber, and R. E. Scholten, "Littrow configuration tunable external cavity diode laser with fixed direction output beam," Review of Scientific Instruments **72**, 4477 (2001).

[159] C. Petridis, I. D. Lindsay, D. J. M. Stothard, and M. Ebrahimzadeh, "Mode-hop-free tuning over 80 GHz of an extended cavity diode laser without antireflection coating," Review of Scientific Instruments **72**, 3811 (2001).

[160] D. E. Zelmon, D. L. Small, and D. Jundt, "Infrared corrected Sellmeier coefficients for congruently grown lithium niobate and 5 mol.% magnesium oxide–doped lithium niobate," J. Opt. Soc. Am. B **14**, 3319 (1997).

[161] Y. Varshni, "Temperature dependence of the energy gap in semiconductors," Physica **34**, 149 (1967).

[162] P. K. Sarswat and M. L. Free, "A study of energy band gap versus temperature for cu2znsns4 thin films," Physica B: Condensed Matter **407**, 108 (2012).

[163] A. Manoogian and A. Leclerc, "Determination of the dilation and vibrational contributions to the indirect energy band gap of diamond semiconductor," Canadian Journal of Physics **57**, 1766 (2011).

[164] L. Viña, S. Logothetidis, and M. Cardona, "Temperature dependence of the dielectric function of germanium," Phys. Rev. B **30**, 1979 (1984).

[165] J. S. Rojas-Ramírez, R. Goldhahn, P. Moser, J. Huerta-Ruelas, J. Hernández-Rosas, and M. López-López, "Temperature dependence of the photoluminescence emission from InxGa1xAs quantum wells on GaAs(311) substrates," Journal of Applied Physics **104**, 124304 (2008).

[166] D. D. Kang, A. Gross, H. Yang, Y. Morita, K. S. Choi, K. Yoshioka, and N. Y. Kim, "Temperature study of Rydberg exciton optical properties in Cu_2O," Phys. Rev. B **103**, 205203 (2021).

[167] *Handbook of Optical Materials* (2002).

[168] A. K. Mohapatra, T. R. Jackson, and C. S. Adams, "Coherent optical detection of highly excited rydberg states using electromagnetically induced transparency," Phys. Rev. Lett. **98**, 113003 (2007).

[169] E. Inbar and A. Arie, "High-sensitivity measurements of the Kerr constant in gases using a Fabry-Pérot-based ellipsometer," Applied Physics B: Lasers and Optics **70**, 849 (2000).

[170] G. Moore, "Floquet theory as a computational tool," SIAM Journal on Numerical Analysis **42**, 2522 (2005).

[171] P. A. Kuchment, "Floquet theory for partial differential equations," Russian Mathematical Surveys **37**, 1 (1982).

[172] J. D. R. Tommey and S. D. Hogan, "Resonant Rydberg-atom–microwave-field interactions in the ultrastrong-driving regime: Beyond the rotating-wave approximation," Phys. Rev. A **100**, 053417 (2019).

[173] V. Walther, S. O. Krüger, S. Scheel, and T. Pohl, "Interactions between Rydberg excitons in Cu_2O," Phys. Rev. B **98**, 165201 (2018).

[174] F. Schöne, S.-O. Krüger, P. Grünwald, H. Stolz, S. Scheel, M. Aßmann, J. Heckötter, J. Thewes, D. Fröhlich, and M. Bayer, "Deviations of the exciton level spectrum in Cu_2O from the hydrogen series," Phys. Rev. B **93**, 075203 (2016).

Colophon

This thesis is based on a template developed by Matthew Townson and Andrew Reeves. It was typeset with LaTeX 2_ε. It was created using the *memoir* package, maintained by Lars Madsen, with the *madsen* chapter style. The font used is Latin Modern, derived from fonts designed by Donald E. Kunith.